

DELFT UNIVERSITY OF TECHNOLOGY

MASTER TRACK: HYDRAULIC & ENGINEERING

MSC THESIS

Numerical investigation of plastic fragment accumulation against a sluice gate

Author:

Marius Franx (4319753)

Thesis committee:

Chair - Wim Uijtewaal

Daily Supervisor - Davide Wüthrich

External Supervisor - Olivier Hoes

External Supervisor - Jeremy Bricker

External Supervisor - Mohammad Farid

August 19, 2022



PREFACE

This thesis was written to fulfill the graduation requirements of the Hydraulic Engineering master program at the Delft University of Technology. It was carried out as part of an international research group between the Delft University of Technology of the Netherlands and the Bandung Institute of Technology (ITB) of Indonesia. The duration of this graduation project lasted from May 2021 until August 2022.

I would like to thank the entire thesis committee for the supervision and support you provided me during the duration of this final phase of my studies. You gave me the room to set my own direction in this project, but also helped me keeping me on track. Which was frequently quite difficult for me, as there were so many rabbit holes to fall down to the last year. Davide, you always gave me guidance and a clear path ahead when I got stuck in these kinds of situations. All your feedback was to the point, fair and constructive and I thank you for that. Wim, thank you for the patience and knowledge you provided throughout the project and for encouraging me to look more positively on my results and to see its merits. Olivier, thank you for always offering me a different perspective on my work with insightful comments and your infectious enthusiasm. Jeremy, thank you for guiding me through the intertwining and beautiful jungle which is numerical modelling. It was interesting to learn about all the different aspects of this world.

Special thanks to Mohammad, for orchestrating all the experimental research conducted in this thesis. Due to the distance and the 'video-call' nature of this project, it was a challenging task to synchronize all our work and to keep each other perfectly up to date. However, your clear communication and feedback made it work. Furthermore, I would like to express my gratitude to the whole ITB team and especially to Faizal for coordinating the buoyancy experiments and to Ahmad for coordinating the flume experiments.

I would also like to thank Corrado for making time to discuss all the various aspects of SPH with me. You showed me patience in discussing all the subjects ranging from basic fundamentals to highly detailed problems.

Last of all, I want to thank my parents, sister, brother and all my friends for all the love and support you provided to me the last year. Mam, Pap, Tjitske en Jorrit, I love you more than I can express in words. Special shout out to Coco, for getting me through the rough patches with your concrete and benevolent advise. Also my roommate Geert, we were in the same proverbial boat and it was nice to talk over all our issues this year. And lastly thanks to the 'Mean Girls'; being in your company was always the highlight of each day while working on the university.

Marius Franx, August, 2022

SUMMARY

The ramifications of plastic pollution on the environment are becoming increasingly serious in various forms throughout the world. In this context, rivers are the most important suppliers of plastics entering the marine environment. However, rivers that contain high loads of plastic waste also directly harm the livelihoods of people living near these rivers. An example is the flooding of urban areas in Indonesia due to clogging of the hydraulic and drainage systems, which is caused by the blockage of local hydraulic structures by plastic debris.

At this moment, there is a lack of knowledge on this accumulation process and its underlying dynamics, since observational and experimental research is lacking. Numerical modeling has proven to be a great tool for expanding experimental research. However, no suitable numerical method has been identified yet to model the plastic accumulation process, since traditional mesh-based CFD numerical methods are expected to be not a viable option, due to their inability to model the individual interaction between plastic particles, critical during this process. A possible solution could be the SPH-DEM method, which is a two-way coupled numerical approach that simulates fluid and debris as discrete particles and elements.

The objective of this report was to find out if SPH-DEM could be a suitable numerical method to model the dynamic processes of the plastic debris accumulation against hydraulic structures. To accomplish this, the first goal was to realistically model a turbulent open-channel flow and the buoyancy of individual plastic debris, which would be validated by experimental research. The second goal was to investigate which are the most important (numerical) parameters affecting the mentioned plastic debris accumulation.

In this report, experimental research was carried out in the form of buoyancy tests and flume tests, and numerical research was carried out in the form of the design of numerical simulations. In the buoyancy tests, the rising velocities of four plastic fragments that differed in size and density were measured, which were released multiple times in a graduated cylinder filled with water. In the flume tests, first the water elevation was measured along the flume, after which the passing ratio's and carpet lengths were measured for the four different released fragments for three different gate configurations. Two types of numerical models were designed that represented both types of experimental tests, for which several design choices had to be made to compensate for several physical phenomena, which can't be directly represented in the model design.

The numerical buoyancy test was validated with the rising velocities obtained from the experimental equivalent. It was discovered, that for relatively low resolution modeled fragments, the rising velocity u_r is heavily influenced by numerical diffusion. The smoothing length C_h was identified as an important numerical parameter, which can compensate this effect. Furthermore, it was discovered that the degree of numerical diffusion is dependent on the depth of the fragment in the water. The numerical flume test was validated with the water elevation obtained from the experimental equivalent. For uniform flows, by adjusting the boundary viscosity coefficient β , smooth turbulent velocity profiles could be simulated throughout the flume corresponding to theoretical values. However, no single value of β was found in which the velocity profiles of the uniform flow and the validated water elevation of the gradually varied flows were both in agreement with their theoretical values.

After validation, fragments were added to numerical flume model. Per fragment type and gate configuration, four different numerical scenarios were executed, where each scenario was defined by a combination of a certain density ρ_s and restitution coefficient e . Finally, the best corresponding scenarios were used to simulate mixed fragments released in the flow. It was found that the gate opening height d_g , density ρ_s and restitution e of the plastic fragments have the largest influence on the passing ratio's PR , carpet length L_c , carpet shape and carpet stability. Furthermore, it was confirmed that individual fragment interactions play a crucial role in the accumulation process. However, the model is mainly limited by its low resolution and the absence of suitable turbulence models. This means that many forms of fragment behavior seen in the experimental research such of buoyancy, trajectory and individual interactions, which are heavily influenced by turbulence, cannot be sufficiently represented in the numerical model. However, it is shown that by adjusting the density the buoyancy behavior can be partly replicated and by adjusting the restitution coefficient the turbulent individual interactions can be partly replicated.

In conclusion it can be stated that SPH-DEM is an interesting option to model the dynamic processes of the accumulation of plastic debris against a sluice gate; however, further improvements in computational power and turbulence models are needed to be more widely applied.

NOMENCLATURE

α	Viscosity coefficient [-]
β	Viscosity boundary value [-]
δ'	Thickness of viscous sublayer [mm]
δ_ϕ	Free parameter [-]
δ_{ij}	Overlap between fragments i and j [mm]
Γ	Dissipative term [-]
γ	Polytropic constant [m]
γ_n	Normal damping constant [-]
γ_t	Tangential damping constant [-]
κ	Von Kármán constant [-]
μ	Friction coefficient [-]
μ_k	Kinetic friction coefficient [-]
∇	Divergence [-]
ν	Kinematic Viscosity [m^2/s]
ν_p	Poisson coefficient [-]
Π_{ab}	Viscosity term [-]
Ψ_{ab}	Density Diffusion term [-]
ρ	Density of numerical particle or discrete fragment [kg/m^3]
ρ_0	Reference density [kg/m^3]
ρ_e	Effective density [kg/m^3]
ρ_f	Factory density [kg/m^3]
ρ_s	Density of plastic fragment [kg/m^3]
ρ_w	Density of water [kg/m^3]
ρ_{ab}^H	Hydrostatic pressure component [kg/m^3]
ρ_{ab}^T	Total pressure component [kg/m^3]
ρ_{exp}	Density of plastic fragments in experiments [kg/m^3]
ρ_{num}	Density of plastic fragments in numerical simulations [kg/m^3]
τ_w	Shear stress [N/m^2]
A	Cross section of the flume [m^2]
A_g	Cross section of the gate opening [m^2]

B	Width of the flume [m]
B_g	Width of the gate opening [m]
C_c	Contraction coefficient [-]
C_d	Drag coefficient [-]
C_h	Smoothing length coefficient [-]
c_s	Speed of sound at the reference density ρ_0
C_{sound}	Speedsystem coefficient [-]
d	Diameter of plastic fragment [mm]
dp	Initial distance between particles (resolution) [m]
d_1	Water depth upstream the gate [m]
d_2	Water depth downstream the gate and upstream the hydraulic jump [m]
d_3	Water depth downstream the hydraulic jump [m]
d_c	Critical water depth [m]
d_e	Equilibrium water depth [m]
d_g	Height of the gate opening [m]
d_w	Depth of water column [m]
d_{inlet}	Water depth at inlet boundary [m]
d_{outlet}	Water depth at outlet boundary [m]
E	Young modulus [N/m ²]
e	Restitution coefficient [-]
E^*	Reduced Young modulus [N/m ²]
F^d	Damping force [N]
F^r	Repulsion force [N]
F_d	Drag force [N]
F_g	Gravitational force [N]
F_n	Normal force [N]
F_t	Tangential force [N]
Fr	Froude number [-]
g	Gravitational acceleration [m/s ²]
g_x	Horizontal component of the gravitation acceleration [m/s ²]
g_z	Vertical component of the gravitation acceleration [m/s ²]
h	Smoothing length [m]
h_L	Head loss [m]
h_{beam}	Thickness of the bottom beam of the gate [cm]

h_{swl}	Maximum still water level for speed of sound calculations [m]
i_b	Bed-level profile [-]
i_w	Water-surface profile [-]
k	Von Karman's constant [-]
k_n	Normal stiffness [N/m]
k_s	Nikuradse's roughness [mm]
k_t	Tangential stiffness [N/m]
L_c	Floating carpet length [cm]
m	Mass of numerical particle or discrete fragment [kg]
n_B	The total amount of plastic fragments, which can theoretically be distributed over the width of the flume [-]
n_{exp}	The total amount of plastic fragments released in experiments [-]
n_{SPH}	The total amount of plastic fragments released in numerical simulation [-]
P	Pressure [Pa]
PR	Passing ratio [%]
Q	Discharge [m ³ /s]
q	Non-dimensional particle distance [-]
R	Radius of plastic fragment [mm]
r	Distance between particle a and b [mm]
R^*	Reduced fragment radius [mm]
R_*	Shear Reynolds number [-]
R_h	Hydraulic radius [m]
Re	Reynolds number [-]
Re_s	Fragment Reynolds number [-]
S	Channel slope [-]
u	Flow velocity in x direction [m/s]
u^+	Dimensionless flow velocity [-]
u_*	Shear flow velocity [m/s]
u_1	Flow velocity in x direction upstream the gate [m/s]
u_2	Flow velocity in x direction downstream the gate and upstream the hydraulic jump [m/s]
u_r	Rising velocity [m/s]
u_{inlet}	Flow velocity at the inlet boundary [m/s]
u_{outlet}	Flow velocity at the outlet boundary [m/s]
v	Flow velocity in y direction [m/s]
w	Flow velocity in z direction [m/s]

W_{ab}	Weighted (Interpolating) kernel function between particle a and b [-]
x	Stream wise direction [m]
y	Lateral direction [m]
z	Vertical direction [m]
z^+	Dimensionless distance to wall [-]
z_0	Roughness length [mm]

TABLE OF CONTENT

Preface	i
Summary	ii
Nomenclature	iii
1 Introduction	1
1.1 Problem Analysis and Knowledge gap	1
1.2 Research Question	3
1.3 Thesis Structure.	3
2 Literature review	4
2.1 Open Channel Flow	4
2.1.1 Turbulence in general	4
2.1.2 Fluid layers.	5
2.1.3 Flow regimes.	7
2.1.4 Gradually-varied flow	8
2.2 Plastic fragments	10
2.2.1 Plastic fragment properties	10
2.2.2 Rising velocities	11
2.2.3 Plastic fragment accumulation.	12
2.3 Numerical Methods	13
2.3.1 Smoothed-Particle Hydrodynamics (SPH)	13
2.3.2 Discrete Element Method (DEM)	15
3 Numerical Approach	17
3.1 Numerical Model Design	17
3.1.1 Flume design	17
3.1.2 Gate Design	19
3.1.3 Fragment Design.	20
3.1.4 Buoyancy test model.	22
3.1.5 Flume test model	22
3.2 Experimental Research	23
3.2.1 Buoyancy experiments.	23
3.2.2 Flume experiments	23
4 Validation	25
4.1 Buoyancy of individual plastic particles.	25
4.2 Flume experiments	28
4.2.1 No gate model	28
4.2.2 Gate model	32
5 Results	33
5.1 Test set up & Scenario's	33
5.1.1 Red fragments	34
5.1.2 Yellow fragments.	36
5.1.3 Blue fragments.	38
5.1.4 Green fragments	40
5.2 Mixture of fragments	42
6 Discussion	44
6.1 Influence gate opening height	44
6.2 Influence rising velocity and density	44

6.3	Influence restitution coefficient	45
6.4	Limitations	45
7	Conclusion & Recommendations	47
7.1	Conclusion	47
7.2	Recommendations	48
A	Additional Literature	50
A.1	Turbulence models	50
A.2	Technical Requirements numerical method.	51
A.3	Numerical methods assessment	52
A.3.1	Inventory General Numerical Methods	52
A.3.2	Assessment Coupled Numerical Methods	53
B	Experimental research data	54
B.1	Buoyancy Experiments	54
B.2	Flume experiments	54
C	Numerical Design input	58
D	Supplementary numerical results	61
D.1	Red fragments	61
D.2	Yellow fragments	63
D.3	Blue fragments	65
D.4	Green fragments	67
D.5	Anomalies regarding density	69
	Bibliography	71

1

INTRODUCTION

In this chapter, it is shown how the negative impacts of plastic pollution on a macro-scale cause problems on a smaller scale in Indonesia. Based on these problems and the knowledge gap in this specific field of research a problem statement is provided. A possible solution is introduced in the form of the numerical method SPH-DEM and the associated research questions are presented. Finally, the structure of this thesis is provided.

1.1. PROBLEM ANALYSIS AND KNOWLEDGE GAP

The negative impacts of plastic pollution on the environment from a local to a global scale have become one of the most urgent environmental issues in recent times. Especially the effects of plastic pollution on the marine environment seem to be a popular topic at the moment [1]. In this research field, rivers are considered the most important suppliers of plastics that enter the marine environment [2]. However the role of rivers shouldn't be solely considered in a 'marine' context, as the direct harms of plastic pollution on riverine areas can be severe on its own [3]. Several examples of the harms caused by plastic pollution are the ingestion and entanglement of plastic by animals that inhabit these river ecosystems [4], the breakdown of macroplastics in the river into microplastics [5] accompanied by potential risks related to human health [6], and lastly, the damage to the livelihoods of humans living near these rivers. One nation in which these livelihoods are majorly impacted by plastics is Indonesia. This country contains many rivers, which are also one of the most polluted ones in the world [7]. Indonesia is ranked as the 5th most plastic emitting country in the world with an emission of 5.6×10^4 MT of plastic waste per year, accounting for a considerable part of the total global emission of 1.0 (0.8 to 2.7) 10^6 MT yearly [8]. These rivers are mainly polluted due to poor waste management in large urban areas all over the country [9]. For a monsoon country like Indonesia, the magnitude of plastic transport in these rivers is largely influenced by the seasonal variety of its river discharges [10]. A peak transport is observed in February during the wet season, and a lowest transport is observed in August during the dry season [11]. Furthermore, on a short time scale, local flood events during heavy rains significantly increase plastic mobilization from river basins to local rivers, significantly increasing plastic loads in the river [12]. When these polluted rivers enter highly urbanized areas such as Jakarta and Bandung, high loads of macroplastic debris are observed to cause accumulation of plastic waste against local hydraulic structures such as bridges, weirs, and trash racks (Figure 1.1). These accumulations can cause clogging of the entire hydraulic and drainage infrastructure, causing severe additional flood risks [13] and subsequent economic losses.



Figure 1.1: Congested Sungai Cikeruh weir

There is a lack of knowledge on the accumulation process of plastic waste against hydraulic structures, how this process affects the hydraulic performance of these hydraulic structures and the underlying dynamics of the plastic debris involved. Even observational research on this topic is severely lacking, which is problematic, as the lack of fundamental insights on the basic dynamics of the accumulation process makes expanding experimental and/or numerical research difficult. An exception is the observational and experimental research conducted by Honigh *et al.* [14], who researched the accumulation process of plastic waste against racks. In a broader context, Zaat [15] researched the vertical distributions of plastic debris in rivers, revealing more about the behaviour of plastic debris in water and the importance of turbulence in this process. Later, Schouten [16] replicated these vertical distributions in a numerical CFD model, giving a better understanding of the trajectories of plastic debris.

Numerical modeling on fluid dynamics has shown in recent times that it can be a great tool to expand on experimental research. First of all, it can give a better insight on certain fluid dynamics such as flow velocity fields, acting forces and fluid trajectories, which are difficult to obtain from experimental research. Second, it provides precise control over multiple parameters in a user confined environment, which isn't always possible for experimental research due to physical limitations. Lastly, once validated, numerical simulations can be repeated multiple times for slightly different settings or parameters, providing a better understanding of the process, which would be too expensive for experimental research.

Traditionally, the **Computational Fluid Dynamics (CFD)** method is the most applied numerical method in the fluid dynamics research field. However, in the plastic debris accumulation process against hydraulic structures, individual interaction between plastic debris is critical during the accumulation process. For example, individual debris getting entangled in the carpet can lead to an increase of the size of that carpet formation, but individual debris bumping into the carpet can also release debris from the carpet formation. In traditional numerical CFD methods, the fluid and the plastic debris are both modeled as a continuum and debris properties such as size, shape and weight are not directly simulated; these are only indirectly included in the density and volume of the entire debris-fluid. This means that realistically simulating plastic accumulation against various hydraulic structures is difficult, as the debris are not hindered enough by these structures. Another problem with numerical CFD methods is that the modeling of flows with interfaces between two or more different homogeneous fluids is difficult. Computational intensive methods are needed to track or capture the interfaces of multiphase flows, such as the VoF method [17], the marker and cell method [18], and the level set method [19]. This problem becomes even more complicated when complex boundary geometries, such as gates or highly active and deforming free surfaces are present in the model.

From these difficulties the problem statement can be summarized as: ***"Traditional numerical CFD methods are currently limited for providing extra understanding of plastic debris accumulation processes against hydraulic structures"***

A possible solution to this problem could be the **SPH-DEM** method, which is a two-way coupled numerical approach that simulates the fluid and the debris as discrete particles and elements. It was originally introduced to simulate astronomical problems by Gingold and Monaghan [20], but has also recently gained more traction in solving environmental flow problems [21]. Canelas *et al.* [22] introduced a method which unified the discretization of SPH and DEM in the DualSPPhysics software framework. He also validated his method [23], by reproducing an experimental research of Zhang *et al.* [24] concerning dam-breaks. Furthermore, Canelas *et al.* [25] conducted a study in which he simulated a flow of stones flowing through a small slit check dam. This is an interesting set-up as it is quite similar to the set-up proposed in this research.

1.2. RESEARCH QUESTION

The main research question is derived from the problem statement and knowledge gap stated before and is stated as:

How suitable is the numerical method SPH-DEM in modeling the dynamic processes of the plastic debris accumulation against a hydraulic structure?

Before being able to answer the main research question, a number of sub-questions must be answered.

1. How can turbulent open channel flows be sufficiently modeled in SPH?
2. How can the buoyancy of individual plastic debris be sufficiently modeled in SPH-DEM?
3. What are the most important (numerical) parameters affecting the plastic debris accumulation in front of a sluice gate in SPH-DEM?

1.3. THESIS STRUCTURE

In [Chapter 2](#) background information is provided on the physical phenomena mentioned in the first three subquestions, namely turbulent open channel flow, buoyancy of individual plastic debris and accumulation of plastic debris. Subsequently the basic principles of SPH and its difference to traditional numerical methods are described. Finally, it is described how water and plastic debris are fundamentally represented in SPH. After reviewing the literature, sufficient context should have been provided for the design of the numerical models and the interpretation of the results produced.

In [Chapter 3](#) the numerical design is provided and several choices are elaborated on the representation of several physical aspects in this numerical design. Finally, the experimental research is briefly presented.

In [Chapter 4](#) the numerical model is validated with the experimental research provided in the previous chapter. In this chapter, sub question 1 and 2 are answered.

In [Chapter 5](#) The numerical results of adding plastic fragments to the validated flow in the presence of the gate are presented. For several fragment types and gate configurations, different numerical scenarios were executed, for which each results are presented. At last, the best corresponding scenario's are used to simulate mixed fragments released in the flow.

In [Chapter 6](#) the results presented in the previous chapter are discussed. Parameters with the highest degree of influence are presented, answering sub question 3. Lastly, the limitations regarding the representation of fluid and debris dynamics of the numerical model are provided.

In [Chapter 7](#) a conclusion is provided for each sub-question, so that the main research question can be answered subsequently. Finally, a list of recommendations is made for future research.

2

LITERATURE REVIEW

In this chapter, information on the theoretical background is provided, which describes the physical phenomena seen in flume experiments and corresponding numerical methods. First, the typical open-channel flow is discussed, with the emphasis on the turbulent properties of these flows. Subsequently, the behavior of plastic debris is discussed in a flow. Finally, the main principles of SPH are presented and how they represent the physical phenomena described earlier.

2.1. OPEN CHANNEL FLOW

The goal of the experimental flume setup and the numerical flume design is to represent a realistic fluvial flow, typically found in Indonesia. Fluvial flows can be categorized under open channel flows, which are fluid flows within a conduit and containing a free-surface. Generally, the behavior of open channel flows is determined by the effects of viscosity, gravity, and inertia (the surface tension is negligible). The ratio between inertial forces and viscous forces is given by the Reynolds number, which is given in Equation 2.1. Here, the hydraulic radius R_h represents the characteristic length. A core assumption within fluvial flows is that the Reynolds number is sufficiently large (typically $Re > 10^6$) as inertia forces dominate. So, open channel flows are almost always considered turbulent. Therefore, understanding the turbulent behavior of open-channel flows is essential.

$$Re = \frac{uR_h}{\nu} \quad (2.1)$$

2.1.1. TURBULENCE IN GENERAL

Typically, fluid flows can be divided into laminar flows or turbulent flows. Laminar flows are relatively low-velocity flows ($Re < 500$) in which so-called fluid layers flow smoothly over and under each other with little to no mixing of fluid particles. Turbulent flows are relatively high-velocity flows ($Re > 2000$) in which the fluid layers cannot be retained and eddies are constantly generated and dissipated. The presence of these eddies are the cause of the constant mixing of fluid particles in the flow and large fluctuations of velocity and pressure in time and space, as shown by the blue line in Figure 2.1 for velocity:

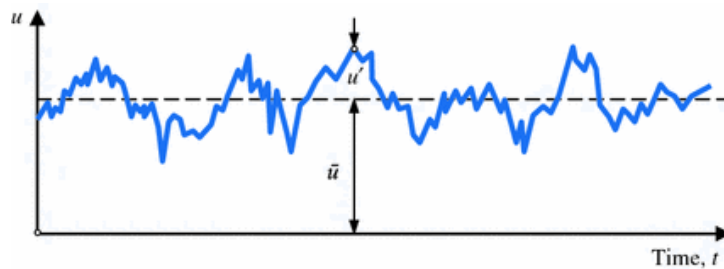


Figure 2.1: Reynolds decomposition for turbulent velocity fluctuations [26]

Mathematically, the values of these fluctuations are determined by subtracting the values averaged over time from the hydrodynamic quantities, such as velocity and pressure. This technique is called the Reynolds decomposition and results in the following equations for velocity and pressure:

$$u = \bar{u} + u' \quad v = \bar{v} + v' \quad w = \bar{w} + w' \quad p = \bar{p} + p' \quad (2.2)$$

The Navier-Stokes momentum equation, which describes the flow of an incompressible fluid, is given in tensor form as:

$$\frac{du_i}{dt} = g_i - \frac{1}{\rho} \frac{\partial p}{\partial x_i} + \nu \nabla^2 u_i \quad (2.3)$$

By applying the Reynolds decomposition to the incompressible Navier-Stokes momentum equation, the Reynolds-averaged Navier-Stokes equation (RANS) is obtained:

$$\frac{\partial \bar{u}_i}{\partial t} = g_i - \underbrace{\frac{1}{\rho} \frac{\partial \bar{p}}{\partial x_i}}_{\text{Pressure gradient}} + \underbrace{\nu \frac{\partial^2 \bar{u}_i}{\partial x_j \partial x_j}}_{\text{Viscous stresses}} - \underbrace{\frac{\partial \overline{u'_i u'_j}}{\partial x_j}}_{\text{Reynolds stresses}} \quad (2.4)$$

The last term is generally called the turbulent stress or Reynolds stress term, which consists of cross products of the velocity fluctuations caused by turbulence. The time averages of these fluctuation values are inherently equal to zero; however, the cross-products of these values do not reduce to zero. To represent the turbulence in a numerical model accordingly in numerical simulations, additional turbulence models are required to close the Reynolds-averaged Navier-Stokes equation (see [Section A.1](#)).

2.1.2. FLUID LAYERS

The flow field of a typical open channel flow can be vertically divided into different fluid layers. Each fluid layer has a different influence on the local average velocity within that layer. The thickness of these layers and the location of the boundaries between them depend on the shear stress τ_w exerted by the wall and its associated shear velocity u_* . In a fully developed turbulent open channel flow in the region near the wall, [Equation 2.4](#) is reduced in the streamwise direction to:

$$0 = \nu \frac{\partial^2 \bar{u}}{\partial z^2} - \frac{\partial}{\partial z} \overline{u'w'} \quad (2.5)$$

By integrating [Equation 2.5](#) in the y direction and applying non-dimensionalization to the equation, the shear velocity u_* can be obtained. From this, the dimensionless distance to the wall z^+ and the dimensionless velocity u^+ can be determined. All parameters are given by:

$$u_* = \sqrt{\frac{\tau_w}{\rho}} \quad z^+ = z \frac{u_*}{\nu} \quad u^+ = \frac{\bar{u}}{u_*} \quad (2.6)$$

The average turbulent velocity profile can be obtained as a function of the dimensionless distance to the wall z^+ for the following 4 fluid layers:

- Viscous sublayer ($z^+ \leq 5$): In this region, viscosity dominates the flow, and turbulence is negligible. Therefore, the total shear stress on the wall τ_w consists only of the constant viscous stress τ_v . By assuming a no-slip condition at the wall, the *linear law* is as follows:

$$u^+ = z^+ \quad (2.7)$$

- Buffer layer ($5 < z^+ < 30$): In this region, viscosity and turbulence exert a similar magnitude of influence on flow. Therefore, the total shear stress on the wall τ_w consists of both the constant viscous stress τ_v and the Reynolds stress. No analytical solution for the local average velocity can be provided for this layer.
- Turbulent wall shear layer ($30 \leq z^+ < 200$): In this region, turbulence dominates the flow and the viscosity is negligible. Therefore, the total wall shear stress τ_w consists only of the Reynolds stress τ_v . By modifying Prantls' mixing length theory, the *law of the wall* is as follows:

$$u^+ = \frac{1}{\kappa} \ln \left(\frac{z}{z_0} \right) + B' \quad (2.8)$$

- Turbulent outer layer ($z^+ \geq 200$): In this region, large eddies are present, which dominate the flow and makes the velocity almost independent of the distance to the wall. By adding a special function to [Equation 2.8](#), the *log-wake law* [27] is as follows:

$$u^+ = \frac{1}{\kappa} \ln \left(\frac{z}{z_0} \right) + \underbrace{\frac{2\Pi}{\kappa} \sin^2 \left(\frac{\pi}{2} z \right)}_{\text{Wake function}} \quad (2.9)$$

Here, Π is known as *Cole's wake parameter*. It seems that for rough boundaries Π has a value of around 0.1 [28] and for smooth boundaries a value of around 0.2 [29].

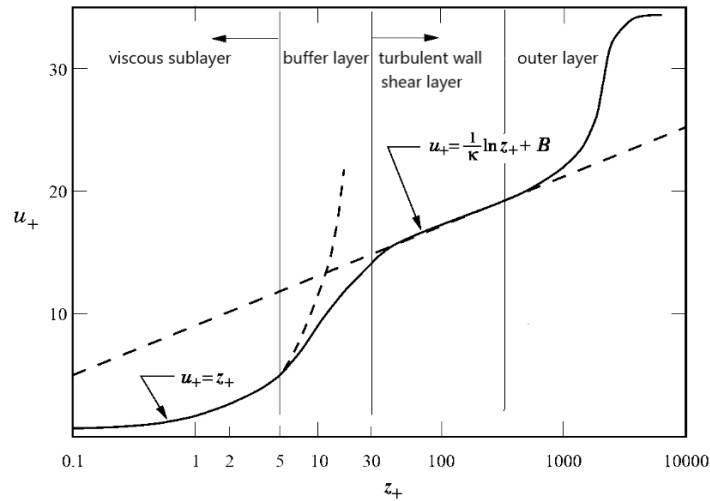


Figure 2.2: Velocity laws of the viscous-, buffer, turbulent wall shear and outer layer [30]

2.1.3. FLOW REGIMES

In addition to the topics mentioned above, the average velocity profile in a turbulent flow also depends on the *roughness* of the wall. Here, the roughness of a wall is physically defined as the irregularities found on the wall surface, represented by the characteristic Nikuradse height k_s . The relationship between the height of the roughness k_s and the thickness of the viscous sublayer previously mentioned δ' determines whether a turbulent *flow regime* can be considered hydraulically smooth, rough, or transitional. This ratio is given by the shear Reynolds number:

$$R_* = \frac{u_* k_s}{\nu} \quad (2.10)$$

Furthermore, the shear Reynolds number also influences the roughness length y_0 , which is the distance from the wall where the velocity following the 'law of the wall' (Equation 2.8) goes to zero and from which the velocity profile is initiated.

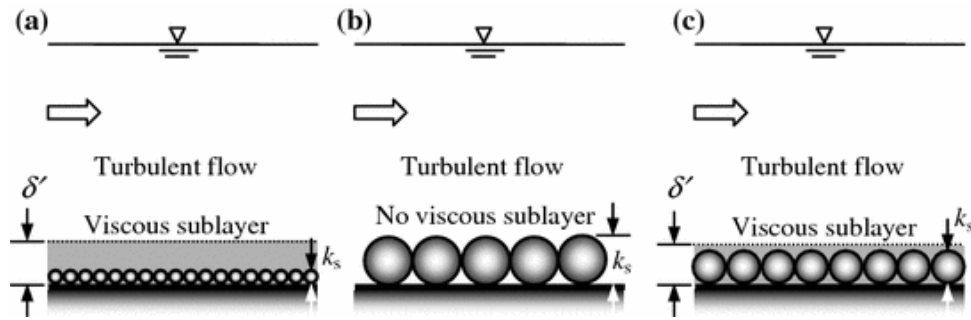


Figure 2.3: Schematic overview of turbulent flow regimes (a):Smooth flow regime, (b): Rough flow regime, (c): Transitional flow regime [26]

- a. *Hydraulically smooth flow* ($R_* \leq 5$): The roughness height k_s is much smaller than thickness of viscous sub layer δ' (Figure 2.3a). Therefore, the roughness elements are totally submerged by the viscous sublayer, and the roughness length z_0 is equal to the thickness of the viscous sublayer δ' . The roughness of the wall is too small to affect the velocity profile, which is therefore only dependent on the viscosity of the fluid. The velocity in the viscous sublayer still follows Equation 2.7, outside the velocity profile is as follows:

$$\frac{\bar{u}}{u_*} = \frac{1}{\kappa} \ln\left(\frac{z}{k_s}\right) + 5.5 + 2.5 \ln(R_*) \quad z_0 = \delta' = 0.11 \frac{\nu}{u_*} \quad (2.11)$$

- b. *Hydraulically rough flow* ($R_* \geq 70$): The roughness height k_s is much higher than the thickness of the viscous sublayer δ' (Figure 2.3b). Turbulence in the form of eddies is generated around the relatively large roughness elements due to flow separation. Therefore, the viscous sublayer and the buffer layer will completely vanish as the viscosity becomes negligible and z_0 is only proportional to the roughness height k_s . The velocity profile that can be seen is as follows:

$$\frac{\bar{u}}{u_*} = \frac{1}{\kappa} \ln\left(\frac{z}{k_s}\right) + 8.5 \quad z_0 = \frac{k_s}{30} \quad (2.12)$$

- c. *Hydraulically transitional flow* ($5 < R_* < 70$): The roughness height k_s is similar in height to the thickness of the viscous sublayer δ' (Figure 2.3c). Therefore, the velocity profile is affected by both the roughness of the wall and the viscosity of the fluid and z_0 is proportional to both the roughness height k_s and the viscous sublayer δ' . The velocity profile is as follows [31]:

$$\frac{\bar{u}}{u_*} = \frac{1}{\kappa} \ln\left(\frac{z}{k_s}\right) + 8.5 + [2.5 \ln(R_*) - 3] e^{-0.121[\ln(R_*)]^{2.42}} \quad z_0 = 0.11 \frac{\nu}{u_*} + \frac{k_s}{30} \quad (2.13)$$

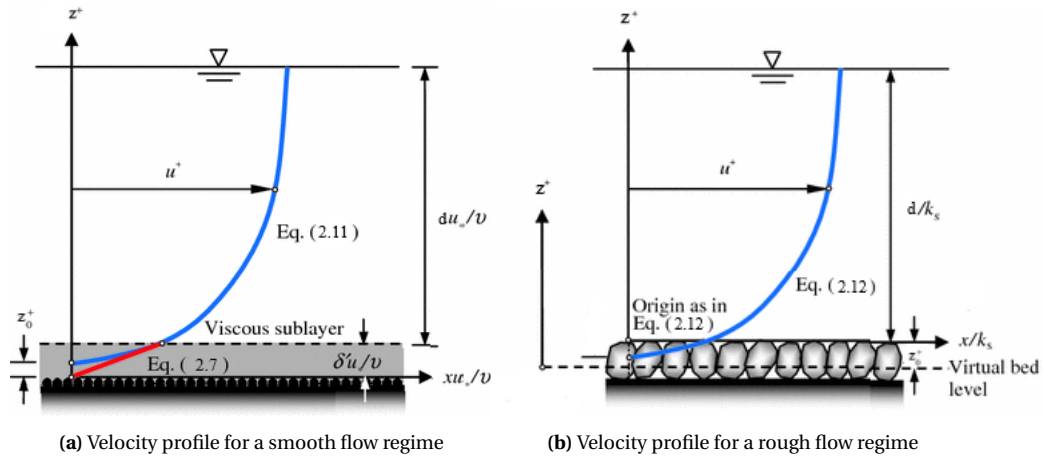


Figure 2.4: Velocity profile for different flow regimes [26]

2.1.4. GRADUALLY-VARIED FLOW

Flow sections can be considered steady uniform, when the water-surface profile (i_w) is equal to the bed-level profile (i_b) and doesn't change in the stream wise direction and therefore the water depth and velocity over the length of this section is in equilibrium. This equilibrium depth d_e depends among other things on the roughness of the bed and can be obtained with the Manning equation:

$$Q = \frac{1}{n} AR_h^{\frac{2}{3}} i_b^{\frac{1}{2}} = \frac{1}{n} (d_e B) \left(\frac{d_e B}{B + 2d_e} \right)^{\frac{2}{3}} i_b^{\frac{1}{2}} \quad (2.14)$$

However due a sudden change in the bottom slope or the presence of an obstruction, an uniform steady flow can transform in a *gradually varied flow* or *rapidly varied flow*, which are characterized by changes in flow depth and velocity. The disruptions causing such changes for the flume setup in this report are the free overflow at the end of the flume, the underflow trough the gate and the hydraulic jump behind the gate.

FREE OVERFLOW

At the downstream end of a typical flume, there is often a sudden drop in bed level, which creates a free overflow situation at this location. At this fixed point, the flow transitions from sub-critical to super-critical and therefore takes on the critical depth d_c ($F_r = 1$). The critical depth only depends on the discharge and the width of the channel, as given by:

$$d_c = \sqrt[3]{\frac{Q^2}{gB^2}} \quad (2.15)$$

This point of critical depth can also be referred to as the *control section*, as it effects the water levels of the sub-critical flow upstream of it. In this case, an M2 backwater curve develops upstream of the control section with a decrease in water depth and an increase in velocity in the flow direction, as can be seen in Figure 2.5.

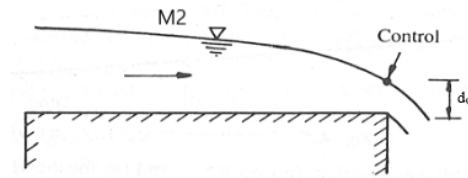


Figure 2.5: Schematic view of free overflow

The development of the water depth upstream the control section along the M2 backwater curve is given by the following Bélanger Equation 2.16. If the flume is long enough, the equilibrium depth is eventually reached, however in practice flumes are often too short.

$$\frac{dd}{dx} = i_w = i_b \frac{d^3 - d_e^3}{d^3 - d_c^3} \quad (2.16)$$

UNDERFLOW

The flow through a sluice gate can be classified as a free surface flow or a submerged flow. The difference is that for a submerged flow, the hydraulic jump downstream the gate will drown and for a free surface flow it does not. In reality, almost all weirs located in the Indonesian riverine system are submerged weirs, as shown, for example in Figure 1.1. However, in this report only free surface flows are considered. A schematic overview of a sluice gate with a free surface flow is shown in Figure 2.6:

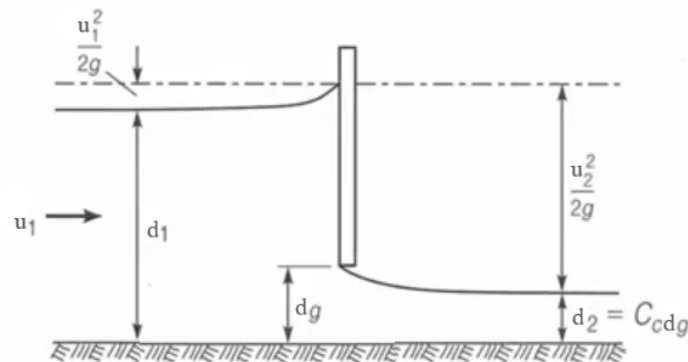


Figure 2.6: Schematic view of underflow trough gate

For a gate opening with a rectangular cross section and the assumption that the energy losses are negligible, the relation between the depth of water upstream the gate d_1 and the depth of water downstream the gate d_2 is given by the energy equation:

$$d_1 + \frac{u_1^2}{2g} = d_2 + \frac{u_2^2}{2g} \quad C_c = \frac{d_2}{d_g} \quad (2.17)$$

Here, d_g is the opening height of the gate and C_c is the contraction coefficient, which normally varies between 0.59 and 0.62 [32].

HYDRAULIC JUMP

The flow downstream of the sluice gate is typically classified as super critical. At a certain point downstream the gate, a hydraulic jump occurs when the supercritical flow suddenly transitions to a subcritical flow. This phenomenon is accompanied by a sudden increase in the depth of the water, a dissipation of energy and resulting head loss h_L as seen in Fig. (2.18)

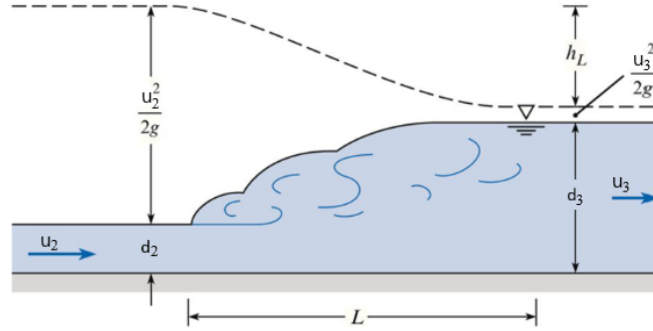


Figure 2.7: Schematic view of hydraulic jump

The relationship between the depth of the water downstream the hydraulic jump d_1 and the depth of the water upstream the water jump d_2 is given by the following Bélanger equation:

$$\frac{d_3}{d_2} = \frac{1}{2} \left(\sqrt{1 + 8Fr_2^2} - 1 \right) \quad Fr_2 = \frac{u_2}{\sqrt{gd_2}} \quad (2.18)$$

2.2. PLASTIC FRAGMENTS

Plastic products are produced with vast amounts of different properties like sizes, shapes, and densities to meet different practical demands from the industry. As these products become litter, these properties can change (e.g. fragmentation) during their long-lasting lifetimes. In fluvial flows these properties have large influence in the trajectory and buoyancy of debris. Therefore, a sufficient understanding of these properties and it's effects on buoyancy is essential.

2.2.1. PLASTIC FRAGMENT PROPERTIES

The size of plastic debris can be divided into three categories according to the European Commission, namely macro debris (>25 mm), meso debris (5-25mm) and micro debris (<5 mm) [33]. Each size category requires a different approach to monitoring and observation methodologies. As far as it is currently known, microplastics don't contribute to plastic debris accumulations found in the field, so in this report only meso and macro plastics are considered.

The shape of plastic debris has a significant influence on the buoyancy of that debris. Plastic debris with complex shapes can contain air pockets which decreases it's overall density and therefor increase it's bouyancy. Furthermore, the drag force exerted on the plastic debris in a buoyancy process depends on the shape. For example, non-spherical debris have a higher drag coefficient than spherical debris. The percentage per shape for which it is in the top 3 of the most frequently found shapes for 43 microplastic studies conducted in Indonesia [34] is presented in Table 2.1. Only fragment shapes are considered in this report, as they are the most found in the field and very straightforward in design.

Shape	Fragment (%)	Fiber (%)	Film (%)	Granule (%)	Foam (%)
Finding percentage	71	63	46	21	21

Table 2.1: Percentage per shape for which it is in the top 3 of the most frequently found shapes for 43 microplastic studies conducted in Indonesia

The density of plastic debris can be divided into two categories, namely, factory density ρ_f and effective density ρ_e [15]. The factory density ρ_f is determined by the type of plastic material and modifications made during production (e.g. foaming and addition of fillers). The effective density ρ_e is determined by aging, biofouling and its ability to trap air during its waste lifetime. The percentage per polymer type for which it is in the top 3 of most frequently found polymers for 46 macroplastic studies conducted in Indonesia [34] is presented in Table 2.2. Only factory densities are considered in the scope of this report.

Polyster type	Finding percentage (%)	Specific gravity ρ_e (g/cm ³)	Examples application
PP	56	0.85-0.83	Bottle caps, drinking straws
PS	33	1.05	Plastic tableware: cups, plates, cutlery
LDPE	33	0.91–0.93	Outdoor furniture
EPS	22	~0.05	Styrofoam
PE	22	0.91–0.96	Plastic bags, plastic bottles
PET	11	1.37	Carbonated drink bottles
HDPE	11	0.94	Detergent bottles, tubes, pipes

Table 2.2: The percentage per polymer type for which it is in the top 3 of most frequently found polymers for 46 macroplastic studies conducted in Indonesia. PP: Polypropylene, PS: Polystyrene, LDPE: Low density polyethylene, EPS: expanded Polystyrene, PE: polyethylene, PET: polyethylene terephthalat, HDPE: High density polyethylene

2.2.2. RISING VELOCITIES

Most plastic fragments have a density lower than water, therefore these fragments will rise in a fluid due to the density difference between the fragment and the water. The associated upward gravitational force F_g is defined as:

$$F_g = (\rho_w - \rho_s)g \frac{4\pi}{3} \left(\frac{d}{2}\right)^3 \quad (2.19)$$

Where ρ_w is the density of water, ρ_s the density of the fragment and d the diameter of the fragment. Rising through the fluid, the fragment will experience drag friction from the water and decelerate. The associated downward drag force F_d is defined as:

$$F_d = \frac{1}{2} C_d \rho_w u_r^2 \pi \left(\frac{d}{2}\right)^2 \quad (2.20)$$

Where u_r is the rising velocity and the frictional drag is represented by the drag coefficient C_d . For perfectly spherical and square micro plastics this drag coefficient is defined by Waldschla and Schu [35] as:

$$C_d = \frac{20}{Re_s} + \frac{10}{\sqrt{Re_s}}; \quad (2.21)$$

The drag coefficient depends on the flow regime around the fragment, which is represented by the fragment Reynolds number Re_s , and is defined as:

$$Re_s = \frac{u_r d}{\nu} \quad (2.22)$$

Where ν is the fluid viscosity. Fragments will accelerate until the gravitational force and drag force are in equilibrium $F_d = F_g$. When this equilibrium is reached, the terminal velocity can be derived from [Equation 2.19](#) and [Equation 2.20](#) as:

$$u_r = \sqrt{\frac{4}{3} \frac{d}{C_d} \left| \frac{\rho_s - \rho_w}{\rho_w} \right| g} \quad (2.23)$$

In the ideal laminar scenario described above, the vertical trajectory of the plastic fragments is only determined by its buoyancy. However, in a turbulent flow as described in [Section 2.1](#) fragments are entrained by eddies, changing their trajectories to random directories. Which causes some fragments to rise faster and other to rise slower. Still, in general, rising velocities as a whole will decrease due to the effects of turbulence.

2.2.3. PLASTIC FRAGMENT ACCUMULATION

Except for the research conducted by Honigh *et al.* [14], there are almost no studies available that describe the specific dynamics of the accumulation of plastic debris against hydraulic structures. In contrast, with wooden debris accumulations more studies have been conducted. Due to the different material properties of wood and plastic these studies shouldn't be seen as perfect substitutions for the lacking knowledge on plastic accumulation. But they give a good insight in the general dynamics of debris accumulation against structures.

Schmoker and Hager [36] showed that the process of accumulation of wood debris in front of a rack can be divided into two phases, namely the first phase of gate formation accompanied by a significant backwater rise and the carpet formation phase accompanied by a minor backwater rise. The same progression through accumulation was also observed for plastic debris in front of a rack by Honigh *et al.* [14]. It's was determined that the rack is blocked faster for plastic debris, which resulted in a faster back-water rise in contrast to wooden debris. Furthermore, the shape of the resulting blockage was determined differently, since organic debris formed a curved blockage ([Figure 2.8](#)) and plastic debris formed an angular shaped blockage ([Figure 2.9](#)).



Figure 2.8: Wooden debris accumulation (curved blockage) [36]



Figure 2.9: Plastic debris accumulation (angular blockage) [14]

2.3. NUMERICAL METHODS

Numerical methods are available in all shapes and forms. Traditionally, the most widely used method is the **Computational Fluid Dynamics (CFD)** method, which is a Eulerian mesh-based numerical method that can model the dynamics of fluid and multi-phase flows. Meshes in all kinds of shapes and sizes can be created by dividing a continuum flow domain into several discrete subdomains. In most solvers, physical information is stored at the nodes of the created grid. At these nodes the discretised Navier-Stoke equations are integrated at every time step based on the neighbouring nodes. As the mesh is fixed these nodes will always interact with the same neighbouring nodes.

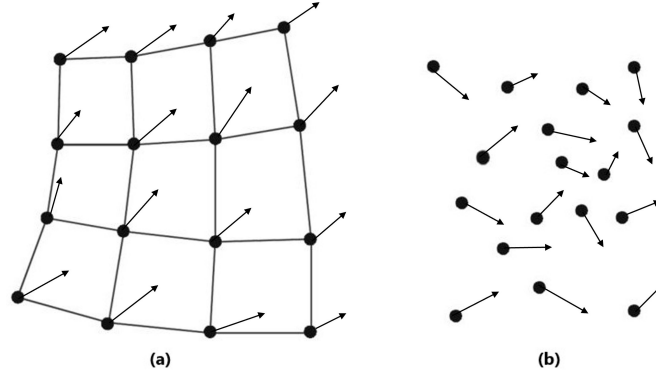


Figure 2.10: (a) Mesh based Eulerian CFD; (b) Meshless Lagrangian SPH

2.3.1. SMOOTHED-PARTICLE HYDRODYNAMICS (SPH)

Smoothed-Particle Hydrodynamics (SPH) is a Lagrangian mesh-less numerical method that can model the dynamics of fluids and particles in a domain. In contrast to traditional CFD methods, in SPH a continuum domain is not modeled by implementation of a fixed grid, but by a set of arbitrary distributed nodal points. Every nodal point has its set of physical properties assigned (e.g., mass, density, velocity, position, pressure). Therefore, these nodal points can be labeled as 'particles', as they carry mass. At the positions of the particles, the discretised Navier-Stokes equations are integrated at every time step based on the influence of neighbouring particles. After integration, the local properties of these particles are updated which determines the movement of these particles. Particles are considered neighboring to a certain particle of interest if they are included in the radius of influence of that particle. The size of the radius is determined by the smoothing length h . The area of influence is circular for 2D situations and spherical for 3D situations. For a 2D situation, the smoothing length h can be expressed as:

$$h = C_h \sqrt{3dp^2} \quad (2.24)$$

Where dp is the initial distance between the particles and C_h the smoothing length coefficient. The typical value for C_h is 1 and sometimes a value 1.2 to 1.5 is used for simulations concerning wave propagation. The magnitude of influence of a random particle b within the influence of radius on a particle of interest a is determined by the weighted kernel function W_{ab} , which is expressed by the Quintic spline function by Wendland [37]:

$$W_{ab}(r, h) = 10/7\pi h^2 \left(1 - \frac{q}{2}\right)^4 (2q + 1) \quad q = \frac{r}{h} \quad (2.25)$$

Where q is the non-dimensional particle distance, which is a function of h the smoothing length and r or x_{ab} is the distance between particles a and b . The smaller the distance between particle a and b , the greater the influence of particle b on a . A visualisation of the radius of influence and the weighted kernel of a particle of interest is displayed in [Figure 2.11](#)

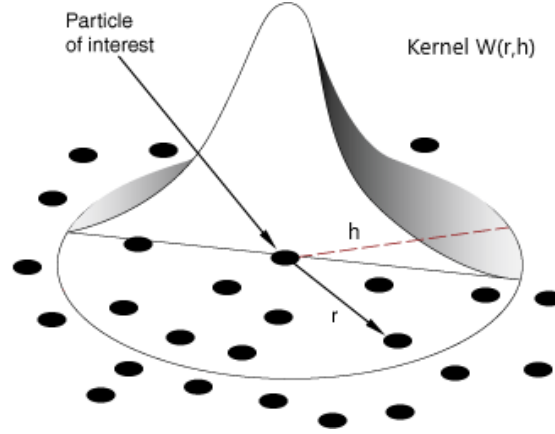


Figure 2.11: Schematic illustration of kernel function [38]

CONTINUITY EQUATION

DualSPHysics is weakly compressible, which in the case of a SPH simulation means that although the mass of each particle remains constant, the associated density can change over time. These changes for a particle of interest a influenced by particle b can be calculated by solving the SPH adjusted continuity equation:

$$\frac{d\rho_a}{dt} = \rho_a \sum_b \frac{m_b}{\rho_b} u_{ab} \nabla_a W_{ab} \quad (2.26)$$

Where m_a and ρ_a are the mass and density of particle a and u_{ab} is the velocity difference between particles a and b . To reduce possible density fluctuations, extra formulation is added to the continuity Equation 2.26, which includes the density diffusion term Ψ_{ab} described by Fourtakas [39]:

$$\frac{d\rho_a}{dt} = \rho_a \sum_b \frac{m_b}{\rho_b} v_{ab} \nabla_a W_{ab} + \underbrace{\delta_\Phi h c_s \sum_b \Psi_{ab} \nabla_a W_{ab} \frac{m_b}{\rho_b}}_{\text{Density diffusion formulation}} \quad (2.27)$$

Where δ_Φ is a free parameter, which is typically set to a value of 0.1 and c_s is the speed of sound at the reference density ρ_0 which can be expressed as:

$$c_s = C_{sound} \sqrt{g \cdot h_{swl}} \quad (2.28)$$

Where C_{sound} is the speedsystem coefficient, which is typically set at a value of 20 and h_{swl} is the maximum still water level for speed of sound calculations. The density diffusion term Ψ_{ab} between particle a and b is given by:

$$\Psi_{ab} = 2(\rho_{ab}^T - \rho_{ab}^H) \frac{x_{ab}}{\|x_{ab}\|^2} \quad (2.29)$$

Where ρ_{ab}^T represents the total component of the pressure and ρ_{ab}^H represents the hydrostatic component of the pressure.

MOMENTUM EQUATION

The momentum Equation 2.3 can be rewritten as the following equation in a continuum:

$$\frac{du}{dt} = -\frac{1}{\rho} \nabla p + g + \Gamma \quad (2.30)$$

Where Γ represents the dissipative terms. These terms are represented in SPH by implementing the artificial viscosity scheme in Equation 2.30, proposed by Monaghan [40]:

$$\frac{du_a}{dt} = -\sum_b m_b \left(\frac{P_b + P_a}{\rho_b \rho_a} + \Pi_{ab} \right) \nabla_a W_{ab} + g \quad (2.31)$$

Where Π_{ab} is the viscosity term, which is given by:

$$\Pi_{ab} = \begin{cases} \frac{-\alpha \overline{c_{ab}} \mu_{ab}}{\rho_{ab}} & v_{ab} \cdot r_{ab} < 0 \\ 0 & v_{ab} \cdot r_{ab} > 0 \end{cases} \quad (2.32)$$

With,

$$\mu_{ab} = \frac{h \cdot u_{ab} \cdot r_{ab}}{r_{ab}^2 + (0.01h)^2} \quad (2.33)$$

Where for α is the viscosity coefficient, which can be tuned to represent the proper dissipation. For interactions between fluid particles, α_{FF} is used for α . For interactions between fluid particles and solid boundary particles α_{FB} is used for α , where $\alpha_{FB} = \beta \cdot \alpha_{FF}$. Where, β is the adjustable viscosity boundary coefficient. Furthermore, the momentum equation requires fluid pressure, which can be obtained with the equation of state, which gives the relationship between pressure P and density ρ as:

$$P = \frac{c_s^2 \rho_0}{\gamma} \left[\left(\frac{\rho}{\rho_0} \right)^\gamma - 1 \right] \quad (2.34)$$

Where γ is the Polytopic constant for water which is 7, ρ_0 is the reference density of the fluid which is 1000 kg/m^3 for water.

2.3.2. DISCRETE ELEMENT METHOD (DEM)

Discrete Element Method (DEM) is a Lagrangian numerical method that can model the dynamics of discrete fragments. Discrete fragments are defined as fragments that do not change size, shape, or weight during the settling process. Originally introduced to simulate behaviour of granular assemblies by Cundall and Strack [41]. Today, bulk materials, rocks, powders, and pharmaceuticals are also commonly simulated in DEM. Non-spherical fragments can also be employed. DEM uses contact detection and contact forces between fragments to determine the movement of these fragments.

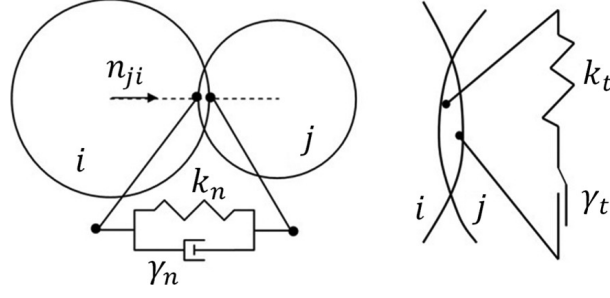


Figure 2.12: Schematic illustration of a normal (left) and tangential interaction (right) between DEM fragments [42]

When two discrete elements interact with each other, as shown in Figure 2.12, the contact force between these two elements can be decomposed into a total normal force F_n and a total tangential force F_t . By assuming the interaction of fragments as a non-linear spring-damper system [43], both forces can be decomposed into a repulsion force F^r and a damping force F^d . Where the repulsion force F^r represents the deformation of the fragments and the damping force F^d the energy dissipation caused by this deformation. The normal force F_n caused by a Hertzian contact of two fragments i and j is given as:

$$\mathbf{F}_{n,ij} = \mathbf{F}_n^r + \mathbf{F}_n^d = k_{n,ij} \delta_{ij}^{3/2} e_{ij}^n - \gamma_{n,ij} \delta_{ij}^{1/2} \dot{\delta}_{ij} e_{ij}^n \quad (2.35)$$

Where the average restitution coefficient e_{ij}^n and the fragment overlap δ_{ij} of interacting fragments i and j are given as:

$$e_n = -\frac{u_n|_{t=t^n}}{u_n|_{t=0}} \quad \delta_{ij} = \max(0, (d_i + d_j)/2 - |r_{ij}|) \quad (2.36)$$

And where the stiffness $k_{n,ij}$ affecting the repulsion force and the damping constant $\gamma_{n,ij}$ affecting the damping force are given as:

$$k_{n,ij} = \frac{4}{3} E^* \sqrt{R^*}; \quad \gamma_{n,ij} = -\frac{\log e_{ij}}{\sqrt{\pi^2 + \log^2 e_{ij}}} \quad (2.37)$$

With the reduced fragment radius R^* and the reduced Young modulus E^* given as:

$$R^* = \left(\frac{1}{R_1} + \frac{1}{R_2} \right)^{-1} \quad E^* = \left(\frac{1 - \nu_1^2}{E_1} + \frac{1 - \nu_2^2}{E_2} \right)^{-1} \quad (2.38)$$

Where ν_p is the Poisson coefficient. The tangential force F_t is represented by:

$$\mathbf{F}_{t,ij} = \min(\mu_{ij} \mathbf{F}_{n,ij} \tanh(8\delta_{ij}^t) e_{ij}^t, \mathbf{F}_t^r + \mathbf{F}_t^d) \quad (2.39)$$

Where:

$$\mathbf{F}_t^r + \mathbf{F}_t^d = k_{t,ij} \delta_{ij}^t e_{ij}^t - \gamma_{t,ij} \delta_{ij}^t \dot{\delta}_{ij} e_{ij}^t \quad (2.40)$$

Where μ_{ij} is the friction coefficient and where the stiffness $k_{n,ij}$ and the damping constant $\gamma_{n,ij}$ are given as:

$$k_{t,ij} = 2/7 k_{n,ij}; \quad \gamma_{t,ij} = 2/7 \gamma_{n,ij} \quad (2.41)$$

3

NUMERICAL APPROACH

In this chapter, the numerical design is provided for the flume, gate and plastic fragments. Furthermore, several design choices are discussed. Finally, the experimental research used for the validation of the model is briefly presented.

3.1. NUMERICAL MODEL DESIGN

All numerical simulations are run by using a GPU of NVIDIA GeForce GTX 1650 on a Aspire A715-74G laptop. It was decided to execute all simulations in a 2D Cartesian coordinate system (x, z) to accommodate acceptable resolutions in combination with acceptable run times, which was impossible in a 3D system. Therefore, additional steps were taken to make sure that the 2D simulations were representative of the 3D phenomena, which will be explained per case in the next sections.

3.1.1. FLUME DESIGN

The numerical design of the flume model includes a facility with a length of 12.35 m (with gate) or 11 m (without gate), which is located on top of a 13 m long rectangular bottom slab consisting of so called dynamic boundary particles [44]. Furthermore, the water body is enclosed by open inlet boundary upstream and open outlet boundary downstream. The open inlet boundary is located on the same location as the first measuring station of the experimental research, whereas the open outlet boundary is located on the same location as the last measuring station of the experimental research. The four different flume set ups which were simulated are presented in Figure 3.1.

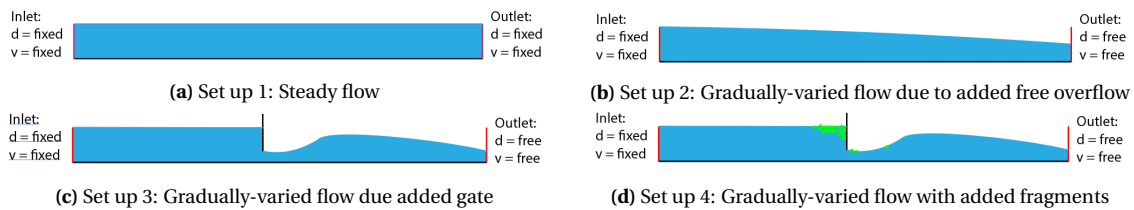


Figure 3.1: Schematic overview of numerical designs for different set ups

As the simulations are executed in 2D, which means that the width of the flume is omitted. Therefore, the numerical model is not influenced by side wall conditions, and it is assumed that the x -axis represents the middle line of the flow. Furthermore due to the lack of width, the specific discharge q was used instead of the total discharge Q :

$$q = Q/B \quad (3.1)$$

Where B is the channel width. The channel slope S is determined with the Manning Equation 2.14 and in-

directly represented in SPH by dissecting the gravitational force g in a horizontal component g_x and vertical component g_z as shown in Equation 3.2:

$$g_x = g \operatorname{arctanh} S \quad g_z = \sqrt{g^2 - g_x^2} \quad (3.2)$$

The initial water elevation imposed over the whole length of the flume is set the equal to the water elevation imposed at inlet boundary. The initial flow velocity imposed uniformly over the length of the flume is set to a similar value as the average velocity imposed at the inlet boundary. For this project, the spin up time was firstly defined as the time required by the model to reach a steady equilibrium of discharge between the inlet and outlet of the flume. Secondly and more importantly, it was defined as the time required by the model to reach a steady state water elevation profile. The simulation time for each scenario was set to 40 seconds to reach water elevation equilibrium.

OPEN BOUNDARY REPRESENTATION

In SPH, open inlet- and outlet boundaries are represented by *Inflow- and Outflow buffers*, as shown in Figure 3.2. These buffers consist of buffer particles, which are created vertically up to the user-defined water level and horizontally in the normal direction up to a user defined permeable boundary. To ensure numerical stability, the number of buffer particles in the horizontal direction is set to 8, so particles interacting with the buffer have full kernel support (Equation 2.25). Buffer particles leaving the buffer are transformed into fluid particles and are simultaneously replaced by newly created buffer particles. Conversely fluid particles entering the buffer are transformed into buffer particles, but no new replacement particles are created [45].

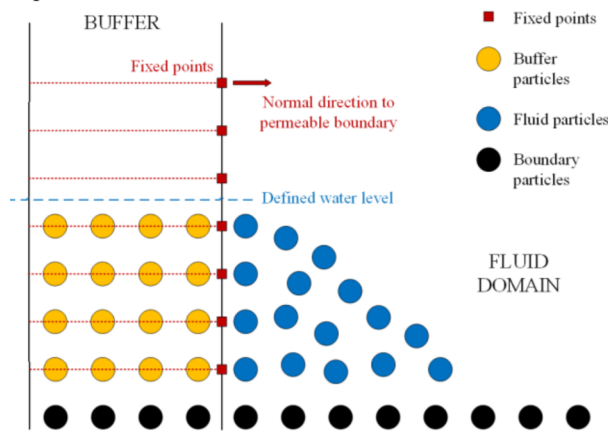


Figure 3.2: Schematic view of inlet buffer [45]

The main physical flow conditions that must be defined in open boundaries are the local water depth d , flow velocity u and lesser degree the density ρ . In SPH, these conditions can be set on a fixed value over time, a variable value over time or be calculated from the fluid domain. Additionally the velocity profile over the water depth at the inlet buffer needs to be defined. The following choices regarding the numerical inflow and outflow buffers were made:

- The water depth d_{inlet} at the inlet buffer is set at a fixed value, as no back flow effects were considered. This value is set to the water elevation measured at the first station of the flume experiment. At the outflow buffer, the water depth d_{outlet} is calculated from the fluid domain. Theoretically the water depth here should approach the critical depth of the flume (Equation 2.15).
- The average velocity u_{inlet} at the inlet buffer is set on a fixed value. As the inflow discharge is constant over time, this average value is simply determined by continuity. To determine the imposed velocity profile, the law of the wall Equation 2.8 can be used. However, some physical parameters required for

input cannot be derived from the experimental research. Therefore parameters Nikuradse roughness k_s and slope S are iterated for several types of flow regime until the average velocity of the associated velocity profile coincide with the fixed average velocity previously determined at the inlet buffer. An example of such iteration for a smooth regime velocity profile can be seen in figure [Figure C.6](#).

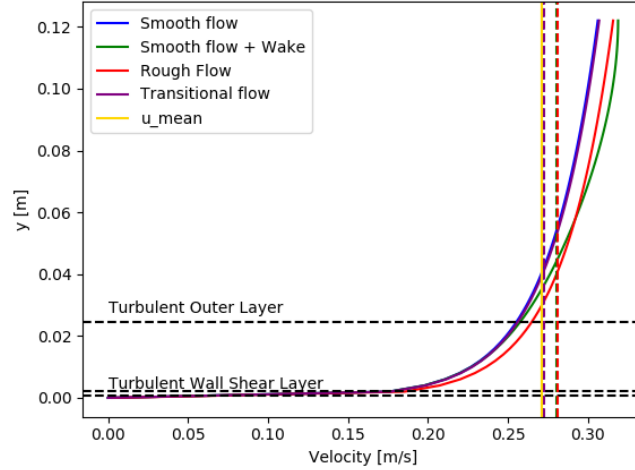


Figure 3.3: Example different velocity profiles

As the steel bottom of the flume has a low roughness (up to 0.0005 m [46]), when iterating the parameters for the rough regime velocity profile, no match in the average velocities could be made. Therefore, the velocity profile for a smooth flow regime is used. The Nikuradse roughness k_s and slope S for which the average velocity of the modified velocity profile is in agreement with the fixed average velocity previously determined from continuity at the inlet buffer are given in [Table 3.1](#) and [Table 3.2](#). At the output buffer, the velocity u_{outlet} is extrapolated from the fluid domain.

	d_{inlet}	u_{inlet}	k_s	S		d_{inlet}	u_{inlet}	k_s	S
High	0.132 m	0.63 m/s	0.00009	0.00109	4.5 cm	0.146 m	0.23 m/s	0.0002	0.00016
Medium	0.088 m	0.42 m/s	0.00015	0.00075	5.0 cm	0.128 m	0.26 m/s	0.0002	0.00023
Low	0.076 m	0.39 m/s	0.00016	0.00072	5.3 cm	0.122 m	0.27 m/s	0.00019	0.00026

Table 3.1: Velocity profile parameters without gate

Table 3.2: Velocity profile parameters with gate

3.1.2. GATE DESIGN

As the numerical simulations are executed in 2D, all the elements of the gate along the y-axis cannot be reproduced; these elements can be seen in the front view of the gate in [Figure 3.4](#). A side view of the gate in SPH is shown in [Figure 3.5](#).

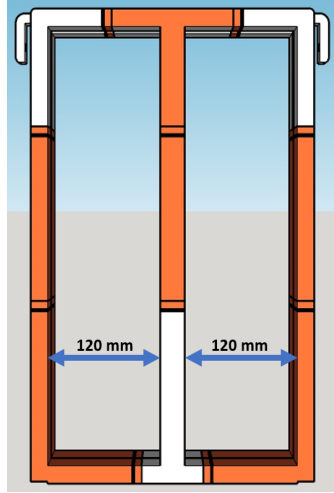


Figure 3.4: Front view gate with dimensions

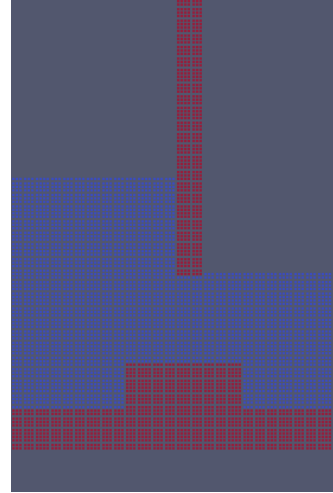


Figure 3.5: Side view of numerical gate

When the flow is passing through the gate, it's restricted by the cross section of the gate as its surface is smaller in comparison to the cross section of the flume, leading to an increase of water elevation in front of the gate. Therefore the cross section of the gate in SPH should also be reduced, in line with the physical model. As the lateral elements are excluded in SPH, alternative design methods were used to get the same cross section, which are:

1. Reducing the hypothetical width ($B_{SPH} = B_g$): The width may not be directly represented in a 2D simulation, but indirectly the specific discharge set at the inflow boundary is indeed a dependent of it, see [Equation 3.1](#). However this method was not chosen, as it affects not only the flow velocity at the gate, but also the velocity over whole flume itself, substantially changing the characteristics of the flow.
2. Reducing the gate opening height ($d_{g,SPH} = \frac{A_g}{B}$): This method is preferred as it's a simple local readjustment of the design. It was chosen to reduce the gate opening height from the bottom d_g , by increasing the thickness of the bottom beam of the gate h_{beam} (originally 1.8 cm), so that the distance between the top of the gate opening and the free-surface of the water upstream remained the same. The relevance of this choice will be further elaborated in [Chapter 6](#). The adjusted gate dimensions per gate configuration are given in [Table 3.3](#).

d_g	A_g	$d_{g,SPH}$	$h_{beam,SPH}$
4.5 cm	0.0108 m ²	3.6 cm	2.7 cm
5.0 cm	0.0120 m ²	4.0 cm	2.8 cm
5.3 cm	0.0127 m ²	4.2 cm	2.9 cm

Table 3.3: Adjusted gate dimensions

3.1.3. FRAGMENT DESIGN

As explained in [Section 2.2](#), the material properties of the plastic fragments like density, shape and size significantly influence the behavior of the fragments their interactions with each other and their environment. In total, 4 types of plastic fragments were investigated, for which these properties were known. The different fragments can be seen in figure [Figure 3.6](#) and its properties are given in [Table 3.4](#):

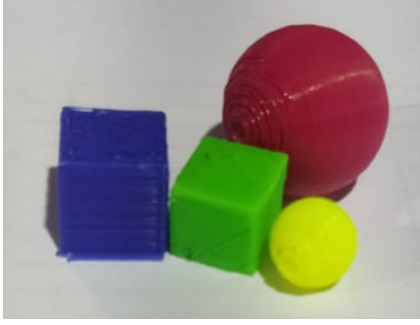


Figure 3.6: Overview of four fragment types with different properties

Color	Shape	Width/Diameter	Density
Red	Sphere	2.0 cm	0.43 g/cm ³
Yellow	Sphere	1.0 cm	0.14 g/cm ³
Blue	Cube	1.2 cm	0.84 g/cm ³
Green	Cube	1.0 cm	0.97 g/cm ³

Table 3.4: Basic properties for each fragment type

The plastic fragments used in the experimental research are made of PLA+ (polylactic acid). PLA+ materials are slightly stronger and stiffer than traditional PLA materials. However, for numerical simulations, the characteristics of traditional PLA materials are used as input, as more is known about them. The material properties of PLA are defined in SPH as follows:

- Young modulus E , which is a mechanical property that measures the tensile or compressive stiffness of a solid material when the normal force is applied. The Young modulus of PLA is approximately 4 GPA [47].
- Poisson ratio ν_p , which is the deformation (expansion or contraction) of a material in directions perpendicular to the specific direction of loading. The Poisson ratio of PLA is approximately 0.33 [47].
- Restitution Coefficient e , which is the ratio of the velocity after collision and the velocity before collision between two fragments. Realistically, this value is at least smaller than 1 due to the typical loss of kinetic energy due, e.g., plastic deformation or heat transfer at collision. Currently, DualSPHysics cannot physically represent the latter phenomena, but the coefficient can be used to calibrate the dissipation of each collide. At first collisions are assumed to be fully elastic ($e=1$) as speed of fragments is fairly low.
- Kinetic friction coefficient μ_k , which occurs when two objects are moving relative to each other and rub together. The kinetic friction of PLA is roughly 0.5 [48]

Other design components for which material properties need to be defined are the glass cylinder used in buoyancy experiments and the steel bottom and the pvc gate for flume experiments. The information about these materials is specified by DualSPHysics itself. A summary of all the material properties is provided in the following table [Table 3.5](#).

Material	Young modulus E	Poisson ratio ν_p	Restitution Coefficient e	Kinetic Friction Coefficient μ_k
PLA	4 GPA	0.33	0.5	0.5
PVC	3 GPA	0.30	0.6	0.45
Glass	65 GPA	0.23	0.85	0.40
Steel	210 GPA	0.3	0.80	0.45

Table 3.5: Summary of material properties used in the present study

FRAGMENT SIZE/SHAPE REPRESENTATION

The shape and size of the plastic fragments in the numerical model are highly influenced by the resolution imposed on that model, as can be seen in [Figure 3.7](#). In SPH, the resolution is defined by the distance between

particles dp (Equation 2.24), which among others determines how many particles are included in the plastic fragments. If the resolution is too low, spherical fragments may lose their spherical shape entirely due to the lack of particles, as shown in Figure 3.7c. For this, the dp is set to 0.002 m for all numerical simulations. A higher resolution is naturally preferred, but that would lead to long run times.

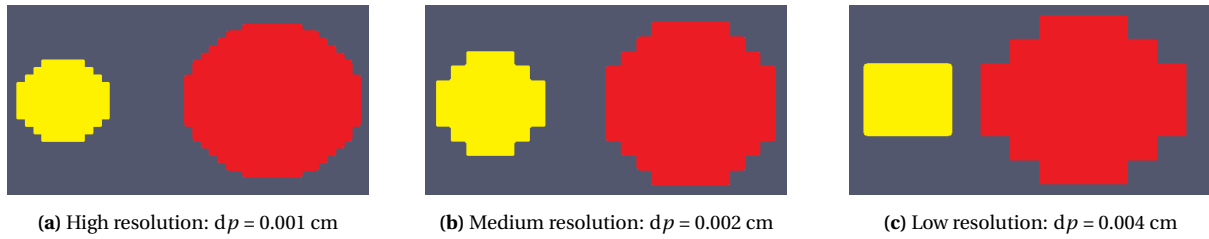


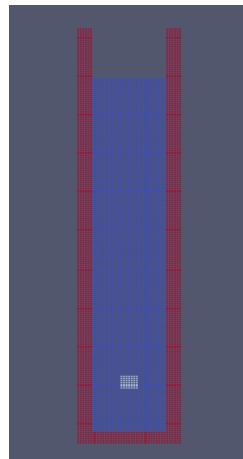
Figure 3.7: Shape and size of yellow and red plastic fragments with different resolution

3.1.4. BUOYANCY TEST MODEL

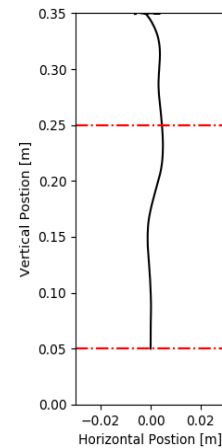
The numerical design of the buoyancy model included a water column with a diameter of 6 cm and a depth of 35 cm enclosed by an U-shaped fixed solid boundary representing experimental tests conducted in a glass cylinder, as shown in Figure 3.8b. Different individual plastic fragments are placed in the middle of the cylinder 5 cm from the bottom up. After starting the simulation, the time it took the particles to move up 20 centimeters is measured, as shown in Figure 3.8c. From this, the numerical rising velocity u_r could be easily calculated. The simulation time for each case was set to 10 seconds to give the fragments enough time to rise.



(a) Buoyancy experiment performed by ITB



(b) Red: Glass cylinder;
Blue: Water column;
White: Plastic fragment



(c) Red: Water column;
Blue: Glass cylinder;
White: plastic fragment

3.1.5. FLUME TEST MODEL

As the numerical simulations are performed in 2D, the amount of fragments released in the model should be modified. The total amount of plastic fragments n_{SPH} released per numerical simulation is determined by dividing the total amount of plastic fragments n_{exp} released during the experiments by the amount of plastic fragments n_B , which can theoretically be distributed over the width of the flume. This theoretical amount is determined by dividing the width B of the flume by the the width/diameter d of the type of fragment released. Equation 3.3 implied that 27 fragments were released if red fragments were used, 13 fragments if yellow or green fragments were used, and 16 fragments if blue fragments were used.

$$n_{SPH} = \frac{n_{exp}}{n_B} = \frac{n_{exp}}{(B/d)} \quad (3.3)$$

The fragments were released in a horizontal sequence, as close to the inlet boundary as possible without influencing it and just above the water surface, as shown in [Figure 3.9](#). The distance between each fragment is set to 3 cm. Fragments were released after the flow of the model had enough time to accelerate, the water elevation downstream was generally stable after 20 seconds. To give the fragments enough time to move past the gate, the total simulation time for each case was set to 40 seconds.



Figure 3.9: Representation release fragments at $t = 20$ s

3.2. EXPERIMENTAL RESEARCH

To validate the numerical model, three series of physical experiments were conducted by the water resources engineering research group of Bandung Institute of Technology (ITB), Indonesia. First, simple buoyancy experiments were conducted to determine the rising velocities of the plastic fragments. Second, flume experiments were conducted where the water elevation along the flume were determined. Lastly, flume experiments were conducted in which plastic fragments were released, where the ratio of these fragments passing the installed gate was determined.

3.2.1. BUOYANCY EXPERIMENTS

The experiment consisted of the release of a single plastic fragment in a graduated cylinder with an inner diameter of 6 cm and filled up with 1 Liter of water, as shown in [Figure 3.8a](#). For the experiment, the time in which the fragments moved up 20 centimeters was measured, from which the rising velocity was calculated. This procedure was performed five times per fragment type; as detailed in [Section B.1](#). The final rising velocity is determined by averaging the rising velocities found per fragment type, summarized in [Table 3.6](#).

Color	Red	Yellow	Blue	Green
Rising velocity u_r	0.205 m/s	0.147 m/s	0.098 m/s	0.044 m/s

Table 3.6: Final rising velocities for each fragment type obtained from experimental research

Interestingly, the rising velocities found by these physical tests are significantly lower than the rising velocities found by Waldschla and Schu [35], following [Equation 2.23](#). This can be explained by the difference in test set up; Since the fragments in the physical tests were released from standstill ($u_r = 0$) and measured over a relatively small distance (20 cm), while the fragments of Waldschla and Schu [35] were already up to speed and measured over a relatively long distance (1 m). This implies that the latter fragments had more time to accelerate and therefore have a higher mean velocity.

3.2.2. FLUME EXPERIMENTS

All flume experiments were carried out in a 12.5 m long, 0.3 m wide and 0.45 m deep flume as shown in [Figure 3.10](#). Throughout the flume, the local elevation of the water was measured at 14 locations along the channel. The locations of these measurement stations can be found in [Table 3.7](#). Stations 1 through 14 are used for the flume experiments without gate, whereas stations 2 through 12 are used for the flume experiments with gate. The discharge is measured by an electromagnetic flow meter in the supply pipes; a complete schematic overview of the flume can be seen in [Figure 3.11](#).

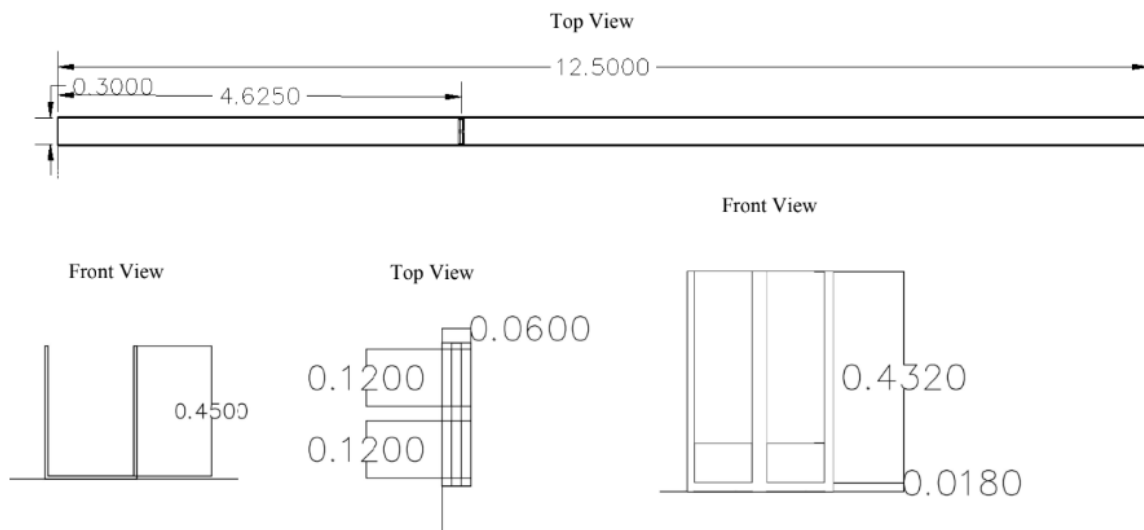


Figure 3.10: Dimensions flume set-up

The experiments without the presence of a gate were conducted with discharges of 11.236 L/s, 8.91 L/s and 24.97 L/s, for each discharge the experiment was executed once. All experiments with the presence of the gate and fragments were conducted with a discharge of 10.0 L/s. The gate was located at $x = 46.25$ m and 3 different gate configurations were executed, with gate openings heights set to 45 mm, 50 mm and 53 mm. For each gate configurations, the experiment was first executed without the plastic fragments to get the initial water elevations. Subsequently, 400 fragments of each fragment type were released in the flume and this was executed 3 to 5 times for each fragment type. The concluding water elevations and pass ratios were determined by averaging the found values in these experiments. All results can be found in [Section B.2](#).

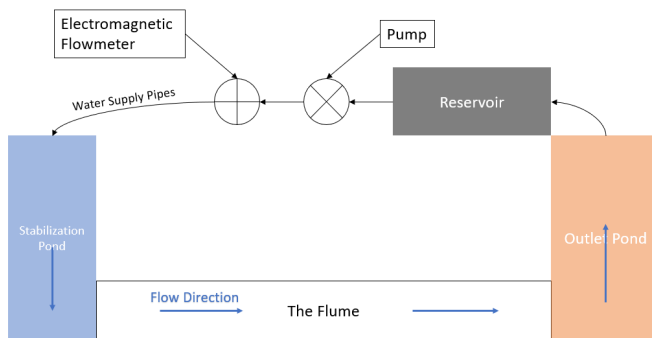


Figure 3.11: Flume top view

Station	Location	Station	Location
1	0.15 m	8	7 m
2	1 m	9	8 m
3	2 m	10	9 m
4	3 m	11	10 m
5	4 m	12	11 m
6	5 m	13	12 m
7	6 m	14	12.5 m

Table 3.7: Locations measurement stations

4

VALIDATION

In this chapter, the validity of the model described in Section 3.1 is presented and its suitability to reproduce real life scenario's is discussed. Once validation is completed for the flow and plastic fragments, plastic fragments are added to the flume simulations and are examined in Chapter 5.

4.1. BUOYANCY OF INDIVIDUAL PLASTIC PARTICLES

The goal of the buoyancy models is to find the numerical conditions and fragment density that gives the best agreement between the rising velocities in the model and in the experimental tests. Once defined, these numerical conditions and densities are included in following numerical design. The first simulations were executed with the numerical density equal to the experimental densities of the plastic fragment. The development of the vertical velocities over time after release for each fragment type are given in Figure 4.1, Figure 4.2, Figure 4.3 and Figure 4.4. Furthermore the theoretical (Subsection 2.2.2), experimental (Subsection 3.2.1) and numerical (Subsection 3.1.4) rising velocity u_r are plotted over the horizontal axis.

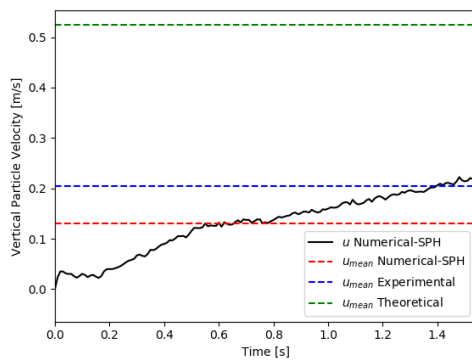


Figure 4.1: Rising velocity Red $C_h = 1 u = 0.205 m/s$

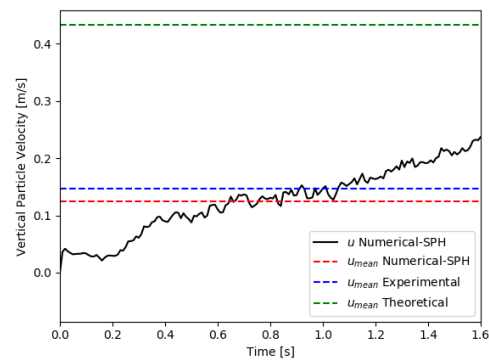


Figure 4.2: Rising velocity Yellow $C_h = 1 u = 0.147 m/s$

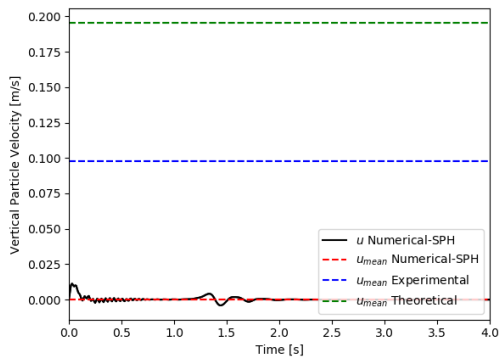


Figure 4.3: Rising velocity Blue $C_h = 1$ $u = 0.098\text{ m/s}$

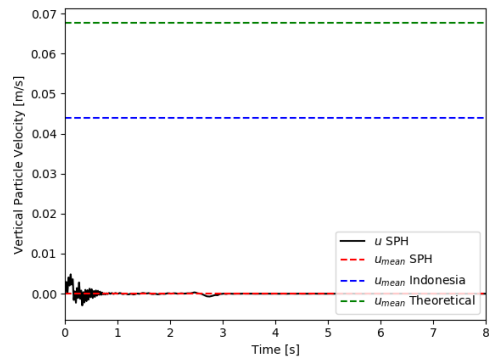


Figure 4.4: Rising velocity Green $C_h = 1$ $u = 0.044\text{ m/s}$

It can be seen that for none of the fragments, the numerical and experimental rising velocity matched, in addition the higher density fragments (blue and green) staid motionless after release. Therefore the numerical density is modified until the numerical rising velocity is equal to the experimental rising velocity, which is shown in Figure 4.5, Figure 4.6, Figure 4.7 and Figure 4.8.. For the lower density fragments (red and yellow), the densities needed little adjustments; however, for the higher density fragments (blue and green), the numerical conditions also needed to be adjusted to prevent unrealistic large adjustments to the density.

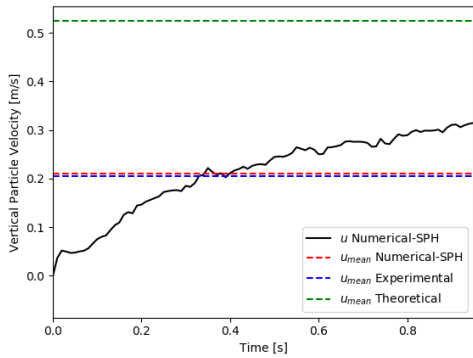


Figure 4.5: Rising velocity Red $C_h = 1$ $u = 0.205\text{ m/s}$

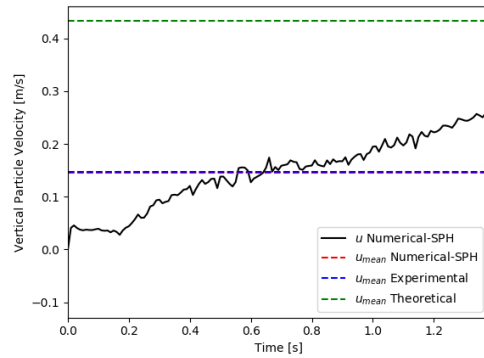


Figure 4.6: Rising velocity Yellow $C_h = 1$ $u = 0.147\text{ m/s}$

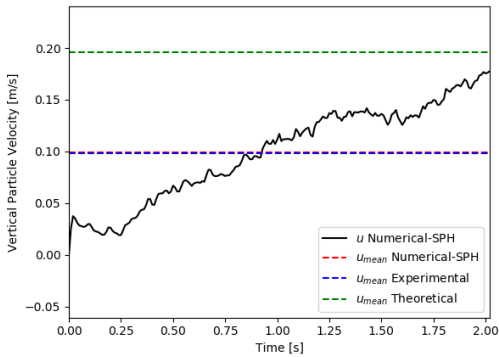


Figure 4.7: Rising velocity Blue $C_h = 1$ $u = 0.098\text{ m/s}$

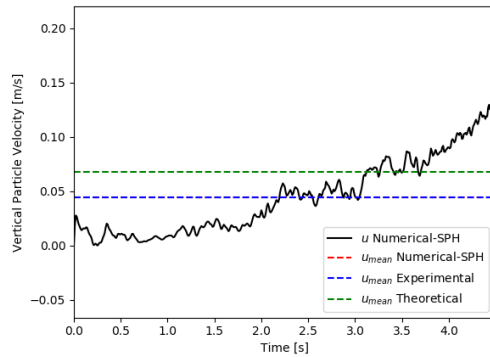


Figure 4.8: Rising velocity Green $C_h = 1$ $u = 0.044\text{ m/s}$

With regard to rising velocity, the smoothing coefficient C_h is the most influential numerical parameter applicable for adjustment. As motioned in [Subsection 2.3.1](#), the smoothing coefficient determines together with the resolution the smoothing length of each particle ([Equation 2.24](#)). Typically this coefficient has a value of 1.0. The numerical densities for which the numerical and experimental rising velocities coincide are given for different values of the smoothing coefficient in [Table 4.1](#):

	Experimental	$C_h = 1.0$	$C_h = 1.25$	$C_h = 1.5$
Red	430 kg/m ³	190 kg/m ³	450 kg/m ³	530 kg/m ³
Yellow	140 kg/m ³	60 kg/m ³	460 kg/m ³	600 kg/m ³
Blue	840 kg/m ³	400 kg/m ³	670 kg/m ³	780 g/m ³
Green	970 kg/m ³	500 kg/m ³	710 kg/m ³	880 kg/m ³

Table 4.1: Numerical densities for different values of smoothing coefficient C_h

It can be seen that for higher values of the smoothing coefficient the particles become more buoyant, since higher densities need to be assigned to the particles to match the rising velocities. The relevance of the smoothing coefficient C_h can be best explained in the context of numerical diffusion between plastic fragments and water. This happens as the particles located on the exterior of the plastic fragments are numerically diffused with the neighbouring water particles. As the fragments in the model are relatively small ($D=1-2$ cm) compared to the imposed resolution ($dp=2$ mm), they consist of a relatively small amount of particles. Therefore, the particles located on the exterior of the fragments are numerically diffused, make up a relatively large number of the total amount of particles. These are also the particles that interact the most with water particles. As the density difference between these exterior plastic particles and water particles is now smaller, the fragment as a whole will be less buoyant. By artificially increasing the smoothing length by increasing the smoothing coefficient, water particles are also forced to interact with the unchanged inner particles of the plastic fragment, thereby increasing density difference and also buoyancy of the plastic fragment in contrast of the water.

Another solution was to increase the resolution of the model, so that among the total amount of particles in a fragment, fewer particles were numerically diffused. This is similar to Canelas *et al.* [49], where released fragments consisted of more particles due to a higher ratio between fragment size and resolution ($D=2$ m; $dp=5$ cm), providing satisfactory results. This is also confirmed by examining the rising velocity per fragment type for different resolutions, which is given by [Table 4.2](#). However as mentioned earlier, an increase in resolution would lead to longer computation times, which was not feasible.

	$dp = 0.002$ m	$dp = 0.001$ m	$dp = 0.0005$ m
Red	0.205 m/s	0.247 m/s	0.290 m/s
Yellow	0.147 m/s	0.171 m/s	0.211 m/s
Blue	0.098 m/s	0.144 m/s	0.185 m/s
Green	0.044 m/s	0.087 m/s	0.120 m/s

Table 4.2: Rising velocities for different numerical resolutions dp

The rising velocity u_r for different depths of the water column d_w in which the fragment is released per fragment type is given by [Table 4.3](#) for a short smoothing length ($C_h = 1.0$) and [Table 4.4](#) for a long smoothing length ($C_h = 1.5$). Depths for which no particle movement was observed are marked with 'X'. No changes in

the way of measuring or the location of release where made. It can be seen, that as the depth of the water column increases, the rising velocity of the particles also decreases. This is worth of notice, as this seemingly "depth dependency" is not mentioned in [Subsection 2.2.2](#) as one of the factors that affect the rising process of plastic fragments. This is logical; since in incompressible hydrostatic water, the difference in water pressure above and below the particle is always the same and relatively minimal compared to the density difference between the particle and the water. This means that the problem appears to be numerical, since the simulations carried out with short smoothing lengths are more affected by this "depth dependency" than simulations carried out with long smoothing lengths. This can be explained by the fact that the numerical water body is not incompressible and therefore the density is higher at the bottom of the water column compared to the top. The deeper the water column, the larger this density difference between the top and bottom will be. This also means that the numerical diffusion between the plastic fragment and the water will be larger if this fragment is located lower in the water column, which results in less buoyancy as showed earlier. What this means for the validity of the buoyancy test will be discussed in [Chapter 6](#).

	$d_w = 0.35$ m	$d_w = 0.70$ m	$d_w = 1.0$ m
Red	0.205 m/s	0.066 m/s	X
Yellow	0.147 m/s	X	X
Blue	0.098 m/s	X	X
Green	0.044 m/s	X	X

Table 4.3: Rising velocities for different water column depths d_w per fragment type for smoothing coefficient $C_h = 1.0$

	$d_w = 0.35$ m	$d_w = 0.70$ m	$d_w = 1.0$ m
Red	0.205 m/s	0.163 m/s	0.136 m/s
Yellow	0.147 m/s	0.092 m/s	0.058 m/s
Blue	0.098 m/s	0.051 m/s	0.025 m/s
Green	0.044 m/s	X	X

Table 4.4: Rising velocities for different water column depths d_w per fragment type for smoothing coefficient $C_h = 1.5$

4.2. FLUME EXPERIMENTS

The flume simulations are validated by finding the numerical conditions that best match the water elevation in the experimental research. Furthermore, it's investigated to what extent the numerical flow can be considered turbulent, by examining different velocity profiles.

4.2.1. NO GATE MODEL

First, the numerical set-up 2 ([Figure 3.1b](#)) for a gradually-varied flow due to free overflow at the end of the flume is modeled. The development of the water elevation over the length of the flume produced by the numerical model is plotted in [Figure 4.9](#) at various points of time time steps using different colors. The water elevation measured in the experiments are plotted as dots. In general, the numerical water profile is similar to the one measured in the experiments. However upstream at the inlet the numerical results show an unregular behaviour, since the flow needs to adjust to the models boundary conditions. Furthermore, it can be seen that the numerical and measured water profiles start to deviate as the outlet approaches ($x = 8$), since the numerical profile seems to deflect more toward the theoretical critical depth ([Equation 2.15](#)). From this point on, the theoretical Belanger equation [2.16](#) can be plotted upstream, as seen in [Figure 4.10](#). The numerical and theoretical water profiles can be matched by iterating k_s . This iterated value of k_s was found to be $4.0 \cdot 10^{-6}$ m, instead of the imposed value at the inlet of $9.0 \cdot 10^{-5}$ m.

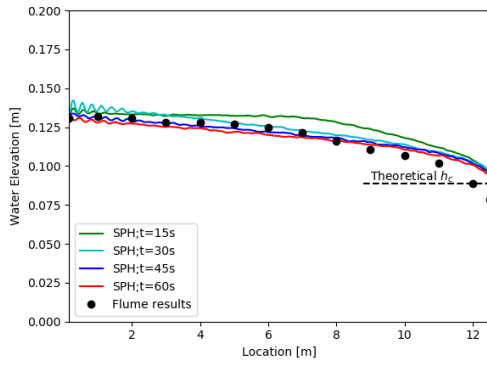


Figure 4.9: Numerical and experimental water elevation over time of a gradually-varied flow $\beta = 0.8$

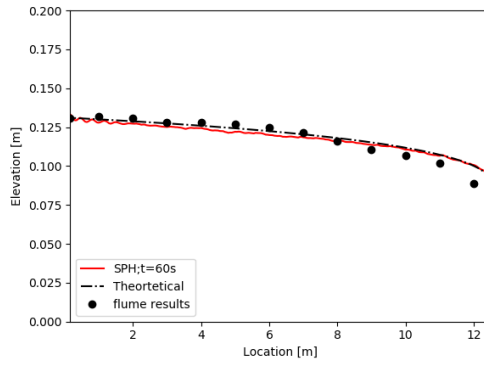


Figure 4.10: Numerical and theoretical water elevation over time of a gradually-varied flow $\beta = 0.8$

A sensitivity analysis showed that with regard to water elevation, the viscosity boundary coefficient β is the most influential numerical parameter. The influence of β can be explained as it represents the friction at the bottom of the flume, as in SPH β determines the degree of friction between the water and solid particles, which strongly influences the acceleration of the flow near the solid boundary. For [Figure 4.9](#) and [Figure 4.10](#), a β value of 0.80 was found give be the best agreement between the numerical, measured and theoretical water profiles.

Based on previous results, it could be argued that there is a strong correlation between β and the physical roughness of the bottom flume k_s . However, the Nikuradse roughness is also an important parameter in the context of velocity profiles. The development of the velocity profile over time at location $x=6$ halfway the flume is given in [Figure 4.11](#).

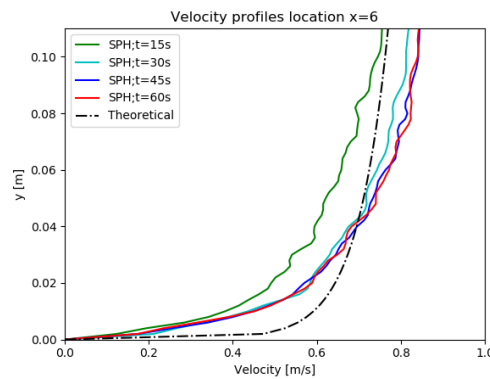


Figure 4.11: Velocity profile at location $x = 6m$ for free overflow outlet $\beta = 0.8$

To compare these profiles with the theoretical ones, uniform flow depth must be imposed over the length of the flume ([Figure 3.1a](#)). This is achieved by fixing the value of water elevation at the outlet to be equal to the water elevation at the inlet; this means that there is no decrease of water elevation accelerating the flow and influencing the velocity profile, and an example can be seen in [Figure 3.1a](#). The development of the water elevation over the length of the flume in time for high flow velocity with a fixed outlet conditions is given in [Figure 4.12](#) and it's associated velocity profile in [Figure 4.13](#).

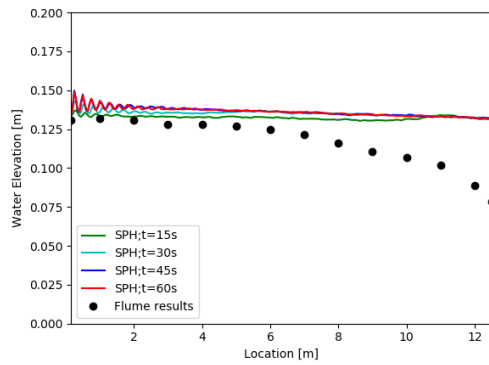


Figure 4.12: Water elevation over time for uniform flow with fixed outlet $\beta = 0.8$

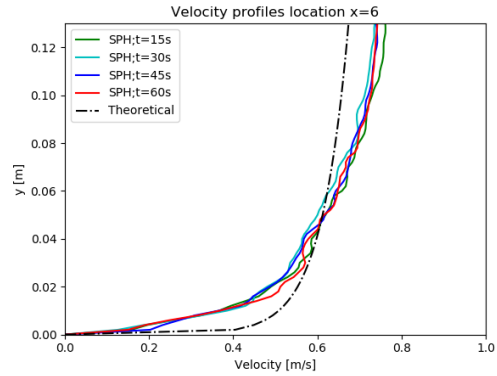


Figure 4.13: Velocity profile at location $x = 6m$ for uniform flow with fixed outlet $\beta = 0.8$

It can be seen in [Figure 4.13](#), that the upper section of the numerical velocity profile coincides better with the theoretical velocity profile in comparison to the unfixed outlet scenario. However, towards the bottom, the numerical flow velocity profile still strongly deviates from the theoretical velocity profile. It seems that there is too much numerical friction from the bottom of the flume. By decreasing β to 0.4 for a uniform water depth over the length of the flume, a more accurate velocity profile can be created following the theoretical velocity profile, which can be seen in [Figure 4.15](#).

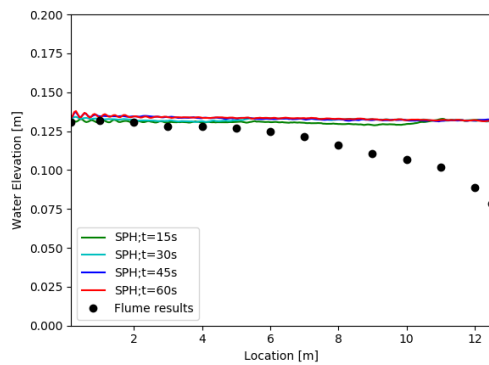


Figure 4.14: Uniform water elevation $\beta = 0.4$

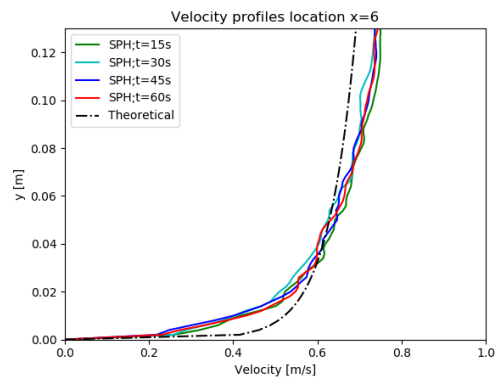


Figure 4.15: Corrected velocity profile $\beta = 0.4$

However, by decreasing β , the elevation of the water also decreases as the acceleration of the flow increases. When implementing a β value of 0.4 again for gradually varied flow with a free overflow outlet instead of a fixed outlet. It can be seen in [Figure 4.16](#), that the water elevation aren't in agreement with the measured values anymore.

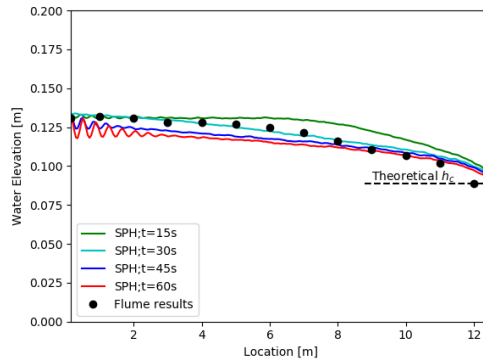


Figure 4.16: Incorrect water elevations for free overflow outlet
 $\beta = 0.4$

By decreasing β even further to 0.1, an accurate turbulent velocity profile can be created, which is shown in Figure 4.18. However, in Figure 4.17 it is shown that the flow accelerates so much, due to the lack of resistance from the bottom, that the water elevation drops at the inlet. Therefore the water elevation has to slope up towards the outlet to meet the boundary condition at the outlet. So using a β of 0.1 for gradually varied flow will also not lead to accurate water elevation levels.

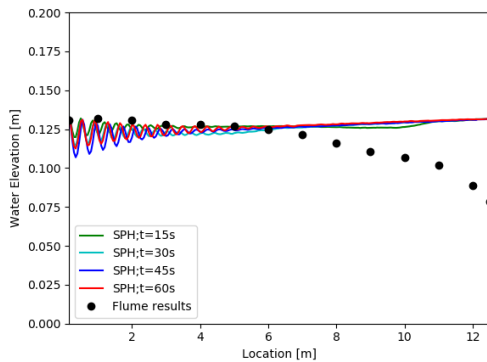


Figure 4.17: Water elevation
 $\beta = 0.1$

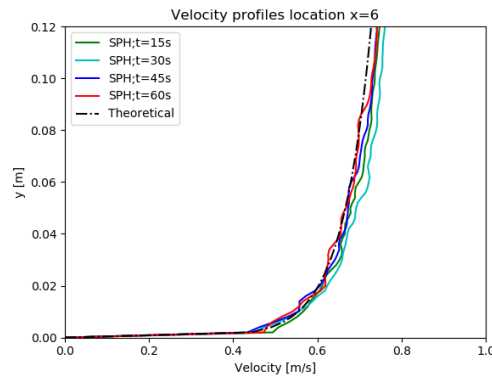


Figure 4.18: Accurate velocity profile
 $\beta = 0.1$

In conclusion, it seems impossible to obtain the correct representation of the water elevation and velocity profile by only adjusting β . Since the goal of validation is to correctly represent the elevation of the water, β is kept at 0.80 for further simulations and it is accepted that the velocity profile of the water is not optimally represented. What this means for the degree to which the numerical flow can be seen as turbulent can be found in the conclusions.

4.2.2. GATE MODEL

The development of the water elevation over the length of the flume in time for different gate configuration and dimensions obtained from Table 3.3, are given in Figure 4.19. It can be seen that for each gate configuration the numerical water elevation upstream of the gate doesn't properly match the measured water elevation upstream of the gate. The water downstream also doesn't coincide, but isn't considered interesting in the context of plastic accumulation.

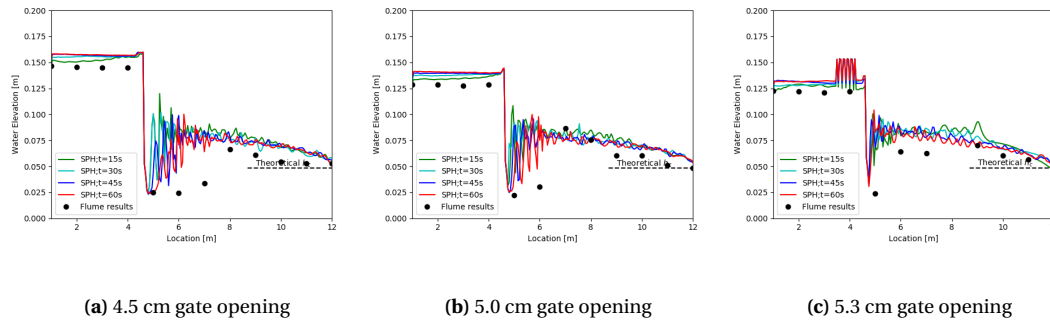


Figure 4.19: Water elevation development for different gate configurations $\beta = 0.8$

It was noted that the model is very sensitive to the gate opening height, so this parameter was slightly changed until the numerical and experimental water elevations in front of the gate matched. The bottom of the gate is also altered, so that the distance between the top of the gate opening and the water surface stays the same. The development of the water elevation over the length of the flume in time for slightly altered gate configuration are given in Figure 4.20. It can be seen that for each gate configuration the numerical water elevation upstream of the gate coincides with the measured water elevation upstream of the gate.

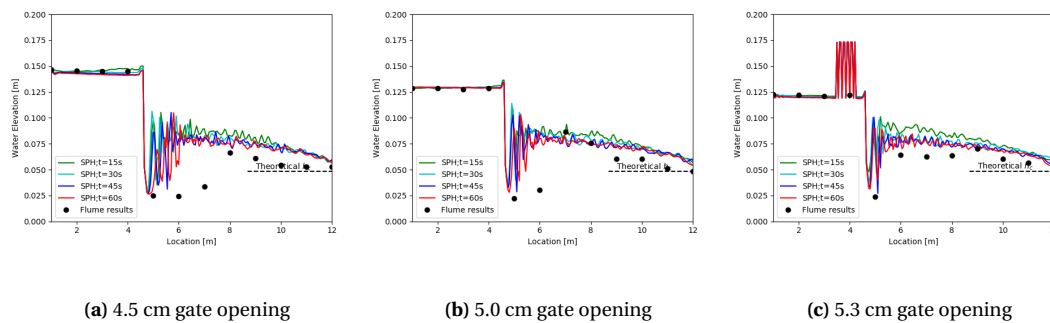


Figure 4.20: Water elevation development for different gate configurations $\beta = 0.8$ with slightly altered gate

The sensitivity analysis shows that with regard to the water elevation, the viscosity coefficient viscosity boundary coefficient β has significantly less influence in contrast to the no-gate model. This is logical as the restriction caused by presence of the gate can be assumed to have a lot more influence on the local (de)acceleration of the flow than the viscosity or bottom friction of the model. Furthermore, from experimental research it can be derived that the water depths in front d_1 and behind the gate d_2 are not depended on these factors, see Equation 2.17.

5

RESULTS

In this chapter, the numerical results of adding plastic fragments to the validated flow in the presence of the sluice gate, as described in [Subsection 4.2.2](#), are presented. First, per test set-up it is examined whether plastic fragments pass through the gate or are retained in front of it; the resulting passing ratio PR and floating carpet length L_c are compared with the experimental results. For each fragment type per gate configuration, the best scenario is recommended, which contains the most similar fragment dynamics compared to its experimental counterpart. These scenarios are then used for the mixed fragment simulation in [Section 5.2](#).

5.1. TEST SET UP & SCENARIO'S

In total, 12 test set-ups are treated, as for each of the 4 different fragment types, 3 gate configurations are examined. The experimental pass ratios and carpet lengths are given in [Table 5.1](#) and [Table 5.2](#).

Gate opening	Red	Yellow	Blue	Green
45 mm	0%	0.5%	52%	100 %
50 mm	0%	2.5 %	92%	100 %
53 mm	1 %	2 %	99%	100 %

Table 5.1: Average passing ratios PR by item per gate configuration extracted from experimental data

Gate opening	Red	Yellow	Blue	Green
45 mm	49.6 cm	13.2 cm	8.4 cm	0 cm
50 mm	48.7 cm	15.3 cm	7.8 cm	0 cm
53 mm	43.6 cm	8.8 cm	2.4 cm	0 cm

Table 5.2: Average carpet length L_c by item per gate configuration extracted from experimental data

For each test set-up 4 numerical scenarios are executed, which are presented in [Table 5.3](#). Each scenario is defined by a combination of a certain density and restitution coefficient. The densities used are the experimental densities ρ_{exp} and the numerically validated densities ρ_{num} for a smoothing coefficient C_h for 1.0, which can be found in [Table 4.1](#). The restitution coefficient e used are 0.60 and 0.75. Numerical simulations are considered failures if fragments are excluded from the domain and/or lose their shape due to heavy collisions (f.e. [Figure D.9a](#)). Simulations failures are marked with a black bar in the graphs and with a 'X' in the tables. Carpets are considered unstable if at the end of the simulation ($t=40$ s), fragments in the carpet are still rearranging, therefor continuously changing the carpet length (f.e. [Figure D.3b](#)). Simulations with unstable carpets are marked with an exclamation mark '!' in the tables.

Scenario	Fragment density	Restitution coefficient
1	ρ_{num}	$e = 0.60$
2	ρ_{num}	$e = 0.75$
3	ρ_{exp}	$e = 0.60$
4	ρ_{exp}	$e = 0.75$

Table 5.3: Overview numerical scenarios

5.1.1. RED FRAGMENTS

The results of the flume experiments with red fragments are characterized by minimal passing ratio's and long carpet lengths, due to the high rising velocity (or low densities) of these fragments. The top view of the carpet formation of the red fragments for each gate configuration accompanied with the associated carpet length is shown in [Figure 5.1](#).

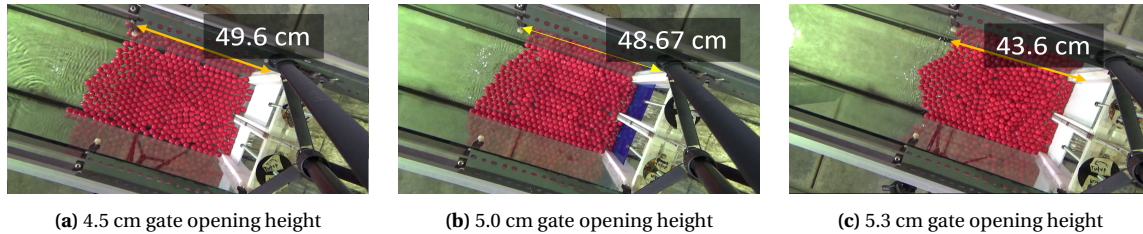


Figure 5.1: Top view of red fragment carpets for different gate opening heights

The side view of the carpet formation of the red fragments for each gate configuration is shown in [Figure 5.2](#). [Figure 5.2a](#) shows that the fragments are mainly not stacking. [Figure 5.2b](#) shows that some fragments are stacking. [Figure 5.2c](#) shows that more fragments are stacking.

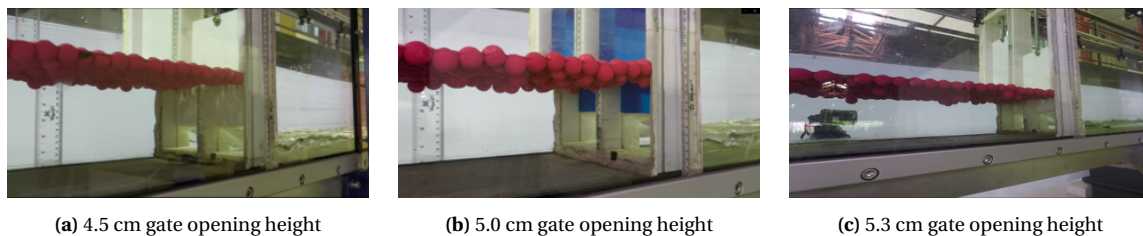


Figure 5.2: Side view of red fragment carpets for different gate opening heights

The final carpet situations ($t = 40$ s) of all the numerical scenarios for the red fragments are presented in [Section D.1](#). From these figures, the passing ratios and carpet lengths of all the numerical scenarios for the red fragments can be determined, which are presented in [Table 5.4](#) and [Table 5.5](#).

	Gate opening 4.5 cm		Gate opening 5.0 cm		Gate opening 5.3 cm	
	$e = 0.60$	$e = 0.75$	$e = 0.60$	$e = 0.75$	$e = 0.60$	$e = 0.75$
ρ_{num}	0 %	0 %	0 %	X	0 %	0 %
ρ_{exp}	0 %	0 %	0 %	0 %	22 %	0 %

Table 5.4: Numerical passing ratio's PR for red fragments

	Gate opening 4.5 cm		Gate opening 5.0 cm		Gate opening 5.3 cm	
	$e = 0.60$	$e = 0.75$	$e = 0.60$	$e = 0.75$	$e = 0.60$	$e = 0.75$
ρ_{num}	57.4 cm	57.6 cm (!)	57.7 cm	X	48.1 cm	43.9 cm (!)
ρ_{exp}	58.2 cm	48.3 cm	58.4 cm	43.8 cm	42.4 cm	31.5 cm

Table 5.5: Carpet lengths L_c red fragments

All simulations were executed successfully, except for gate opening 5.0 cm - scenario 2 (Figure D.3b). It shows a highly unstable carpet in which some plastic fragments increased in size. For scenario 1, it is shown that the passing ratios are zero and the carpets barely stack regardless of gate opening height (Figure D.1a, Figure D.3a and Figure D.5a). Although by increasing gate opening height from 5.0 to 5.3 cm, it is observed that stacking somewhat increases right in front of the gate. For scenario 2, By increasing the restitution coefficient, in comparison to scenario 1, it is observed that the carpet becomes unstable regardless of gate opening height (Figure D.1b, Figure D.3b and Figure D.5b). By increasing the gate opening height, this instability only increases further. For scenario 3, by increasing density compared to scenario 1, it is observed that the length and shape of the carpet remain similar for a gate opening height of 4.5 or 5.0 cm (Figure D.2a and Figure D.4a). However, for a gate opening height of 5.3 cm (Figure D.6a), the stack of fragments in front of the gate eventually passes through the gate. For scenario 4, by increasing the restitution coefficient compared to scenario 3, it is observed that the carpets become shorter as they start to stack (Figure D.2b, Figure D.4b and Figure D.6b). By increasing the gate opening height, the amount of stacking increases significantly. By increasing the density compared to scenario 2, it is observed that the carpets become less unstable. In order to compare the numerical values better to the experimental values and recommend one scenario; The data from Table 5.4 and Table 5.5 is visualized using a bar chart in Figure 5.3 and Figure 5.4.

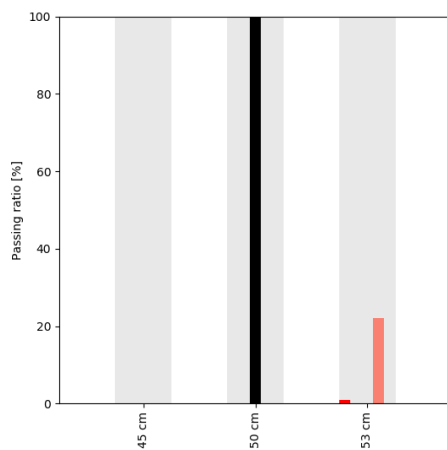


Figure 5.3: Bar chart of passing ratio's for red fragments

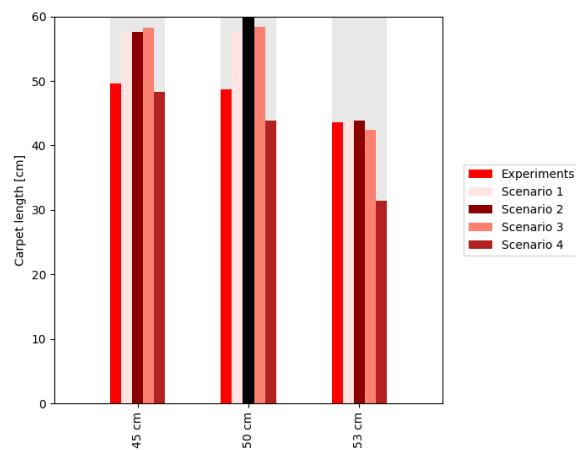


Figure 5.4: Bar chart of carpet lengths for red fragments

It is shown that for every gate configuration, almost every successfully executed scenario has a 0 % passing ratio. So on the basis of passing ratio's it's hard to recommend a specific scenario. It is shown that for a gate opening of 4.5 and 5.0 cm, scenario 4 is the most in agreement with the experimental carpet lengths and carpet shapes (Figure D.2b and Figure D.4b). For a gate opening of 5.3 cm, scenario 2 and 3 (Figure D.5b and Figure D.6a) are most in agreement with the experimental carpet lengths. scenario 3 is chosen over scenario 2, as the carpet of scenario 3 may show less stacking and is partly shorter as it should because some fragments passed the gate, however the carpet of scenario 2 is highly unstable. The final carpet formations of the scenarios, which are the best in agreement with the experimental results, are presented in Figure 5.5.

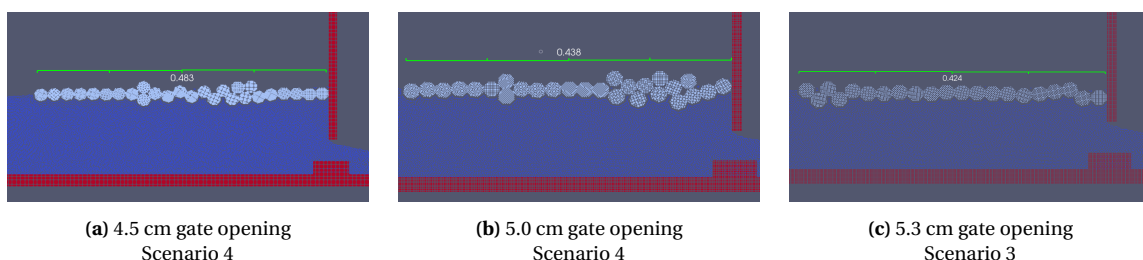
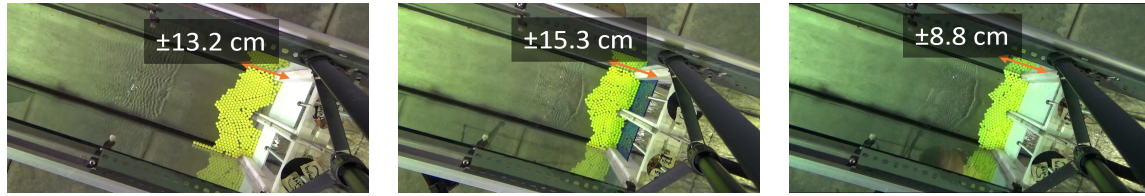


Figure 5.5: Final numerical carpet formation for red fragments

5.1.2. YELLOW FRAGMENTS

The results of the flume experiments with yellow fragments are characterized by minimal passing ratio's and shorter carpet lengths because of more interlocking in comparison to the red fragments. The top view of the carpet formation of the yellow fragments for each gate configuration accompanied with the associated carpet length is shown in [Figure 5.6](#).



(a) 4.5 cm gate opening height

(b) 5.0 cm gate opening height

(c) 5.3 cm gate opening height

Figure 5.6: Top view of yellow fragment carpets for different gate opening height

The side view of the carpet formation of the yellow fragments for each gate configuration is shown in [Figure 5.7](#). [Figure 5.7a](#) shows that the fragments are not stacking. [Figure 5.7b](#) shows that several fragments are stacking. [Figure 5.7c](#) shows that most fragments are stacking.



(a) 4.5 cm gate opening height

(b) 5.0 cm gate opening height

(c) 5.3 cm gate opening height

Figure 5.7: Side view of yellow fragment carpets for different gate opening height

The final carpet situations ($t = 40$ sec) of all the numerical scenarios for the yellow fragments are presented in [Section D.2](#). From these figures, the passing ratios and carpet lengths of all the numerical scenarios for the yellow fragments can be determined, which are presented in [Table 5.6](#) and [Table 5.7](#).

	Gate opening 4.5 cm		Gate opening 5.0 cm		Gate opening 5.3 cm	
	$e = 0.60$	$e = 0.75$	$e = 0.60$	$e = 0.75$	$e = 0.60$	$e = 0.75$
ρ_{num}	0 %	0 %	X	X	X	X
ρ_{exp}	0 %	0 %	0 %	X	0 %	X

Table 5.6: Passing ratio's PR yellow fragments

	Gate opening 4.5 cm		Gate opening 5.0 cm		Gate opening 5.3 cm	
	$e = 0.60$	$e = 0.75$	$e = 0.60$	$e = 0.75$	$e = 0.60$	$e = 0.75$
ρ_{num}	17.0 cm	16.7 cm	X	X	X	X
ρ_{exp}	17.6 cm	17.6 cm	16.4 cm	X	13.8 cm (!)	X

Table 5.7: Carpet lengths L_c yellow fragments

Many simulations were executed unsuccessfully. For scenarios 1, 2 and 4 with gate openings of 5.0 and 5.3 cm (Figure D.9a, Figure D.9b, Figure D.10b, Figure D.11a, Figure D.11b and Figure D.12b), it is observed that fragments deform heavily and are even launched out of bounds. All four scenarios can only be successfully executed for a gate opening of 4.5 cm. For this gate configuration, it is observed that the carpet lengths of the higher densities scenarios 3 and 4 (Figure D.8a and Figure D.8b) are slightly longer than those of the lower-density scenarios 1 and 2 (Figure D.7a and Figure D.7b), due to the small gap between the fragments and the gate. Moreover, the shape or amount of stacking does not change with increasing density or restitution coefficient. Furthermore, only scenario 3 gave successful results for all gate configurations. For scenario 3, the carpet lengths decrease slightly with increasing gate opening height. As for a gate opening of 5.0 cm (Figure D.10a), the fragments compress more against each other in and as for a gate opening of 5.3 cm (Figure D.12a), the fragments would eventually. The data from Table 5.6 and Table 5.7 is visualized with means of bar chart in Figure 5.8 and Figure 5.9.

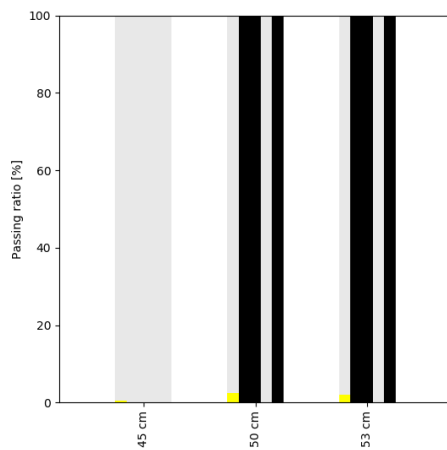


Figure 5.8: Bar chart of passing ratio's for yellow fragments

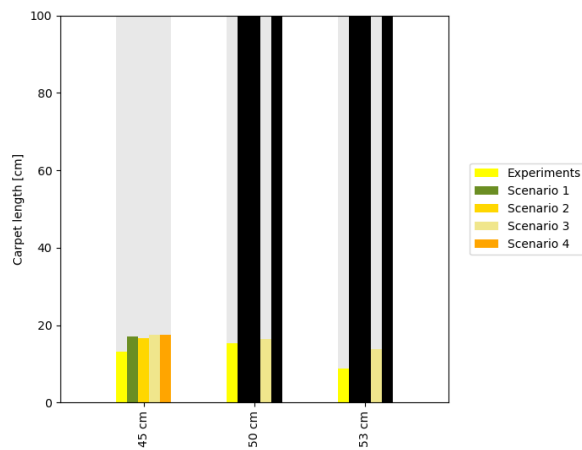


Figure 5.9: Bar chart of carpet lengths for yellow fragments

It is shown that for every gate configuration, every successfully executed scenario has a 0 % passing ratio, which aren't in agreement with the small passing ratio's of the experiments. So on the basis of passing ratio's no distinction in preference can be made between scenario's. This also holds for the carpet lengths and shapes, as there is almost no difference to be found between scenario's for gate opening 4.5 cm. So, the preference is again based on stability for scenario 3. The final carpet formations of the scenarios, which are the best in agreement with the experimental results, are presented in Figure 5.10.

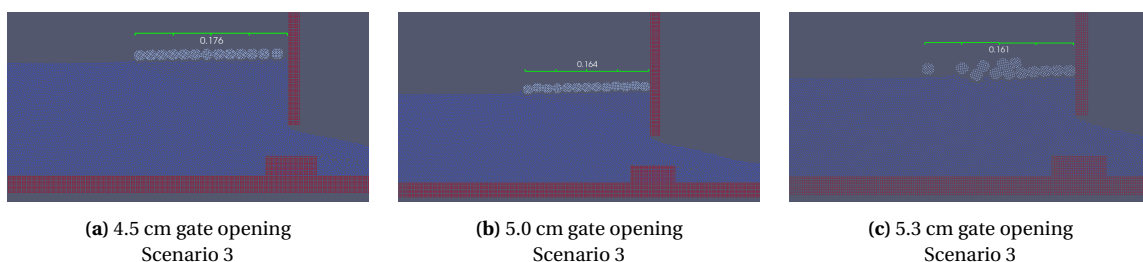


Figure 5.10: Final numerical carpet formation for yellow fragments

5.1.3. BLUE FRAGMENTS

The results of flume experiments with blue fragments are characterized by significant differences in passing ratios and carpet lengths between different gate configurations. The carpet formation of the blue fragments for each gate configuration can be seen in [Figure 5.11](#).

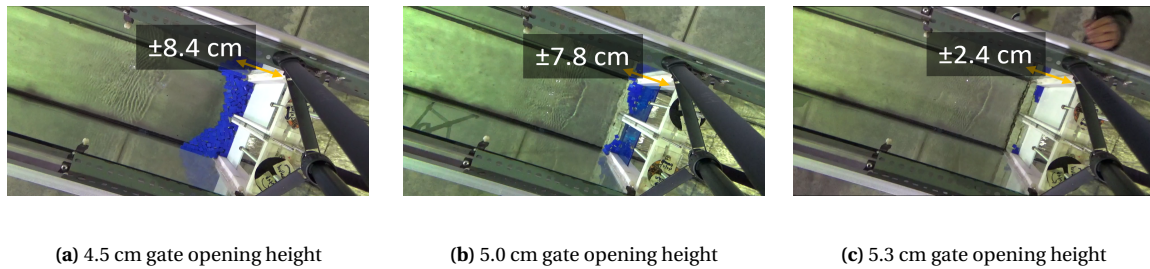


Figure 5.11: Top view of blue fragment carpets for different gate opening height

The side view of the carpet formation of the blue fragments for each gate configuration is shown in [Figure 5.12](#). [Figure 5.12a](#) shows that most of the fragments that did not pass through the gate stack. [Figure 5.12b](#) shows that none of the fragments that did not pass through the gate stack. [Figure 5.12c](#) shows that there are not enough fragments to stack.

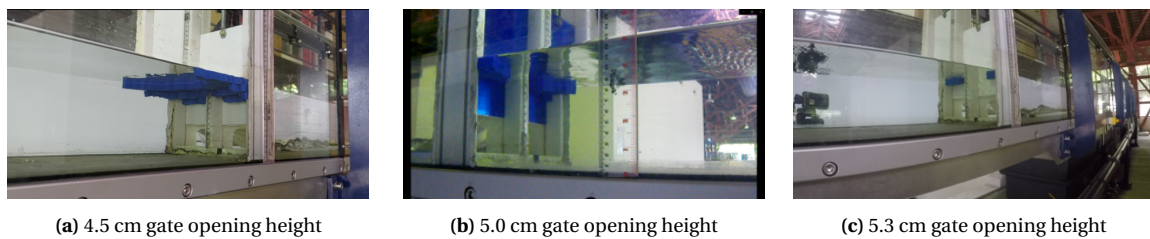


Figure 5.12: Side view of blue fragment carpets for different gate opening height

The final carpet situations ($t = 40$ s) of all the numerical scenarios for the blue fragments are presented in [Section D.3](#). From these figures, the passing ratios and carpet lengths of all the numerical scenarios for the blue fragments can be determined, which are presented in [Table 5.8](#) and [Table 5.9](#).

	Gate opening 4.5 cm		Gate opening 5.0 cm		Gate opening 5.3 cm	
	$e = 0.60$	$e = 0.75$	$e = 0.60$	$e = 0.75$	$e = 0.60$	$e = 0.75$
ρ_{num}	0 %	0 %	0 %	0 %	94 %	0 %
ρ_{exp}	0 %	0 %	X	88 %	100 %	94 %

Table 5.8: Passing ratio's PR blue fragments

	Gate opening 4.5 cm		Gate opening 5.0 cm		Gate opening 5.3 cm	
	$e = 0.60$	$e = 0.75$	$e = 0.60$	$e = 0.75$	$e = 0.60$	$e = 0.75$
ρ_{num}	24.0 cm	23.2 cm	21.8 cm	19.2 cm	1.2 cm	17.8 cm (!)
ρ_{exp}	27.1 cm	24.2 cm	X	1.2 cm	0 cm	1.2 cm

Table 5.9: Carpet lengths L_c blue fragments

All simulations were executed successfully, except for gate opening 5.0 scenario 3 (Figure D.16a). It is observed that the fragments block the gate opening by clumping together, causing the simulation to crash. For a gate opening of 4.5 cm, the passing ratios are zero regardless of the scenario. It is observed that the carpet lengths of the higher densities scenarios 3 and 4 (Figure D.14a and Figure D.14b) are slightly longer than the lower densities scenarios 1 and 2 (Figure D.13a and Figure D.13b), as the fragments are more spread out over the length over the carpet. Furthermore, the shape or amount of stacking barley changes with increasing restitution coefficient. When increasing the gate opening to 5.0 cm, it is observed that the gap between the gate and the carpet of the lower densities scenarios 1 and 2 (Figure D.15a and (Figure D.15b) and disappears. For Scenario 2, by increasing the restitution coefficient in comparison with scenario 1, it is shown that carpet starts to stack. By increasing the gate opening to 5.3 cm, it is observed that for scenarios 1, 3 and 4 (Figure D.17a, Figure D.18a and Figure D.18b) almost all fragments pass the gate. However, for Scenario 2 (Figure D.17b), by increasing restitution coefficient in comparison with Scenario 1, the carpet becomes unstable. The data from Table 5.8 and Table 5.9 is visualized using a bar graph in Figure 5.13 and Figure 5.14.

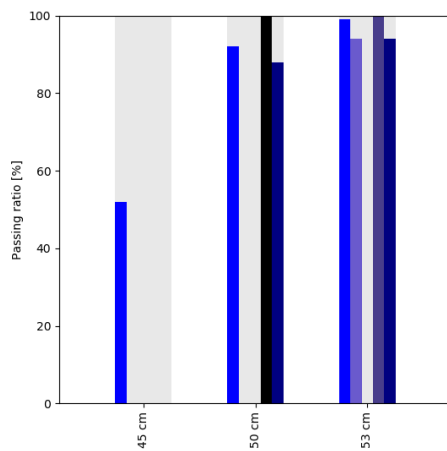


Figure 5.13: Bar chart of passing ratio's for blue fragments

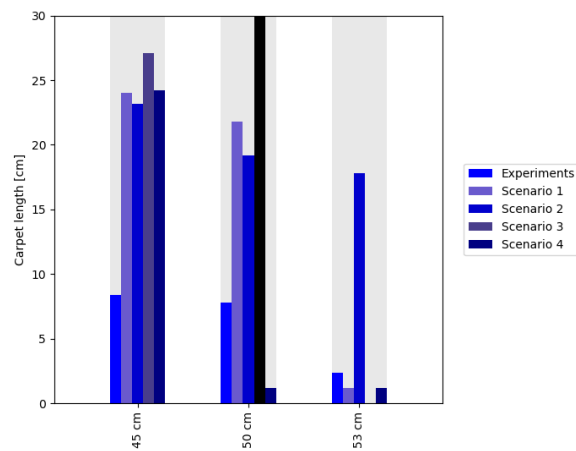


Figure 5.14: Bar chart of carpet lengths for blue fragments

It is shown, that for a gate opening of 4.5 cm, all scenario's (Figure D.13a, Figure D.13b, Figure D.14a and Figure D.14b) have similar passing ratios and carpet lengths, which aren't in agreement with the experimental results. For a gate opening of 5.0, the passing ratio of scenario 4 (Figure D.16b) is most in agreement with the experimental passing ratio. For a gate opening of 5.3, scenarios 1 and 4 (Figure D.17a and Figure D.18b) have similar passing ratio's and carpet lengths and are the most in agreement with the experimental results. The final carpet formations of the scenarios, which are the best in agreement with the experimental results, are presented in Figure 5.15.

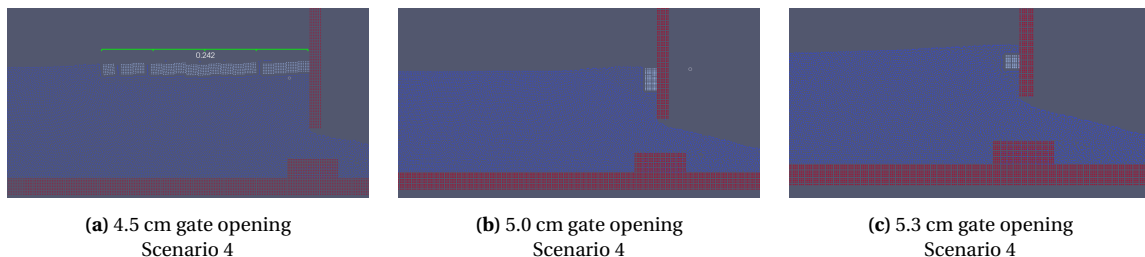


Figure 5.15: Final numerical carpet formation for blue fragments

5.1.4. GREEN FRAGMENTS

The results of the flume experiments with green fragments are characterized by maximal passing ratios and the absence of carpets in front of the gate, due to the low rising velocity of these fragments. In contrast to the other fragments, green fragments approaching the gate don't only travel over the free-surface, as shown in [Figure 5.16](#). At the gate, it is observed that fragments can shortly be trapped in so-called 'vortex areas', which is shown in [Figure 5.17](#).



Figure 5.16: Green particles in flume



Figure 5.17: Vortex areas in front of the gate

The final carpet situations ($t = 40$ s) of all the numerical scenarios for the green fragments are presented in [Section D.4](#). From these figures, the passing ratios and carpet lengths of all the numerical scenarios for the green fragments can be determined, which are presented in [Table 5.10](#) and [Table 5.11](#).

	Gate opening 4.5 cm		Gate opening 5.0 cm		Gate opening 5.3 cm	
	$e = 0.60$	$e = 0.75$	$e = 0.60$	$e = 0.75$	$e = 0.60$	$e = 0.75$
ρ_{num}	0 %	0 %	0 %	0 %	0 %	8 %
ρ_{exp}	0 %	62 %	100 %	77 %	100 %	100 %

Table 5.10: Passing ratio's PR green fragments

	Gate opening 4.5 cm		Gate opening 5.0 cm		Gate opening 5.3 cm	
	$e = 0.60$	$e = 0.75$	$e = 0.60$	$e = 0.75$	$e = 0.60$	$e = 0.75$
ρ_{num}	18.7 cm	18.7 cm	14.6 cm	13.9 cm	10.7 cm	12.3 cm (!)
ρ_{exp}	20.4 cm	10.9 cm	0 cm	5.5 cm	0 cm	0 cm

Table 5.11: Carpet lengths L_c green fragments

All simulations were executed successfully. For a gate opening of 4.5 cm, the passing ratios of all scenarios are 0 %, except for scenario 4 ([Figure D.20b](#)). The lower densities scenario's 1 and 2 ([Figure D.19a](#) and [Figure D.19b](#)) have a near identical carpet length and shape. By increasing the density ([Figure D.20a](#) and [Figure D.20b](#)), it is observed that the gap between the gate and the fragments disappears, but the fragments are more spread over the carpet. By increasing the gate opening to 5.0 cm, it is observed that the gap between gate and the carpet of the lower densities scenarios 1 and 2 ([Figure D.21a](#) and [Figure D.21b](#)) disappears and therefore the carpets get shorter. For scenario 2, by increasing the restitution coefficient in comparison with scenario 1, it is shown that there isn't an increasing of stacking of the carpet. Furthermore, by increasing the densities for scenarios 3 and 4 ([Figure D.22a](#) and [Figure D.22b](#)) the passing ratios increase. By increasing the gate opening to 5.3 cm, it is observed the carpets get shorter for the lower densities scenarios 1 and 2 ([Figure D.21a](#) and [Figure D.21b](#)). This is caused by fragments adhering to the gate for scenario 1 and the carpet becoming unstable for scenario 2 by

increasing the restitution coefficient. By increasing the density, it is observed that all the fragments pass the gate for scenarios 3 and 4 (Figure D.24a and Figure D.24b). The data from Table 5.10 and Table 5.11 is visualized with means of bar chart in Figure 5.18 and Figure 5.19.

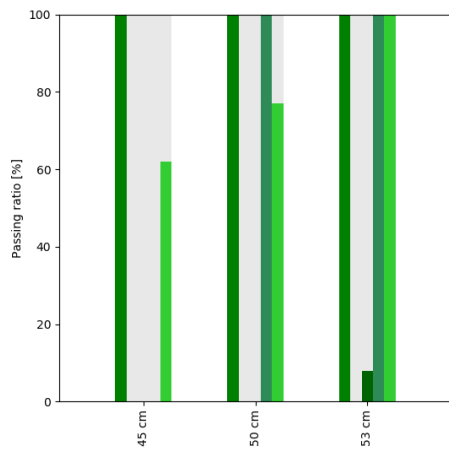


Figure 5.18: Bar chart of passing ratio's for green fragments

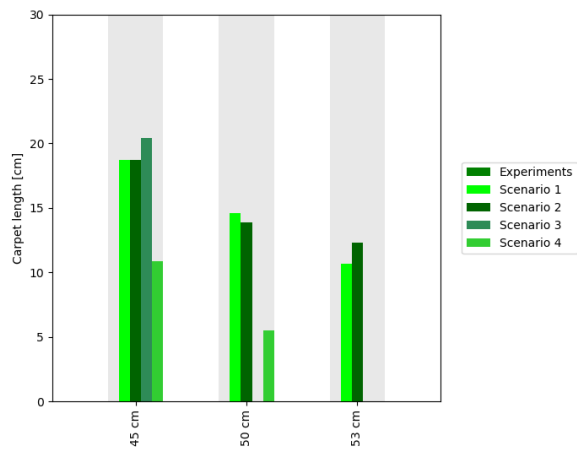


Figure 5.19: Bar chart of carpet lengths for green fragments

None of the scenario's have a 100 % passing ratio for all the gate configurations corresponding with the experimental results. For a gate opening of 4.5 cm, scenario 4 (Figure D.20b) has the highest passing ratio and the shortest carpet length. For a gate opening of 5.0 cm, scenario 3 (Figure D.22a) is in agreement with the experimental results. For a gate opening of 5.3 cm, scenario 3 (Figure D.24a) and 4 (Figure D.24b) are in agreement with experimental results. The final carpet formations of the scenarios, which are the best in agreement with the experimental results, are presented in Figure 5.20.

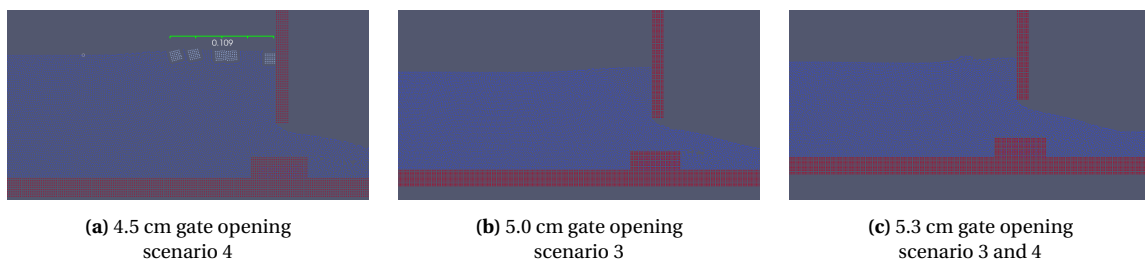


Figure 5.20: Final numerical carpet formation for green fragments

5.2. MIXTURE OF FRAGMENTS

There are two methods in which a mixture of different types of fragments can be released into the flume; The fragments can be first mixed in a bucket and then released into the flume, or they can be released in a sequence one-by-one per fragment type. In this case, the sequence of release is from the fragment type with the highest rising velocity to the fragment type with the lowest rising velocity, so Red-Yellow-Blue-Green. The carpet formation and carpet length of a mixture of fragments released one-by-one for each gate configuration is shown in [Figure 5.21](#).

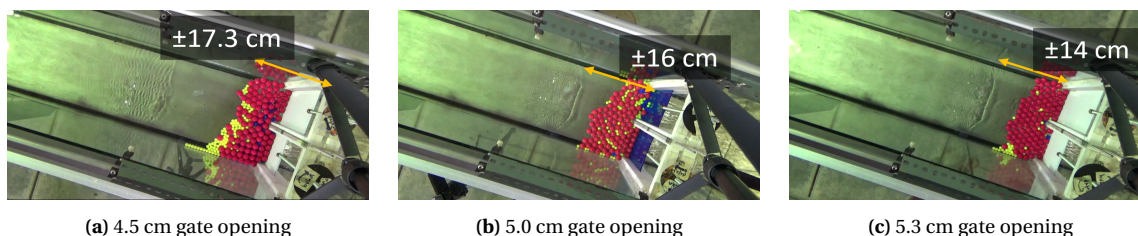


Figure 5.21: Mix carpet for different gate openings Top view

The carpet formation of a mixture of fragments released with the bucket method for each gate configuration can be seen in [Figure 5.22](#). By comparing [Figure 5.21a](#) and [Figure 5.22a](#), it is shown that for the 4.5 cm gate opening scenario, there is a significant difference in carpet length between the one-by-one method and the bucket method. However, by comparing [Figure 5.21c](#) and [Figure 5.22b](#), it is shown that for the 5.3 cm gate opening scenario, the carpet lengths are more or less the same. Furthermore, the fragment distribution in the carpet is more random in the bucket method than in the one-by-one method.

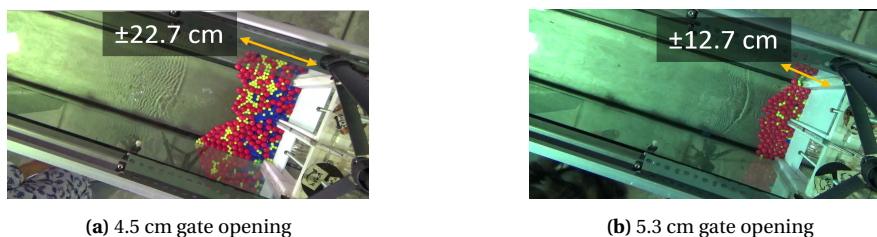


Figure 5.22: Mix carpet for different gate openings Top view

The side view of the carpet formation of a mix of fragments released one by one for each gate configuration is shown in [Figure 5.23](#). [Figure 5.23a](#) shows that many blue fragments stacked below the carpet against the gate. [Figure 5.23b](#) shows that most blue fragments have been replaced by yellow fragments. [Figure 5.23c](#) shows that the carpet has a similar shape as [Figure 5.23b](#).

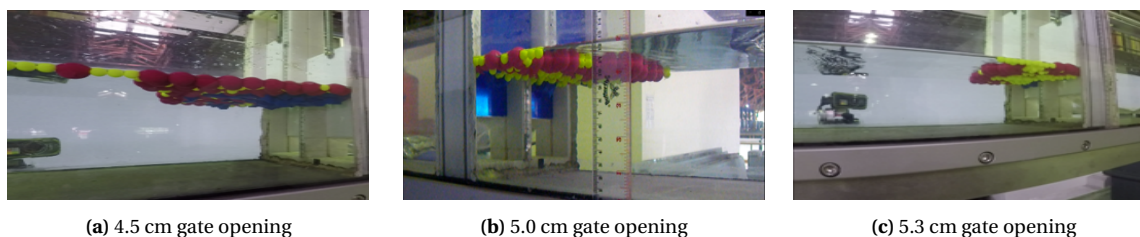


Figure 5.23: Mix fragment carpet for different gate openings

The pass ratios extracted from the experimental data for each fragment type within the mix is presented in [Table 5.12](#). The numerical scenarios which were used for each fragment type and gate configuration are presented in [Table 5.13](#).

Gate opening	Red	Yellow	Blue	Green
45 mm	0%	0%	17%	100 %
50 mm	0%	26 %	88%	100 %
53 mm	0%	6 %	97%	100 %

Table 5.12: Pass ratios PR results by item in mix per configuration from experimental data

Gate opening	Red	Yellow	Blue	Green
45 mm	4	3	4	4
50 mm	4	3	4	3
53 mm	3	3	4	4

Table 5.13: Scenario used by item in mix per configuration in numerical research

The resulting pass ratios and carpet lengths are visualized by means of bar chart in Figure 5.24 and Figure 5.25. Where per gate configuration, the left bar represents the experimental results and the right bar the numerical results. The final carpet formations for each gate configuration are presented in Figure 5.26.

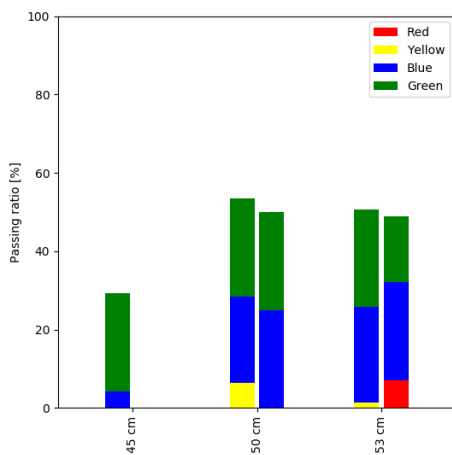


Figure 5.24: Bar chart of passing ratios for mixed fragments

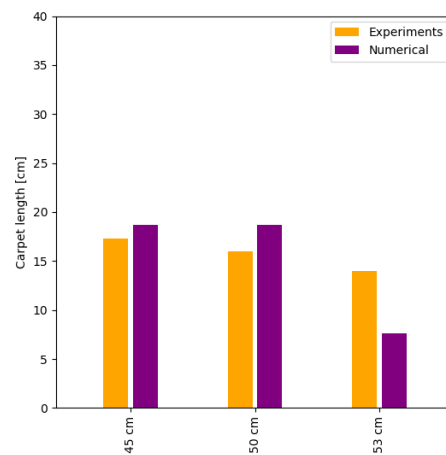


Figure 5.25: Bar chart of carpet lengths for mixed fragments

For a gate opening height of 4.5 cm, it is shown that the passing ratios are not in agreement, as none of the green or blue fragments in the numerical simulation pass the gate. The carpet lengths are more in agreement, as the blue and green fragments stack under the carpet. However, the location of stacking is different, as in the experiments the blue fragments are stacked against the gate, and in the numerical simulations on the other side of the carpet. For a gate opening of 5.0 cm, the passing ratios are more in agreement as the green and blue fragments pass the gate. The carpet of the numerical simulation is longer than the experiment, because there is less stacking. For a gate opening of 5.3 cm, it is shown that especially the carpet lengths are not in agreement. Because in the numerical simulation the carpet partly collapses, as the red fragments are pushed against the gate, even entrapping a green fragment, drastically reduces the carpet length.

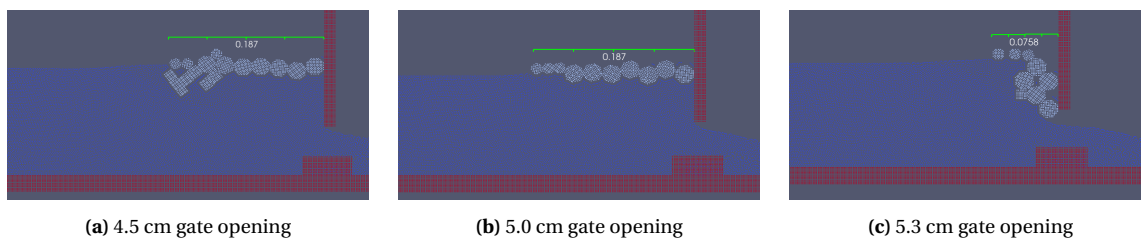


Figure 5.26: Final numerical carpet formation for mixed fragments

6

DISCUSSION

In this chapter, the results presented in the previous chapter are discussed. Parameters with the highest degree of influence are presented. Lastly, limitations are provided with respect to the representation of fluid and plastic debris dynamics of the numerical model.

6.1. INFLUENCE GATE OPENING HEIGHT

In experimental research, it was found that with an increase in the opening of the gate height, the passing ratio will increase (Table B.9) and the carpet lengths decrease (Table B.10). An anomaly was found, for the carpet length of the yellow fragments with a gate opening of 5.0 cm is longer than the carpet with a gate opening of 4.5 cm. In numerical research, the same relationship was found for all combinations of scenarios and fragment types. Except for some small anomalies, as for scenario 1 and 3, the carpet of the red fragments with a gate opening of 5.0 cm (Figure D.3a and Figure D.4a) is slightly longer than the carpet with a gate opening of 4.5 cm (Figure D.1a and Figure D.2a). This can be explained by the fact, that fragments with the larger gate opening depth are more influenced by the velocity field than the fragments with smaller gate opening depth. Until this influence is large enough for the fragments to start stacking or moving past the gate, as with a gate opening of 5.3 cm (Figure D.5a and Figure D.6a), the fragments will be slightly less stacked and therefore increasing its length. It was found that for scenario 2, an increase in gate opening depth would lead to an eventual increase in carpet instability for all types of fragment. This in contrast with scenario 4 for red fragments for example, where an increase in gate opening height leads to a stable increase of stacking. This difference in outcome can be explained by the difference in density between scenarios. As it is observed, that with an increase in opening height, a change in density will lead to a abrupt transition between a stable stacked carpet and an unstable carpet.

Lastly, it could be argued that it is not the inherent increase in gate opening height itself, which increases the passing ratio and decreases carpet length, but rather the resulting decrease of water elevation in front of the gate. This means that the distance between the plastic fragments in the carpet and the top of the gate opening becomes smaller and therefore the fragments are more influenced by the flow velocity field of the gate opening.

6.2. INFLUENCE RISING VELOCITY AND DENSITY

As obviously expected, in experimental and numerical research it was found that with a decrease of rising velocities between fragment types, the passing ratios will increase and the carpet length will decrease. However, in numerical research, some anomalies were found. For scenario 3, the passing ratio for red fragments is higher than yellow fragments with a gate opening 5.3 cm (Figure D.6a and Figure D.12a). For scenario 4, the passing ratios for blue fragments are higher than those for green fragments with gate opening 5.0 cm (Figure D.16b and Figure D.22b) and for scenario 1 with gate opening 5.3 cm (Figure D.17a and Figure D.23a). It is shown in Figure D.25, Figure D.26 and Figure D.27. It is observed that the mechanism of fragments for every anomaly is in principle similar; the fragments seem to be at the precise point, where fragments are adhesive enough to be pulled by the stream as one whole through the gate, but not adhesive enough for the carpet to keep its shape (akin Figure D.6b).

It was found that scenarios 1 and 2, which use the densities validated by the buoyancy tests, are often less in agreement with the experimental results as scenarios 3 and 4, which use the densities used in the experimental research directly. This is especially the case for fragments trying to pass the gate. This can be explained by the 'depth dependency' of the plastic fragments, which was found in the validation of the buoyancy tests [Section 4.1](#). Where it was shown, that the deeper the fragment is under water, the more the rising velocity of the fragments decreases. As for the flume experiments, the water depth is smaller than the water depth of the buoyancy tests and the plastic fragments are released on the water surface instead down at the bottom, and the rising velocity is relatively higher for the flume experiments. Therefore it can be explained why scenario 3 and 4 work better, as those have a higher density which decreases the rising velocity.

Furthermore, it was found that lower density scenarios and fragments are more susceptible for carpet instability than higher densities scenario's and/or fragments. For the yellow fragments, which have the lowest density of all the fragments types, half of the total amount of simulations couldn't be fully executed due to carpet instability. For red fragments, it was found that by increasing the density for scenario 4 in comparison to scenario 2, the carpet would become more stable. This can be explained because, for lower densities scenarios and/or fragments, the relative impact of kinetic interactions between fragments is larger than for higher densities scenarios and/or fragments, making the carpet more unstable.

6.3. INFLUENCE RESTITUTION COEFFICIENT

The influence of the restitution coefficient was found to be highly sensitive to the amount of potential energy in the system. Which is consistent with expectations, since the restitution coefficient works as a multiplier when this potential energy is converted in kinetic interactions ([Equation 2.35](#)). For example, it is shown that for red fragments, that with an increase in opening height, an increase in restitution coefficient will lead to more unstable carpet. As for larger gate opening heights, the velocity on the water surface is higher than for smaller gate opening heights, so more shear stress is exerted on the fragments in the carpet.

The found sensitivity of carpet stability of the combination of fragments density, restitution coefficient and gate opening height can best be displayed by examining the extremes. For yellow fragments, scenario 3 was the only scenario that produced stable carpets for each gate opening height, since this scenario has the highest density and the lowest restitution coefficient. On the other side, for a gate opening of 5.3 cm, scenario 2 was the only scenario that produced unstable carpet for every fragment type, as this scenario has the lowest density and highest restitution coefficient.

Furthermore, it was found that the restitution coefficient has a large influence on the way individual fragments interact with each other. For low restitution coefficients, fragments often pass through the gate because they are adhesive and hence are being pulled as one whole through the gate. Between fragments retained in front of the gate, there is often too much friction for fragments to slide over or under each other to stack, leading to longer carpet. For high restitution coefficients, fragments often pass the gate because individual collisions push them into the velocity field near the gate. Between fragments retained in front of the gate, there is often less friction, so fragments can slide over and over each other to stack, leading to shorter carpets. No clear correlation was found between an increase in the restitution coefficient and an increase in the passing ratio. Lastly, it is generally observed in the numerical simulations, that individual fragments often stack on top in the present carpet (f.e. [Figure D.12a](#)). However, in experimental tests, individual fragments are observed to often stack below the carpet (f.e. [Figure 5.2c](#))

6.4. LIMITATIONS

For the experimental research, the conditions of the flume experiments are limited in representing the conditions of a natural riverine environment. In the flume experiments a steel bottom is used to represent the riverbed, however steel is significantly smoother and therefore generates less turbulence than a normal river bed. Also a constant discharge was present in the flume, however in reality discharge is always varied. Furthermore, rivers are not perfectly straight as the flume is, as bends in the river affect the horizontal and vertical plastic distribution of plastic fragments. This distribution is also affected by the application of wind on the free surface, all these factors weren't considered in this report. The plastic debris released in the flume were signif-

icantly more uniform in shape, density and size than found in reality, which for example excludes important fragment dynamics like entanglement. Lastly, weirs found in riverine system are almost always submerged (see [Figure 1.1](#)) instead of free surface flow weirs used in this report.

For the numerical research, one of the main limitations of the SPH-DEM method is the inability to properly design models in a high-resolution and/or 3D environment, due to high computational costs. These costs also limit the size of the simulation domain and the possible simulation time. Furthermore, the method is unable to properly represent turbulent behavior in the flow, due to the low resolution and the lack of available turbulence models. The resolution (0.002 mm) of the model is too low to simulate viscous boundary layer and buffer layer of a typical turbulent velocity profile. However the processes that are investigated mostly occur in the upper part of the flow, hence some minor discrepancies in the lower part of the flow are acceptable. Low resolution also affects fragment design, as only simple shapes can be simulated presently.

It is possible that the restitution coefficients used in the numerical simulations, which obtain the best results in representing realistic carpet formations and individual fragment interactions, have a significant higher values ($e=0,75$) that found in the experiments. This may possibly be explained due to the lack of turbulence imposed in SPH. As in normal conditions, turbulence creates more energetic interactions between the fragments. To compensate for this, the restitution coefficient has to be increased to get similar results. As with higher restitution coefficients, less energy is dissipated after interactions between fragments. However no restitution coefficients were determined for the experiments, so this would be an interesting topic to research in the future.

7

CONCLUSION & RECOMMENDATIONS

In this chapter, the subquestions and the main research question provided in [Chapter 1](#) are subsequently answered. Finally, recommendations regarding further research are provided, which take in account possible future developments in SPH.

7.1. CONCLUSION

1. How can turbulent open channel flows be sufficiently modeled in SPH?

Currently, there are no sufficiently theoretically supported turbulent models available for SPH in DualSPHysics. However, a method was developed to impose turbulent velocity profiles at the inlet while maintaining continuity. Furthermore, using the artificial viscosity scheme for uniform flows, by adjusting the boundary viscosity coefficient β to 0.1, smooth turbulent velocity profiles were simulated throughout the flume corresponding to theoretical values. The resolution (0.002 mm) of the model is too low to simulate viscous boundary layer and buffer layer of a typical flow field. However the processes that are investigated mostly occur in the upper part of the flow, hence some minor discrepancies in the lower part of the flow are acceptable. For gradually varied flows without gate, by adjusting the boundary viscosity coefficient β to, water elevations were simulated throughout the flume corresponding to theoretical values. However, no single value of β was found in which the velocity profiles of the uniform flow and the water elevation of the gradually varied flows were both in agreement with their theoretical values. For gradually varied flows with gate, it was found that β has less effect on the water elevation as for the previous set ups. The gate opening height had to be adjusted to simulate the water elevations accordingly.

2. How can the buoyancy of individual plastic debris be sufficiently modeled in SPH?

Canelas *et al.* [49] showed that the rising velocities of fragments, which are modeled with relatively high resolution, match the experimental results, and the fragments, which are modeled with a relatively low resolution, do not. A possible explanation is provided in this report, as it was noticed that the effects of numerical diffusion are larger for fragments, which are modeled with relatively low resolution. The larger the numerical diffusion, the larger the change in density and the larger the change in rising velocity. In addition to the physical parameter density, a new numerical parameter was identified which can be adjusted to compensate for the numerical diffusion, namely the smoothing length. Furthermore, it was noticed that the degree of numerical diffusion is dependent on the depth of the fragment in the water. Which explains the seeming difference in buoyancy between the validated plastic fragments released in the numerical buoyancy model and the same fragments released in the numerical flume model, because these models differ in water depth.

3. What are the most important (numerical) parameters affecting the plastic debris accumulation in front of a hydraulic structure in SPH?

For the numerical model, three parameters were identified as having the greatest influence on the passing ratio's and carpet length per simulation; namely, gate height opening, density and restitution coefficient. In experimental and numerical research, it was shown that with an increase in gate height opening and/or decrease in density, the passing ratio will increase and the carpet lengths decrease.

Furthermore, it was noticed that the stability of the plastic carpet also depends on these three parameters. It was shown in numerical research that with an increase in opening height, a change in density or restitution coefficient will lead to an abrupt transition between a stable stacked carpet and an unstable one. Lastly, it was found that the restitution coefficient is integral in the way individual fragments interact with each, which holds for the mechanism in which fragments pass the gate, but also how carpets are formed.

Final Conclusion: How suitable is the SPH-DEM numerical method to model the dynamic processes of plastic debris accumulation against a sluice gate?

At the moment, due to high computational costs, simulations in SPH-DEM are mainly limited to perform in a 2D and a relatively low resolution environment. This means that many physical aspects and dynamics need to be taken into account in the design of the numerical model and compensated for in the validation process. As it was achieved to validate the flow on the basis of water elevation and the fragments on the basis of rising velocities. However, when including fragments in the flow, the absence of turbulence has to be compensated by increasing the density and restitution coefficient, as sufficient easy-to-use turbulence models are still not available. Furthermore, numerical diffusion, dependent on the vertical position of the fragment in the water, changes the rising velocities of which the fragments were validated on before. However, this report has shown that the dynamics of individual fragment interactions play a crucial role in the way fragments pass the gate or in how carpet is formed in the upstream part. As well as in the influence of individual fragment parameters such as the restitution coefficient. For these properties can not be modeled in a traditional CFD model, where the fragments are modeled as a continuum. So in conclusion, SPH-DEM is in principle sufficient for modeling the dynamic processes of the plastic debris accumulation against a sluice gate; however, further improvements in computational power and turbulence models are needed to be more widely applied.

7.2. RECOMMENDATIONS

Regarding experimental research, the buoyancy tests could have been conducted in a bigger tank like Waldschla and Schu [35], which reduces the wall effects and also gives the fragment more time to accelerate, providing more accurate rising velocities. As long as the numerical simulations in SPH are in 2D, it would be beneficial that the weir dimensions in the width of the flume were as simple and uniform as possible. This makes the 2D numerical model more realistic and makes the comparison between the numerical and experimental results straightforward; this also holds for the theoretical values obtained from Equation 2.17.

In the future, it would be interesting to conduct flume experiments with a submerged gate instead of a free flow gate, as these types of weir are practically always found in the field. For flume experiments with uniform flows without gate, velocity profiles at multiple locations can be measured, which can then be compared the velocity profiles found in the numerical model. Furthermore, by applying the least squares method to Equation 2.8 for measured velocity data within the turbulent wall shear layer, Equation 7.1 can be derived. This method is called the *Clauser method* [50]. With this equation the bed shear stress for the flume can be obtained and a correlation could possibly be established with the numerical value β .

$$\bar{u} = \frac{u_*}{\kappa} \ln y + \left(-\frac{u_*}{\kappa}\right) \ln y_0 = C_1 \ln y + C_2 \quad (7.1)$$

Regarding numerical research, until new turbulence models are added, it would be recommended to perform more numerical simulations with a wider range of parameters. For uniform flows, a specific combination of values α and β can be found for which there is agreement between a realistic turbulent velocity profile and water elevation over the flume, but this could be a time-intensive iterative process. For flume simulations with plastic fragments, it would be helpful to find a specific value of the restitution coefficient that gives the most realistic interactions between fragments. Furthermore, a wider variety of methods can be used to release fragments into the flume. For example, the distance between the released fragments can be altered, or the fragments can be released vertically instead of horizontally. A method to release a mix of fragments randomly is still unavailable. Lastly, SPH offers several options in terms of wave generation. Regular and irregular wave

can be generated at the inlet boundary. It could be interesting to see the effects of an incoming wave on the fragment-fragment interactions and passing ratios near the gate.

Until computational power increases, it is advised for a flume model with a numerical resolution sharp enough to model meso plastic debris to simulate in a 2D environment instead of a 3D one. In a 2D environment, more complex geometries than simple spheres, squares or triangles aren't possible for the size of the fragments used in this thesis. The modeling of micro plastics is not optional at the moment. Furthermore, it would be advised to limit the flume lengths to around 10 meters, the water depth around 0.1 to 0.2 meters, and the simulation time to be on the order of a minute.

If computational power sufficiently increases, 3D modeling would be more appealing. For the buoyancy tests, it would be interesting to compare the rising velocities between 3D fragments and 2D fragments. For the flume tests, the horizontal velocity profile at the surface can be examined, including its effects on the carpet shape. Furthermore, it can be examined if the vortex areas shown in [Figure 5.17](#) can also be represented in the numerical model.

Lastly, this report concluded that the Lagrangian based numerical methods SPH and DEM could be interesting alternatives to Eulerian based traditional CFD methods, when investigating the accumulation of plastic debris. The question remains in which situations or circumstances SPH-DEM is the better numerical option than CFD (or the other way around). For the representation of plastic debris, it would be recommended to always use a Lagrangian based numerical model like SPH or DEM if one would like to investigate the individual interactions between these debris, as these interactions are for example crucial in the accumulation process showed in this report. If one would like to investigate other processes that aren't dependent on individual interactions between debris (f.e. spatial distribution in a multi-phase flow with no structure interaction), CFD is recommended. For the representation of the flow, the choice between numerical methods depends on the complexity of the channel shape in coherence with the possible presence of hydraulic structures, free-surface variance and the manner in which turbulence needs to be properly represented in the flow. If the shape of the flow channel is straightforward and no or simple hydraulic structures are present, CFD is recommended, as a mesh is easily created. However if the shape of the channel and present hydraulic structures become more complex, SPH can be recommended, as they treat 'fragment-fluid-structure' interactions and accompanied free-surface variance more naturally. Lastly, if turbulence is an integral part within the investigation, CFD is recommended, as at the moment SPH is limited in the representation of turbulence in a flow.

A

ADDITIONAL LITERATURE

A.1. TURBULENCE MODELS

To simulate water flows with turbulent features as described in [Section 2.1](#) there are roughly three turbulence numerical models available in traditional CFD models, namely:

- In **Direct Numerical Modeling (DNS)** fluctuated values are directly implicated in the Navier-Stokes equations ([Equation 2.3](#)), without decomposing the flow into mean and fluctuating quantities and without using additional turbulence models. As in this case, the length scales of the discretized numerical grid should represent the Kolmogorov microscales ($\eta = (\nu^3/\epsilon)^{\frac{1}{4}}$) and an enormous number of grid points are needed. This makes this method practically impossible to use (even for barely turbulent flows) because it simply requires an impossible amount of computing power. z
- In a **Reynolds-Avaraged Navier Stokes (RANS)** model, the time-averaged values are implicated in the Navier-Stokes equation ([Equation 2.4](#)). The mean flow properties are smoothed over the flow, allowing a courser grid and less computational time. Additional arbitrary equations (Reynolds stresses) are added to approximate the effect of turbulence fluctuation of the flow. Simple one-equation models can be used, such as Spalart Amaras (SA), where a transport equation is solved for the turbulence quantity of the eddy viscosity ν_t related to the time scale. The length scale still has to be determined empirically, which is virtually impossible for complex flows. Two-equation models such as k- ϵ and k- ω can also be used, where two transport equations are solved for the turbulence quantities of the kinetic energy k and the dissipation rate of the kinetic energy ϵ or the specific dissipation rate of the kinetic energy ω related to the time and length scale. k- ϵ models are usually more used for free-stream problems and k- ω for near-wall problems. Even k- ϵ SST can be used, which uses k- ω near the wall and switches to k- ϵ in free flow. RANS models are the most standard used turbulence models.
- In a **Large Eddy Simulation (LES)** values are directly implicated in filtered Navier-Stokes equations for larger scale eddies and additional turbulence models are added for smaller scale eddies. One could say RNS is used for large scales and RANS for small scales, making LES a hybrid version of the two. One drawback of LES is that is has difficulty predicting near-wall regions, due to the small turbulence scales present there.

In contrast to CFD, the literature on turbulence modeling in SPH is quite scarce at present [\[51\]](#). Efforts have been made to directly solve Navier-Stokes equations in a Langrarian formulation for high turbulence flows. This DNS approach in SPH gives the same problems as in CFD. As it is practically impossible to solve for all length scales. Furthermore, the theoretical foundation of this method is lacking [\[52\]](#). Regarding turbulence models, there are some studies in which traditional CFD turbulence models are reproduced in SPH, such as one-equation models [\[53\]](#), k- ϵ models [\[54\]](#) and Large Eddy Simulation (LES) Issa *et al.* [\[55\]](#). Where LES seems to be the easier to apply than RANS models, as LES only models the small scale eddies, making it less dependent on boundaries conditions and the modeling easier [\[52\]](#).

A.2. TECHNICAL REQUIREMENTS NUMERICAL METHOD

There are four requirements that the proposed numerical method must meet. It has to be noted, that at the time these requirements were drawn up, the goal was to simulate a plastic debris accumulation in front of a rack in stead of the later used sluice gate. Furthermore, the focus also included the need to simulate a proper backwater rise in front of the rack (second requirement), this focus was later let go to keep the scope of the project sizable.

1. The first requirement for the numerical method is to properly reproduce the blockage of the rack by the gate- and carpet formation in front of it. Therefor it's required that the plastic debris be modeled as individual particles. As when the plastic particles are instead modeled as continuum, which is for example done for sediment particles in most multi-phase flows, the plastic continuum will just flow trough the rack without any blocking. Note that this requirement only applies to accumulation-focused models. If one purely wanted to examine plastic behavior instead, continuum-based models can be used.
2. The second requirement for the numerical method is to properly reproduce the backwater rise in front of the rack. Therefor it's required that in the model the dynamics between the entities of water and plastic are numerically two-way coupled (Figure A.1b). Two-way coupling means that in this case in the numerical model the water flow affects the plastic particles and in turn the plastic particles affect the water flow. This is contrary to (Figure A.1a) one-way coupling, where the water flow affects the plastic particles; however, plastic particles do not affect the water flow.

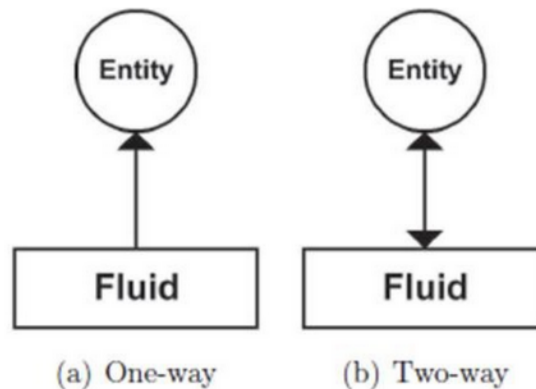


Figure A.1: Basic coupling approaches for numerical modeling

Therefore, when one would only like to examine the influence of flow characteristics and/or turbulence on a particles or multiple particles, a one-way approach would suffice, as one would only be interested in how the particles are affected by the water flow. However if a water-level rise caused by particle accumulation is wished to be replicated, a two-way approach is needed, as it is required that the plastic particles blocking the rack, affect the water flow and therefor create a back-water rise.

3. The third requirement for the numerical method is that the rack structure can be truly set up in 3D. This is necessary as the mesh of the rack is naturally made up of horizontal and vertical bars. And when the set-up was 2D modeled, it would always mean that one of the two bar dimensions could not be modeled. Since the length dimension in front of the rack would always be preferred to be included, as otherwise carpet formation and back-water rise could not be simulated.
4. The last requirement for the numerical method is that it is user-friendly. This is assessed in the context of available external support (which weighs heaviest), software usability and computational demand.

A.3. NUMERICAL METHODS ASSESSMENT

The assessment of different numerical methods is comparable to a tiny jigsaw puzzle. First, the general numerical methods, which can be seen as puzzle pieces, are described in the way that they represent water and/or plastic. Then combinations of these puzzle pieces are made and assessed, which is the numerical coupling of these methods. These assessments are based on the technical requirements mentioned above.

A.3.1. INVENTORY GENERAL NUMERICAL METHODS

- **Computational Fluid Dynamics (CFD)** is a Eulerian mesh-based numerical method that can model the dynamics of fluid- and multiphase flows. A mesh is created by dividing a continuum flow domain into several discrete subdomains. Physical information is stored at the nodes of the created grid. Regularly used CFD software is the open-source free **OpenFoam (OF)** [56] and the commercially developed **ANSYS Fluent (AS)** [57], which is freely accessible (for 2D problems) with the TU license. In general both OF and AS can be used for different problems given roughly the same results. For example for both softwares standard RANS turbulence models like $k-\epsilon$ models can be applied resulting roughly in the same results [58].
An advantage of OF is the high degree of freedom and adjustability within the software due to the open source nature. For example, there are no limitations on programming within OF and/or black boxes are present. However this advantage is also a disadvantage, as for less experienced users this set-up can be quite overwhelming. Whereas AF seems more user-friendly (f.e. multiple user-defined functions) for users who are just getting familiar with numerical modeling. This premise was confirmed by talks with people with 'hands-on' experience (Pengxu, Jeremy Bricker).
- **Smoothed-Particle Hydrodynamics (SPH)** is a Lagrangian mesh-free numerical method that can model the dynamics of fluids and particles. Originally introduced to simulate astronomical problems by Gingold and Monaghan [20]. A continuum domain is not modeled with a grid, but by a set of arbitrary distributed nodal points. Every nodal point has its set of physical properties assigned (e.g., mass, density, velocity, position, pressure). At these points the discretised Navier–Stokes equations are integrated at every time step based on neighbouring particles, which updates the local properties and therefore the movement of these particles. The determination of which particles are considered neighboring is based on a weighted kernel function (W), which is based on the smoothing length h . Which is circular for 2D situations and spherical for 3D situations.
One of the disadvantages of SPH models is that they can have a high computational cost. Due to the presence of small time steps to require to the Courant condition and the high number of particles. To address this fact, Graphic Processing Units (GPUs) have been implemented in recent years to reduce computing time [59]. This resulted in the development of a new open-source dualSPHysics software [60], which is also the most used commercially available software.
- **Particle Finite Element Method (PFEM)** is a Lagrangian mesh-based numerical method that can model the hydrodynamics of fluid and multiphase flows. A mesh is created, but due constant remeshing, the nodes on the grid move in a Lagrangian manner through the simulation [61]. Therefore this method can be seen as a kind of compromise between the mesh-based CFD and meshless SPH. The research done with this method has been steadily growing in recent years [62], however, it is still the most infant of the above-mentioned methods and therefore more difficult in usability. As little external support is available and certain features such as two-way coupling are still missing [63]. That's why this method is not taking in to account for the numerical assessment.
- **Discrete Element Method (DEM)** is a Lagrangian numerical method that can model the dynamics of discrete particles. Originally introduced to simulate behaviour of granular assemblies by Cundall and Strack [41]. Today bulk materials, rocks, powders and pharmaceuticals are also commonly simulated in DEM. Non-spherical particles can also be employed. DEM uses contact detection and contact forces between particles to determine the movement of these particles. The software regularly used for DEM is ROCKY [64].

A.3.2. ASSESSMENT COUPLED NUMERICAL METHODS

- **CFD-CFD** is a two-way coupled approach used to simulate multi-phase flows where the fluid and the debris are both modeled as a continuum. Meaning that no individual plastic particles are traced and particle properties like shape and size only are not directly simulated, they are only indirectly represented in the density and volume of the entire particle-fluid. This means that simulating plastic accumulation against a rack would not be possible, as the particles would flow between the bars, not meeting the proposed requirements. It seems that CFD-CFD is more interesting if one wanted to investigate the behavior of the plastic particles without structure interaction. An other problem with CFD-CFD is that the free-surface is not naturally defined and more complicated methods like VoF models are needed for compensation [17]. This becomes even a more complicated problem when floating objects are added interacting with the free-surface. As stated in the inventory, software such as OpenFoam and ANSYS FLuent is freely available and offers relatively good support options.
- **CFD-DEM** is a one-way or two-way coupled approach which simulates the fluid as a continuum and the debris as discrete elements, so it already meets two of the technical requirements. Self proclaimed open-source software like the CFDEM@project are freely available [65], which has been used to research the effects of debris landslide in a water reservoir [66]. However it seems that available support is lacking and some features like using non-spherical particles are not publicly available. So Ansys-EDEM is still the most used software, which uses traditional ANSYS Fluent for the fluid simulation coupled to the DEM-based Rocky [64]- or EDEM Software for the particle simulation. This software has been used, among others, to simulate the blocking (two-way coupled) of a river by a landslide [67]. However, the problem with Ansys is that with the current TU license, 3D simulations are not possible and therefore it does not meet one of the proposed technical requirements.
- **SPH-SPH** is a two-way coupled approach that simulates fluids and debris as discrete particles and elements. As they are both formulated in roughly the same matter the treatment of free motions of a body inside a fluid is quite easy. The first simulations of floating bodies in fluid were performed by Bouscasse *et al.* [68]. Recent examples of research are simulations of floating bodies in a none-linear waves in 2D [69] and 3D [70], as well as simulations of floating booms in a two-phase flow (oil and water) [71]. The fluid-structure interface is easily defined due to the Langrangian nature of the model, which in turn makes interactions between fluid and structures easier [72]. The problem with the SPH-SPH approach is that there is no user-friendly software available, as every university uses its own written codes, making general support hard.
- **SPH-(DC)DEM** is a two-way coupled approach which simulates the fluid and debris as discrete particles and elements. This coupled method seems to have gained a lot of traction in the environmental flow sciences recently [21]. Canelas *et al.* [22] introduced a method which unified the discretization of SPH and DEM in the DualSPHysics software framework. He also validated his method [23], by reproducing an experimental research of Zhang *et al.* [24] concerning dam-breaks. Furthermore, Canelas *et al.* [25] conducted a study in which he simulated a stony particle flow flowing in water through a small-scale slit check dam. This is an interesting set-up as it is of course quite similar to the set-up proposed in this research. Furthermore, external support for the use of SPH-(DC)DEM should suffice as C. Altomare, a core developer of the DualSPHysics numerical model, has expressed his willingness to help from abroad.

In conclusion, according to the summarized version of the assessment in table A.1 the SPH-(DC)DEM numerical method appears to be the best possible option to simulate plastic debris accumulations in front of a rack. Since it meets the most of the requirements proposed in Section A.2.

	CFD-CFD	CFD-DEM	SPH-SPH	SPH-DEM
Individual particles	x	✓	✓	✓
Two-way coupling	✓	✓	✓	✓
Three-dimensional	✓	x	✓	✓
Usability	✓	✓	x	✓

Table A.1: Summary assessment of coupled numerical methods

B

EXPERIMENTAL RESEARCH DATA

B.1. BUOYANCY EXPERIMENTS

Fragment	Time #1	Time #2	Time #3	Time #4	Time #5	Rising velocity
Red #1	1.29 s	1.04 s	0.98 s	1.18 s	0.92 s	0.185 m/s
Red #2	1.14 s	0.87 s	0.80 s	0.81 s	0.81 s	0.226 m/s
Yellow	1.18 s	1.37 s	1.51 s	1.30 s	1.44 s	0.147 m/s
Blue	2.02 s	2.24 s	2.01 s	2.05 s	1.92 s	0.098 m/s
Green	6.01 s	5.50 s	4.12 s	3.66 s	3.67 s	0.044 m/s

Table B.1: Rising velocities time measurements per fragment type

B.2. FLUME EXPERIMENTS

Progress Date	Condition (Gate Opening, Flow rate)	No Particle	Red (400 particles)	Yellow (400 particles)	Green (400 particles)	Blue (400 particles)	Mix (100 per particle, Total 400 particles)
18 th January 2022	5 cm, 10 l/s Without Release Gate	1 time	3 times	3 times	3 times	3 times	3 times
	5 cm, 10 l/s With Release Gate		1 time	1 time	1 time	1 time	1 time
8 th February 2022	4.5 cm, 10 l/s	1 time	5 times	5 times	5 times	5 times	6 times
	5.3 cm, 10 l/s	1 time	5 times	5 times	5 times	5 times	6 times
1 st March 2022	5 cm, 12.5 l/s	1 time	5 times	5 times	5 times	5 times	5 times
	5 cm, 8.28 l/s	1 time	5 times	5 times	5 times	5 times	5 times
	5 cm, 11 l/s	1 time	-	-	5 times	-	-
22 th March 2022	5 cm, 11 l/s	-	5 times	5 times	-	5 times	5 times
Total							152 times

Table B.2: Overview all flume experiments executed

NO GATE EXPERIMENTS

x (m)	y (mm)
0.15	87.4
1	84.1
2	81.4
3	78.5
4	78.7
5	79.1
6	79.9
7	76.1
8	72.3
9	67.8
10	64.0
11	57.6
12	55.5
12.5	47.3

Table B.3: Water elevation measurements

x (m)	y (mm)
0.15	76.1
1	74.3
2	73.7
3	70.6
4	70.6
5	69.5
6	69.8
7	67.2
8	64.3
9	59.6
10	57.8
11	53.3
12	48.0
12.5	41.5

Table B.4: Water elevation measurements

x (m)	y (mm)
0.15	131.0
1	131.8
2	130.7
3	127.8
4	127.8
5	126.9
6	124.6
7	121.4
8	116.0
9	110.7
10	106.8
11	101.9
12	88.5
12.5	78.3

Table B.5: Water elevation measurements

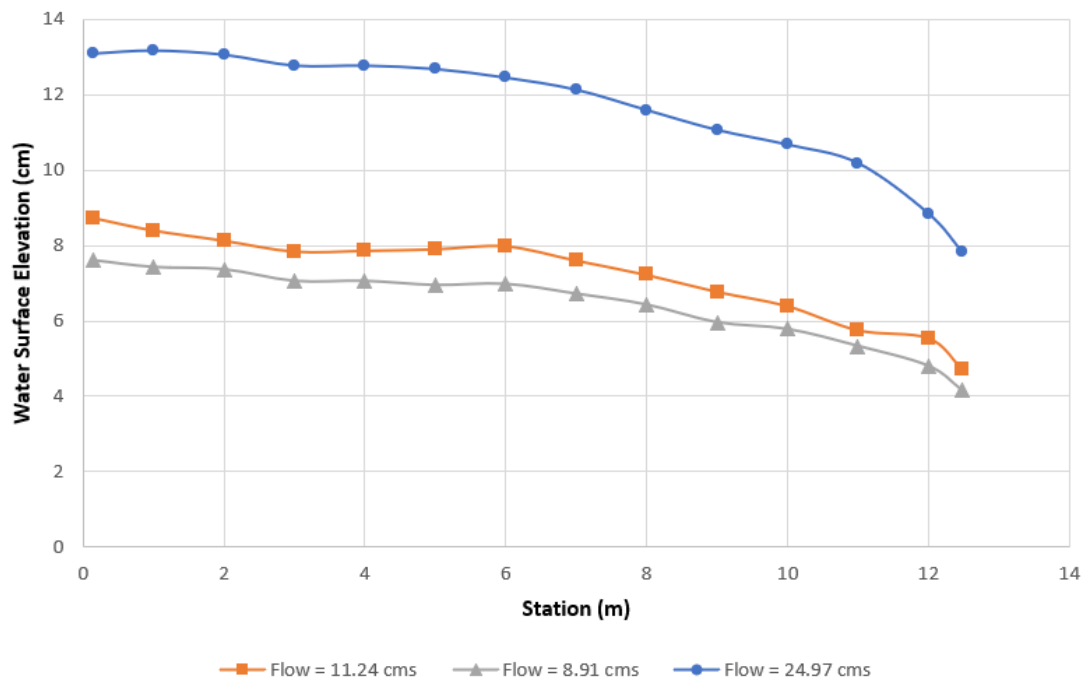


Figure B.1: Water elevation measurements over flume length for different flow rates

GATE EXPERIMENTS

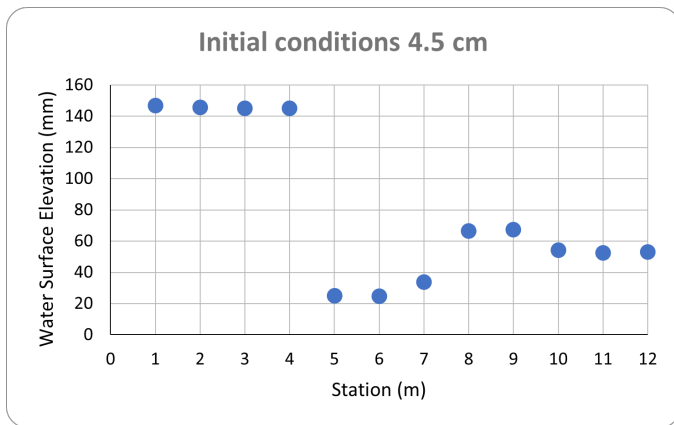


Figure B.2: Water elevation measurements over flume length
Initial conditions 4.5 cm

x (m)	y (mm)
1	146.7
2	145.5
3	145.0
4	145.0
5	25.0
6	24.6
7	33.7
8	66.4
9	67.3
10	54.1
11	52.5
12	52.9

Table B.6: Water elevation measurements

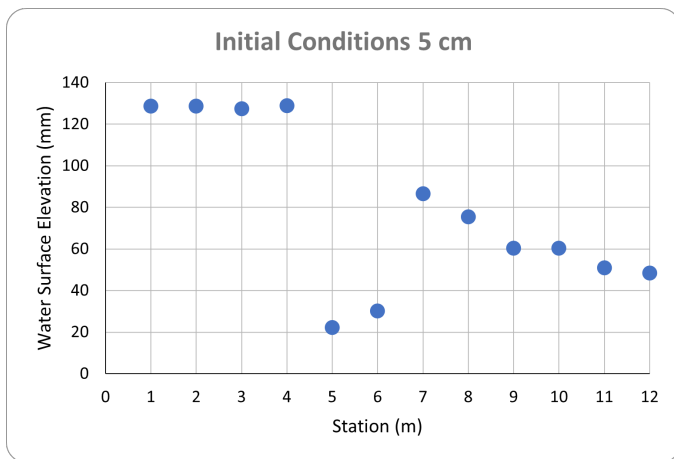


Figure B.3: Water elevation measurements over flume length
Initial conditions 5.0 cm

x (m)	y (mm)
1	128.6
2	128.6
3	127.4
4	128.8
5	22.3
6	30.1
7	86.6
8	75.5
9	60.4
10	60.3
11	51.0
12	48.4

Table B.7: Water elevation measurements

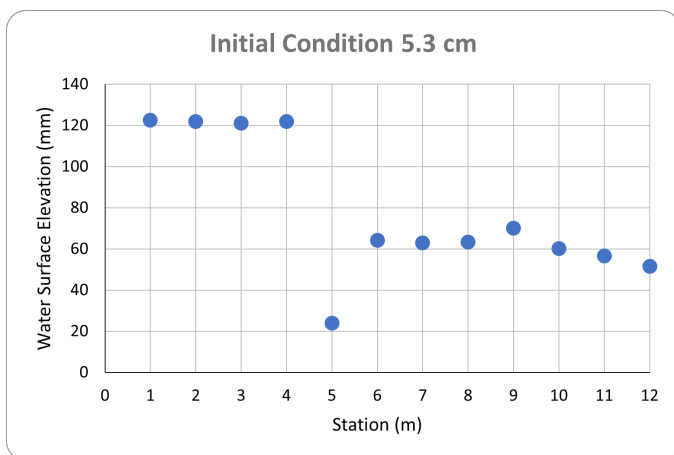


Figure B.4: Water elevation measurements over flume length
Initial conditions 5.3 cm

x (m)	y (mm)
1	122.5
2	121.8
3	121.0
4	121.8
5	24.0
6	64.2
7	62.8
8	63.4
9	70.0
10	60.2
11	56.6
12	51.6

Table B.8: Water elevation measurements

PASSING RATIOS AND CARPET LENGTHS

Gate opening	Red	Yellow	Blue	Green
45 mm	0%	0.5%	52%	100 %
50 mm	0%	2.5 %	92%	100 %
53 mm	1 %	2 %	99%	100 %

Table B.9: Pass ratios results by item per configuration from experimental data

Gate opening	Red	Yellow	Blue	Green
45 mm	49.6 cm	13.2 cm	8.4 cm	0 cm
50 mm	48.7 cm	15.3 cm	7.8 cm	0 cm
53 mm	43.6 cm	8.8 cm	2.4 cm	0 cm

Table B.10: Carpet length results by item per configuration from experimental data

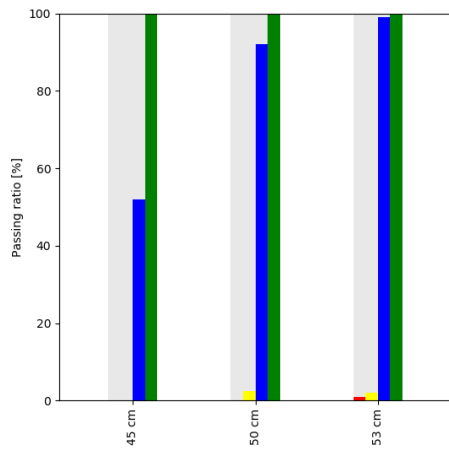


Figure B.5: Bar chart of passing ratio's for all fragments per gate configuration obtained from experimental research

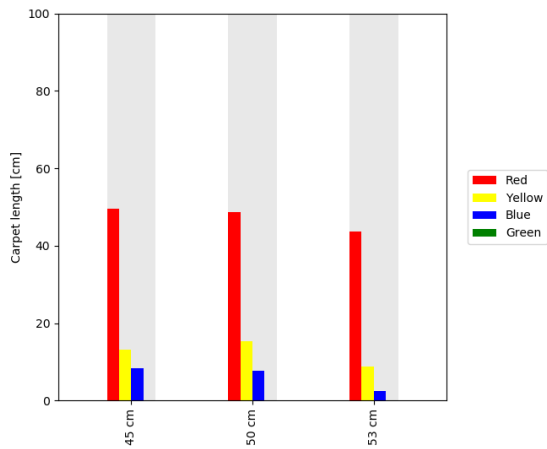


Figure B.6: Bar chart of carpet lengths for all fragments per gate configuration obtained from experimental research

C

NUMERICAL DESIGN INPUT

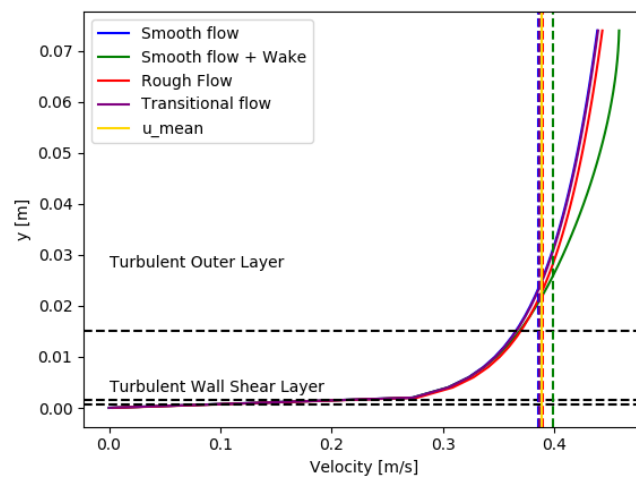


Figure C.1: Velocity profile low; $d = 0.076$ m; $u = 0.39$ m/s; $k_s = 0.00016$; $S = 0.00072$

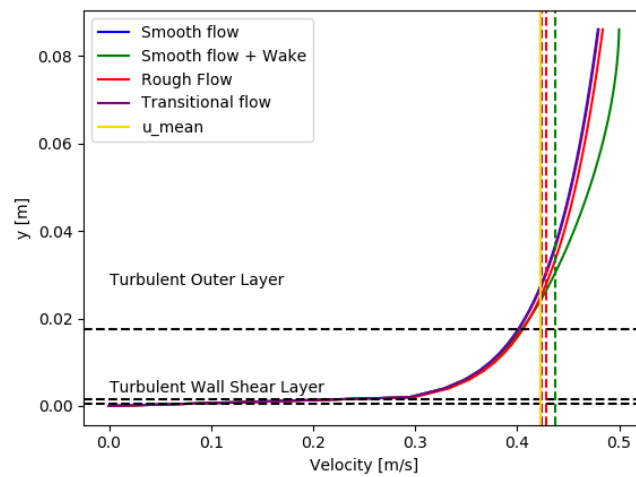


Figure C.2: Velocity profile medium; $d = 0.088$ m; $u = 0.42$ m/s; $k_s = 0.00015$; $S = 0.00075$

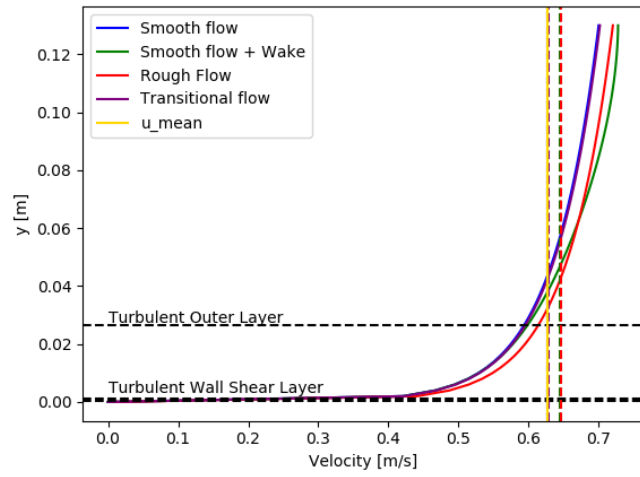


Figure C.3: Velocity profile high; $d = 0.132$ m; $u = 0.63$ m/s; $k_s = 0.00009$; $S = 0.0011$

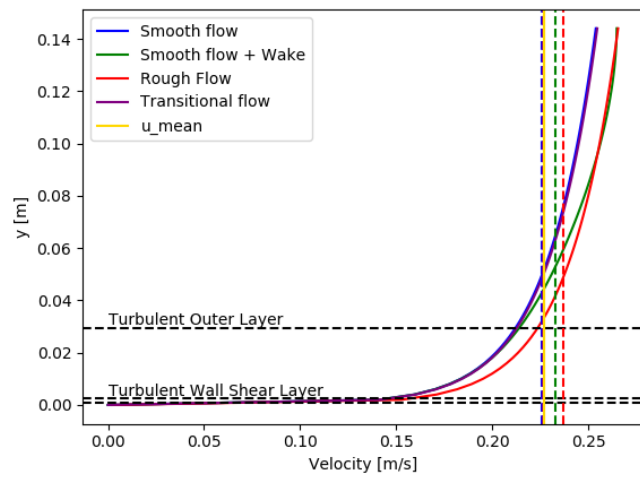


Figure C.4: Velocity profile 4.5 cm; $d = 0.146$ m; $u = 0.23$ m/s; $k_s = 0.0002$; $S = 0.00016$

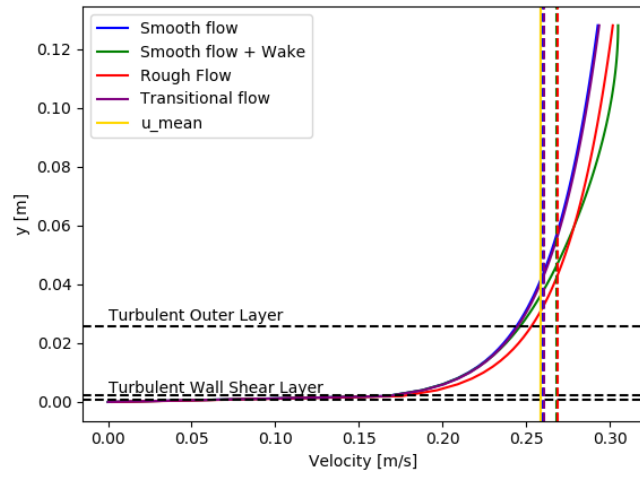


Figure C.5: Velocity profile 5.0 cm; $d = 0.128$ m; $u = 0.26$ m/s; $k_s = 0.0002$; $S = 0.00023$

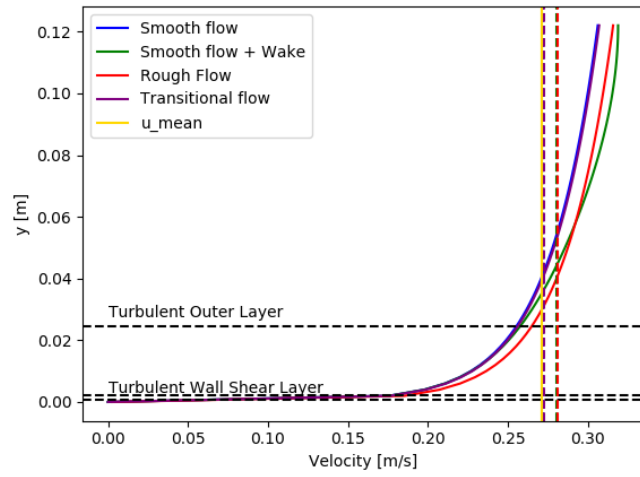


Figure C.6: Velocity profile 5.3 cm; $d = 0.122$ m; $u = 0.27$ m/s; $k_s = 0.00019$; $S = 0.00026$

D

SUPPLEMENTARY NUMERICAL RESULTS

D.1. RED FRAGMENTS

4.5 CM GATE OPENING

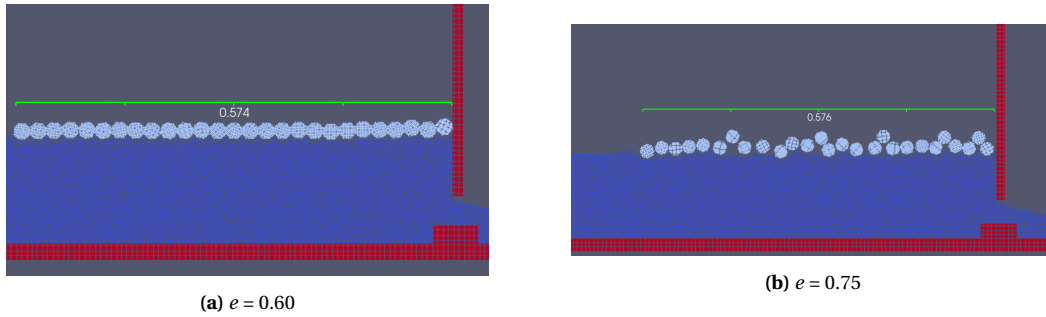


Figure D.1: Final carpet situation for red fragments with ρ_{num} for a 4.5 cm gate opening configuration

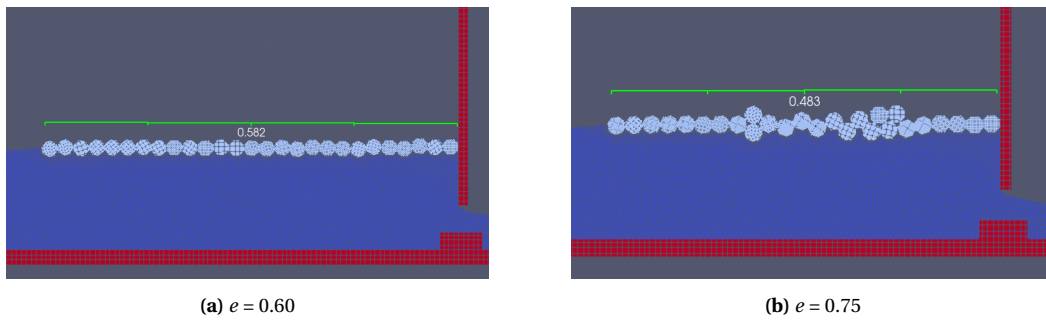


Figure D.2: Final carpet situation for red fragments with ρ_{exp} for a 4.5 cm gate opening configuration

5.0 CM GATE OPENING

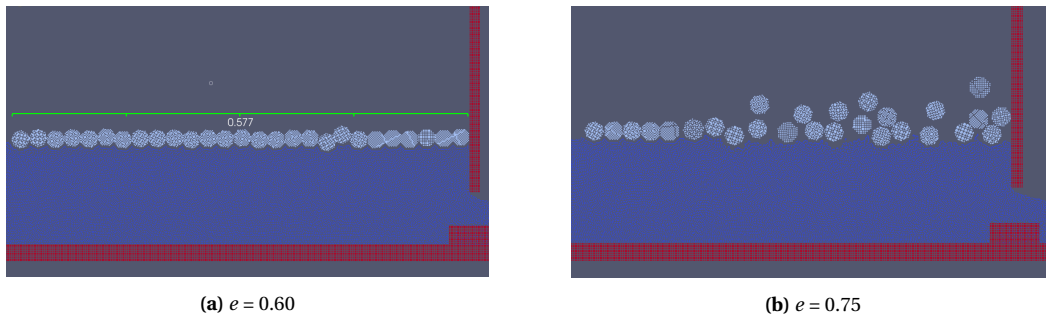


Figure D.3: Final carpet situation for red fragments with ρ_{num} for a 5.0 cm gate opening configuration

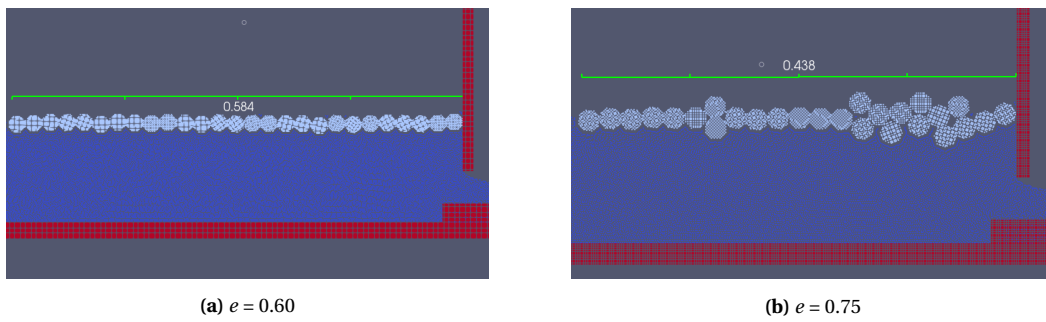


Figure D.4: Final carpet situation for red fragments with ρ_{exp} for a 5.0 cm gate opening configuration

5.3 CM GATE OPENING

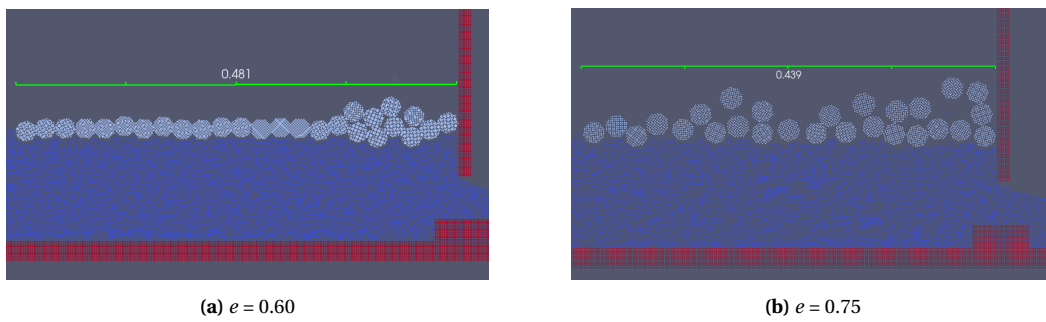


Figure D.5: Final carpet situation for red fragments with ρ_{num} for a 5.3 cm gate opening configuration

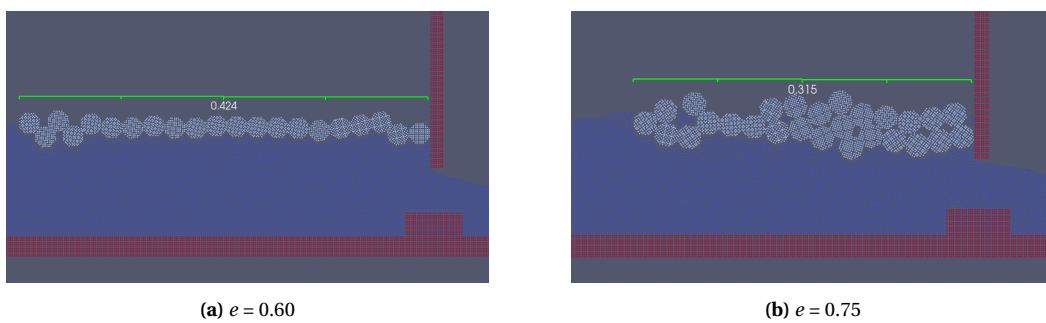
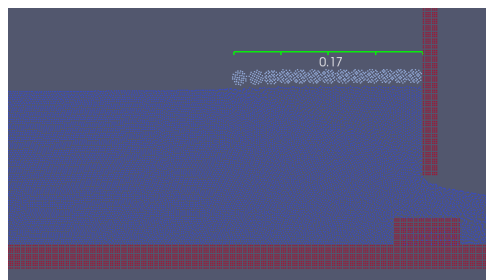


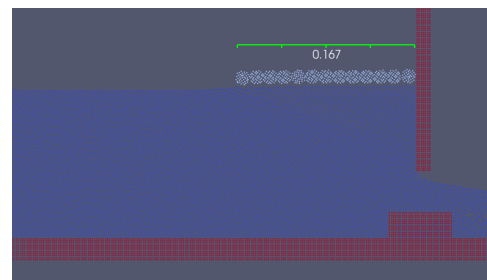
Figure D.6: Final carpet situation for red fragments with ρ_{exp} for a 5.3 cm gate opening configuration

D.2. YELLOW FRAGMENTS

4.5 CM GATE OPENING

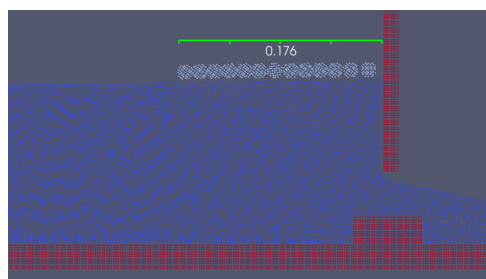


(a) $e = 0.60$



(b) $e = 0.75$

Figure D.7: Final carpet situation for yellow fragments $\rho_{numerical}$



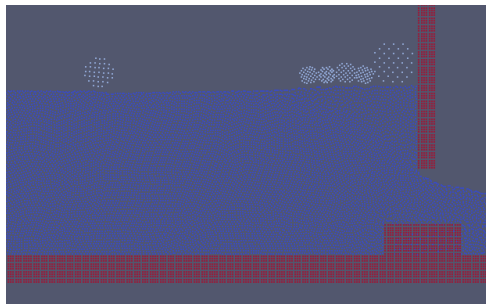
(a) $e = 0.60$



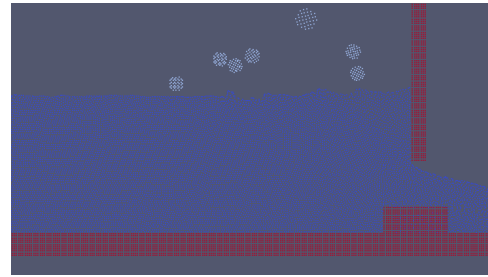
(b) $e = 0.75$

Figure D.8: Final carpet situation for yellow fragments with $\rho_{experimental}$

5.0 CM GATE OPENING

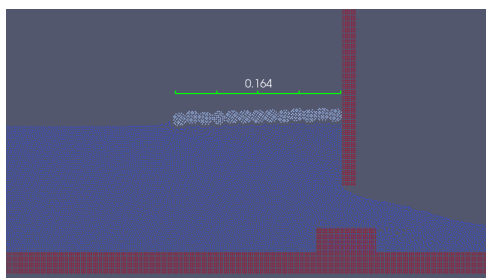


(a) $e = 0.60$

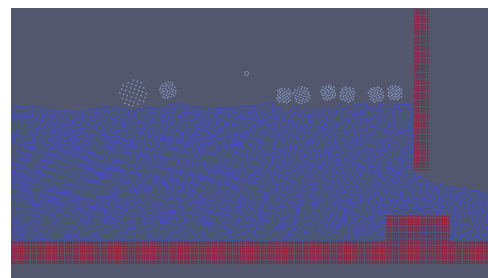


(b) $e = 0.75$

Figure D.9: Final carpet situation for yellow fragments $\rho_{numerical}$



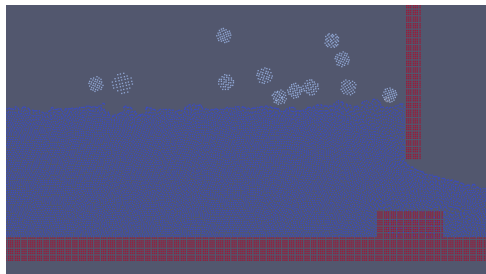
(a) $e = 0.60$



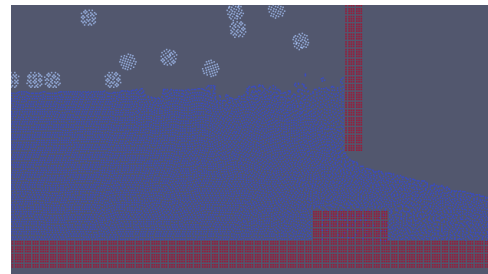
(b) $e = 0.75$

Figure D.10: Final carpet situation for yellow fragments with $\rho_{experimental}$

5.3 CM GATE OPENING

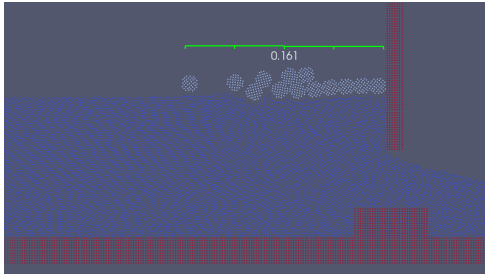


(a) $e = 0.60$

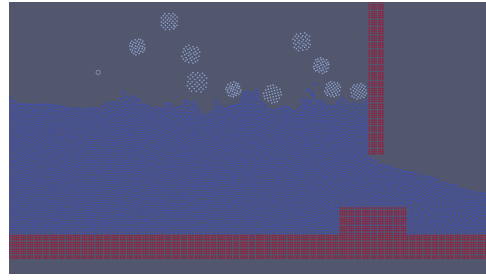


(b) $e = 0.75$

Figure D.11: Final carpet situation for yellow fragments $\rho_{numerical}$



(a) $e = 0.60$

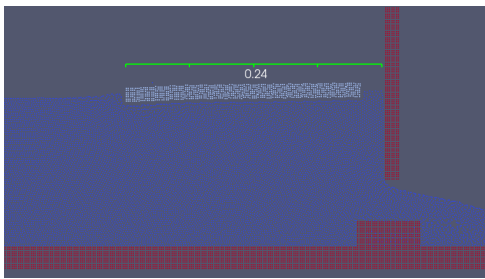


(b) $e = 0.75$

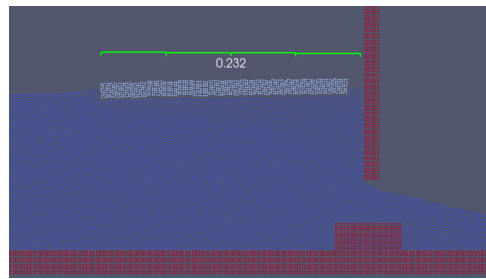
Figure D.12: Final carpet situation for yellow fragments with $\rho_{experimental}$

D.3. BLUE FRAGMENTS

4.5 CM GATE OPENING

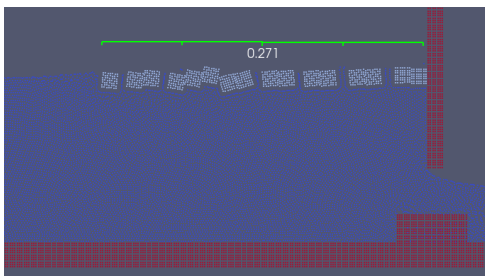


(a) $e = 0.60$

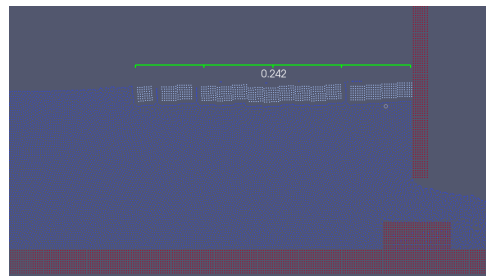


(b) $e = 0.75$

Figure D.13: Final carpet situation for blue fragments ρ_{num}



(a) $e = 0.60$



(b) $e = 0.75$

Figure D.14: Final carpet situation for blue fragments with ρ_{exp}

5.0 CM GATE OPENING

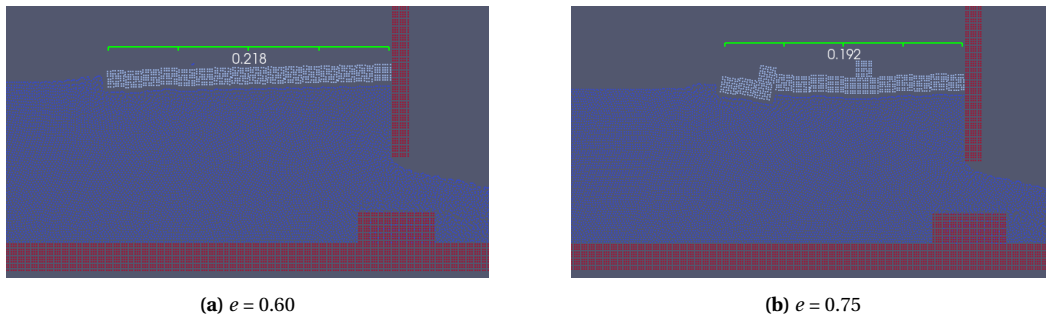


Figure D.15: Final carpet situation for blue fragments ρ_{num}

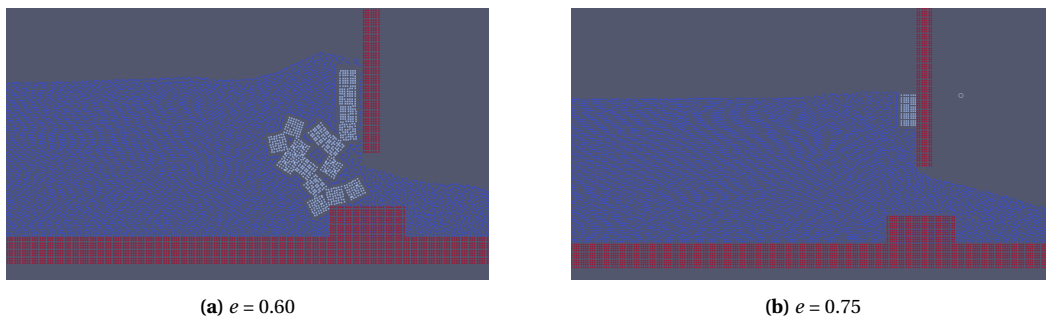


Figure D.16: Final carpet situation for blue fragments with ρ_{exp}

5.3 CM GATE OPENING

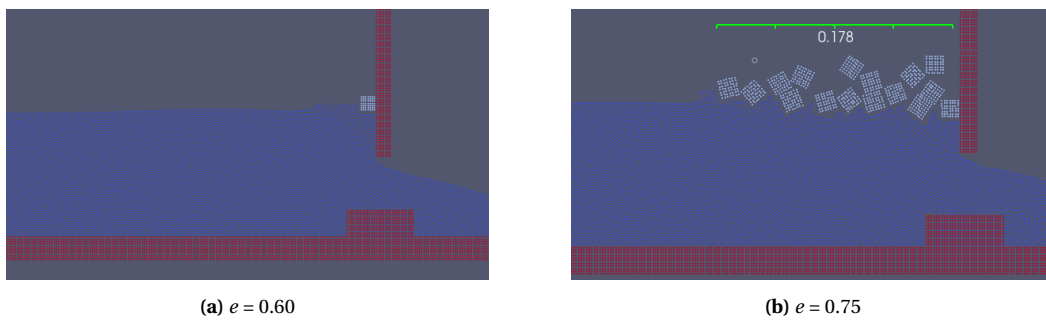


Figure D.17: Final carpet situation for blue fragments ρ_{num}

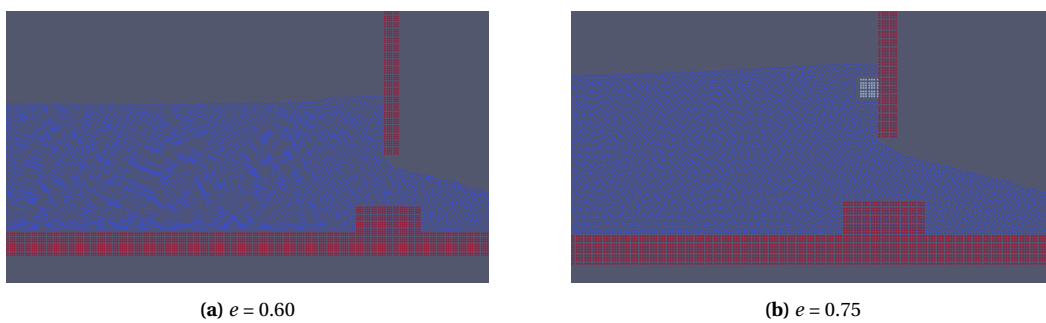
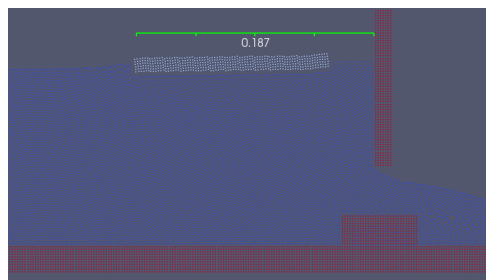


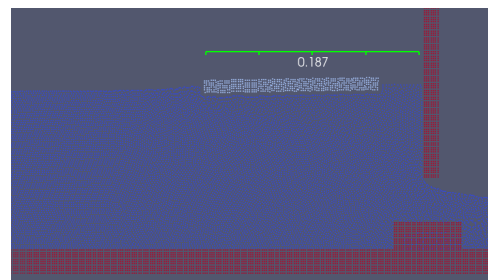
Figure D.18: Final carpet situation for blue fragments with ρ_{exp}

D.4. GREEN FRAGMENTS

4.5 CM GATE OPENING

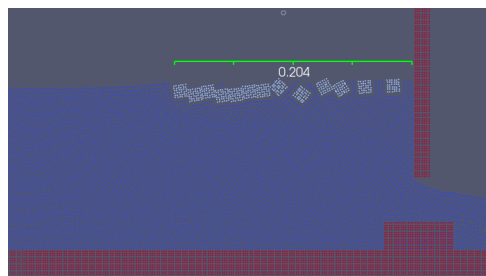


(a) $e = 0.60$

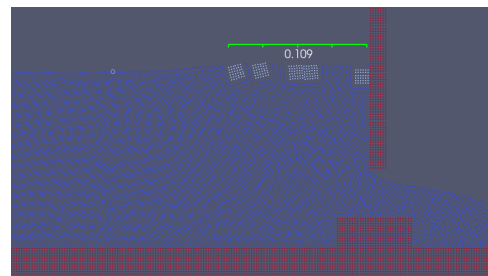


(b) $e = 0.75$

Figure D.19: Final carpet situation for green fragments ρ_{num}



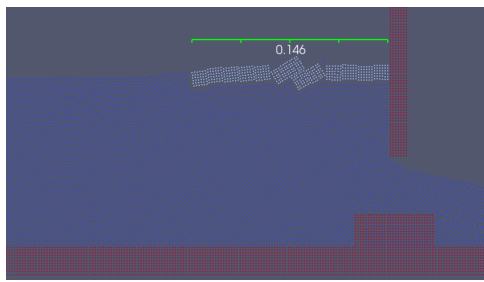
(a) $e = 0.60$



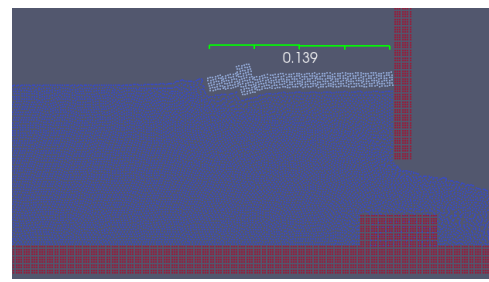
(b) $e = 0.75$

Figure D.20: Final carpet situation for green fragments with ρ_{exp}

5.0 CM GATE OPENING

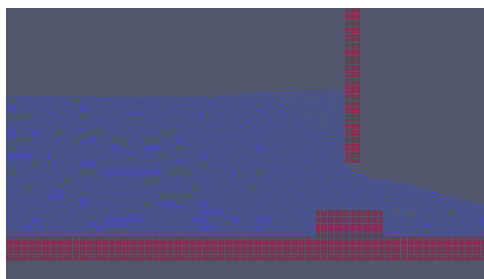


(a) $e = 0.60$

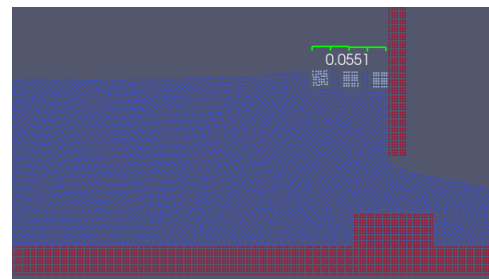


(b) $e = 0.75$

Figure D.21: Final carpet situation for green fragments ρ_{num}



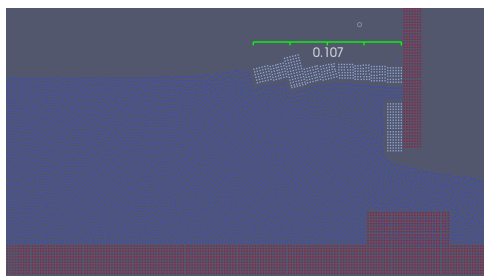
(a) $e = 0.60$



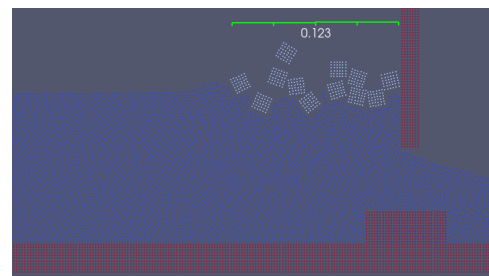
(b) $e = 0.75$

Figure D.22: Final carpet situation for green fragments with ρ_{exp}

5.3 CM GATE OPENING

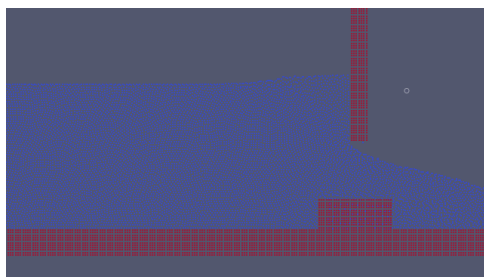


(a) $e = 0.60$

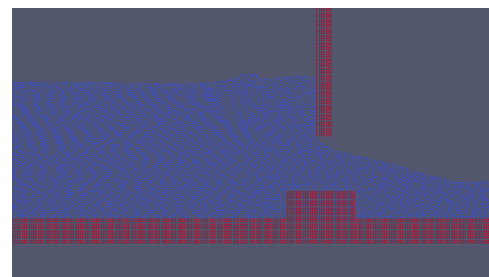


(b) $e = 0.75$

Figure D.23: Final carpet situation for green fragments ρ_{num}



(a) $e = 0.60$



(b) $e = 0.75$

Figure D.24: Final carpet situation for green fragments with ρ_{exp}

D.5. ANOMALIES REGARDING DENSITY

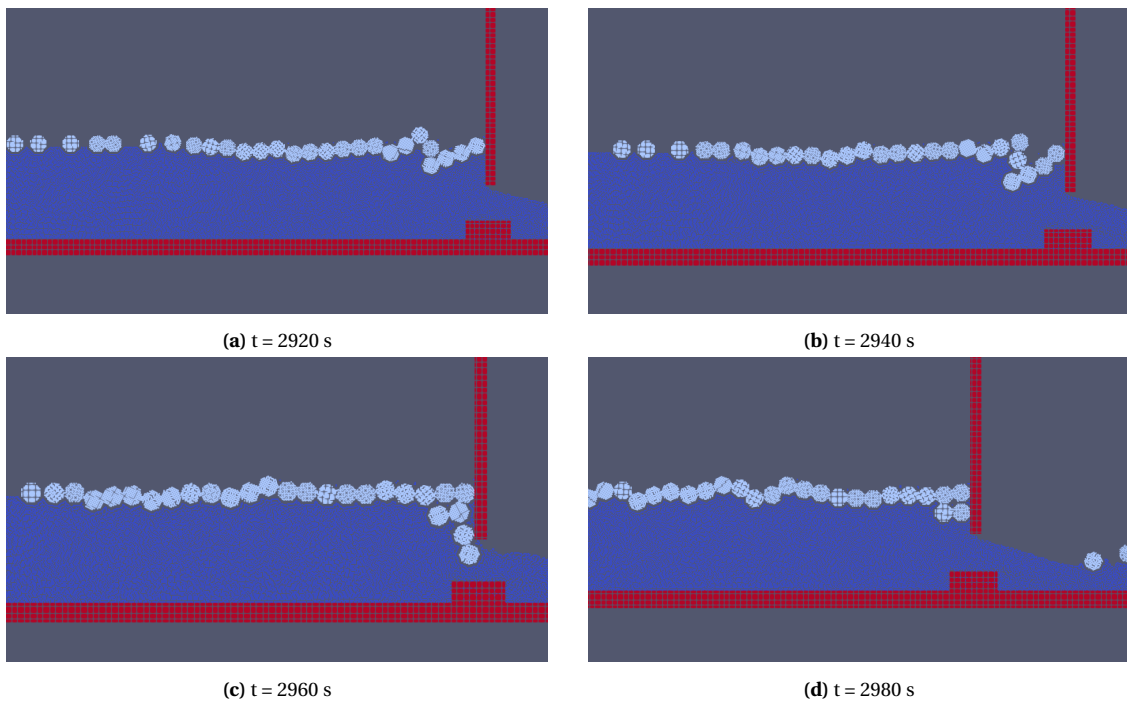


Figure D.25: Anomaly Scenario 3 red fragments with gate opening height of 5.3 cm

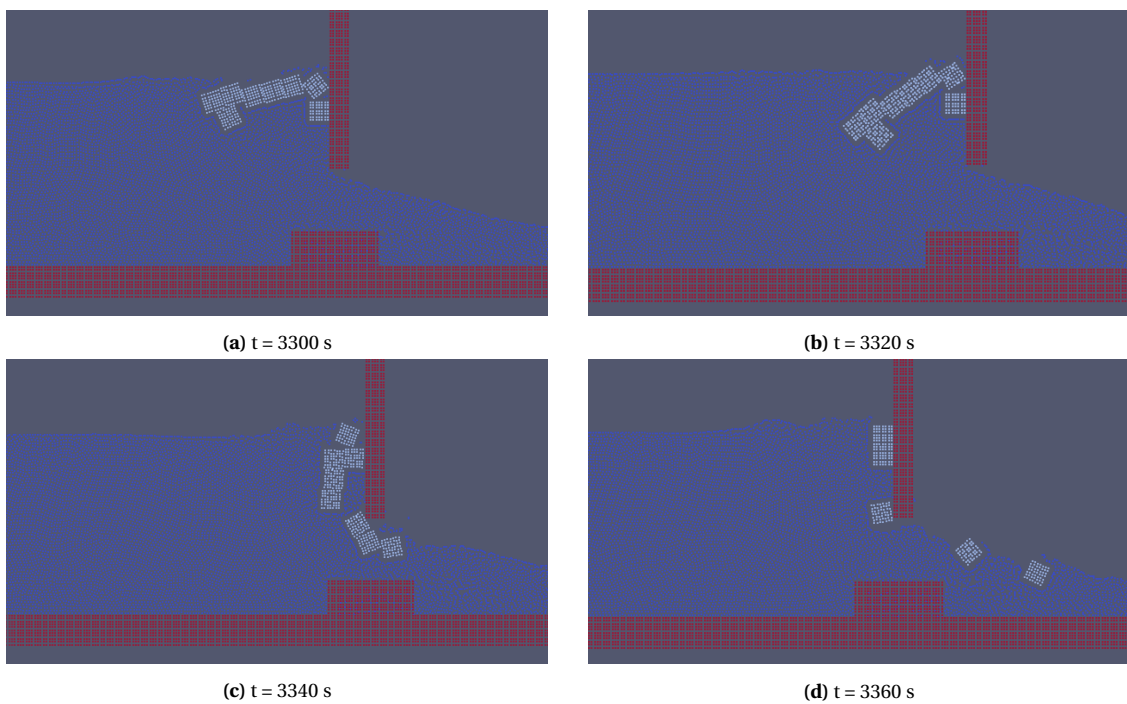
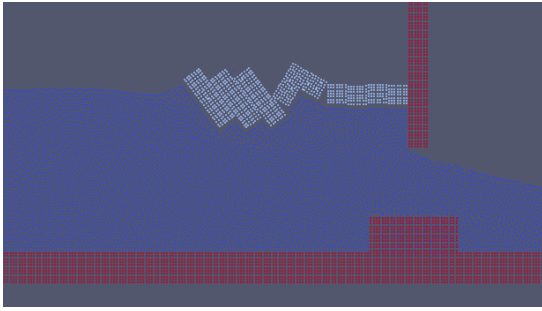
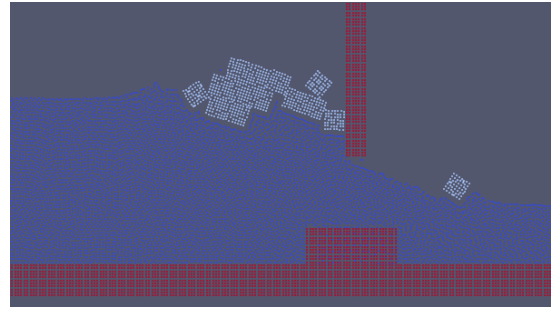


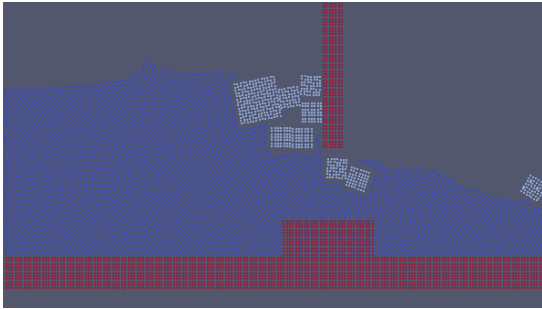
Figure D.26: Anomaly Scenario 4 blue fragments with gate opening height of 5.0 cm



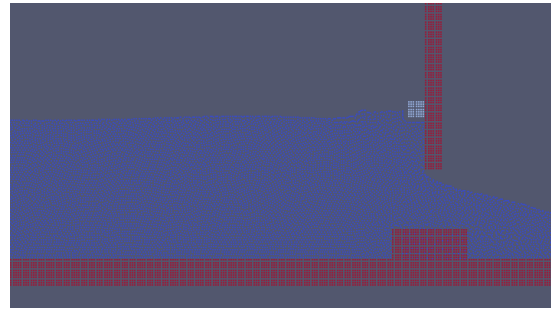
(a) $t = 3600$ s



(b) $t = 3700$ s



(c) $t = 3800$ s



(d) $t = 3900$ s

Figure D.27: Anomaly Scenario 1 blue fragments with gate opening height of 5.3 cm

BIBLIOGRAPHY

- [1] I. E. Napper and R. C. Thompson, *Plastic Debris in the Marine Environment: History and Future Challenges*, *Global Challenges* **4**, 1900081 (2020).
- [2] J. R. Jambeck, R. Geyer, C. Wilcox, T. R. Siegler, M. Perryman, A. Andrady, R. Narayan, and K. L. Law, *Plastic waste inputs from land into the ocean*, *Science* **347**, 768 (2015).
- [3] T. van Emmerik and A. Schwarz, *Plastic debris in rivers*, *WIREs Water* **7** (2019), <https://dx.doi.org/10.1002/wat2.1398>.
- [4] S. C. Gall and R. C. Thompson, *The impact of debris on marine life*, *Marine Pollution Bulletin* **92**, 170 (2015).
- [5] M. A. Browne, T. Galloway, and R. Thompson, *Microplastic—an emerging contaminant of potential concern?* *Integrated Environmental Assessment and Management* **3**, 559 (2007).
- [6] L. G. A. Barboza, A. D. Vethaak, B. R. Lavorante, A.-K. Lundebye, and L. Guilhermino, *Marine microplastic debris: An emerging issue for food security, food safety and human health*, *Marine Pollution Bulletin* **133**, 336 (2018).
- [7] L. C. Lebreton, J. Van Der Zwet, J. W. Damsteeg, B. Slat, A. Andrady, and J. Reisser, *River plastic emissions to the world's oceans*, *Nature Communications* **8**, 1 (2017).
- [8] L. J. Meijer, T. van Emmerik, R. van der Ent, C. Schmidt, and L. Lebreton, *More than 1000 rivers account for 80% of global riverine plastic emissions into the ocean*, *Science Advances* **7**, eaaz5803 (2021).
- [9] Y. Hidayat, S. Kiranamahsa, and M. Zamal, *A study of plastic waste management effectiveness in indonesia industries*, *AIMS Energy* **7**, 350 (2019).
- [10] S. B. Kurniawan and M. F. Imron, *Seasonal variation of plastic debris accumulation in the estuary of Wonorejo River, Surabaya, Indonesia*, *Environmental Technology & Innovation* **16**, 100490 (2019).
- [11] M. R. Cordova and I. S. Nurhati, *Major sources and monthly variations in the release of land-derived marine debris from the Greater Jakarta area, Indonesia*, *Scientific Reports* **9**, 1 (2019).
- [12] C. T. Roebroek, S. Harrigan, T. H. Van Emmerik, C. Baugh, D. Eilander, C. Prudhomme, and F. Pappenberger, *Plastic in global rivers: Are floods making it worse?* *Environmental Research Letters* **16**, 25003 (2021).
- [13] *What's Clogging Jakarta's Waterways? You Name It - The New York Times*, .
- [14] D. Honigh, T. van Emmerik, W. Uijttewaal, H. Kardhana, O. Hoes, and N. van de Giesen, *Urban River Water Level Increase Through Plastic Waste Accumulation at a Rack Structure*, *Frontiers in Earth Science* **14** (2020), <https://dx.doi.org/10.3389/feart.2020.00028>.
- [15] L. Zaat, *Below the surface: A laboratorial research to the vertical distribution of buoyant plastics in rivers*, (2020).
- [16] D. Schouten, *Simulation of the interception of plastic fluxes in rivers*, (2021).
- [17] E. Guerrero, F. Muñoz, and N. Ratkovich, *Comparison between eulerian and vof models for two-phase flow assessment in vertical pipes*, *Ciencia, Tecnología Futuro* **7** (2017), <https://dx.doi.org/10.29047/01225383.66>.

- [18] F. Harlow and J. Welch, *Numerical calculation of time-dependent viscous incompressible flow of fluid with free surface*, [Physical Fluids](#) **8**, 2182 (1965).
- [19] S. Osher and R. Fedkiw, *Level Set Methods and Dynamic Implicit Surfaces*, Applied Mathematical Sciences, Vol. 153 (Springer New York, New York, NY, 2003).
- [20] R. A. Gingold and J. J. Monaghan, *Smoothed particle hydrodynamics: theory and application to non-spherical stars*, [Monthly Notices of the Royal Astronomical Society](#) **181**, 375 (1977).
- [21] P. W. Cleary and M. Prakash, *Discrete-element modelling and smoothed particle hydrodynamics: Potential in the environmental sciences*, [Phil. Trans. R. Soc. Lond. A](#) **362**, 2003 (2004).
- [22] R. Canelas, R. Ferreira, A. Crespo, and J. Domínguez, *A generalized sph-dem discretization for the modelling of complex multiphase free surface flows*, (2013).
- [23] R. B. Canelas, A. J. Crespo, J. M. Domínguez, R. M. Ferreira, and M. Gómez-Gesteira, *SPH-DCDEM model for arbitrary geometries in free surface solid-fluid flows*, [Computer Physics Communications](#) **202**, 131 (2016).
- [24] S. Zhang, S. Kuwabara, T. Suzuki, Y. Kawano, K. Morita, and K. Fukuda, *Simulation of solid-fluid mixture flow using moving particle methods*, [Journal of Computational Physics](#) **228**, 2552 (2009).
- [25] R. B. Canelas, J. M. Domínguez, A. J. C. Crespo, M. Gómez-Gesteira, and R. M. L. Ferreira, *Resolved Simulation of a Granular-Fluid Flow with a Coupled SPH-DCDEM Model*, [Journal of Hydraulic Engineering](#) **143**, 06017012 (2017).
- [26] S. Dey, *Turbulence in open-channel flows*, [GeoPlanet: Earth and Planetary Sciences](#) **4**, 95 (2014).
- [27] D. Coles, *The law of the wake in the turbulent boundary layer*, [Journal of Fluid Mechanics](#) **1**, 191 (1956).
- [28] S. Dey and R. V. Raikar, *Characteristics of Loose Rough Boundary Streams at Near-Threshold*, [10.1061/ASCE0733-94292007133:3288](#).
- [29] N. L. Coleman, *Velocity Profiles With Suspended Sediment*, [Journal of Hydraulic Research](#) **19**, 211 (2010).
- [30] H. Kudela, *Turbulent flow*.
- [31] M. H. García, *Sediment Transport and Morphodynamics*, [undefined](#), 21 (2013).
- [32] G. Belaud, L. Cassan, and J.-P. Baume, *Calculation of Contraction Coefficient under Sluice Gates and Application to Discharge Measurement*, [Journal of Hydraulic Engineering](#) **135**, 1086 (2009).
- [33] *Riverine Litter Monitoring - Options and Recommendations*, Tech. Rep. (European Commission, 2016).
- [34] P. Vriend, H. Hidayat, J. van Leeuwen, M. R. Cordova, N. P. Purba, A. J. Löhr, I. Faizal, N. S. Ningsih, K. Agustina, S. Husrin, D. D. Suryono, I. Hantoro, B. Widianarko, P. Lestari, B. Vermeulen, and T. van Emmerik, *Plastic Pollution Research in Indonesia: State of Science and Future Research Directions to Reduce Impacts*, [Frontiers in Environmental Science](#) **9**, 187 (2021).
- [35] K. Waldschla and H. Schu, *Effects of Particle Properties on the Settling and Rise Velocities of Microplastics in Freshwater under Laboratory Conditions*, (2019), [10.1021/acs.est.8b06794](#).
- [36] L. Schmoker and W. H. Hager, *(scale modeling of wooden debris accumulation at a debris rack)*. [Journal of Hydraulic Engineering](#) **139**, 827 (2014).
- [37] H. Wendland, *Piecewise polynomial, positive definite and compactly supported radial functions of minimal degree*, [Advances in Computational Mathematics](#) 1995 **4**:1 **4**, 389 (1995).
- [38] M. B. Liu and G. R. Liu, *Smoothed Particle Hydrodynamics (SPH): an Overview and Recent Developments*, [Archives of Computational Methods in Engineering](#) 2010 **17**:1 **17**, 25 (2010).
- [39] G. Fourtakas, R. Vacondio, J. Dominguez Alonso, and B. Rogers, *Improved density diffusion term for long duration wave propagation*, (2020) pp. 351–357, 2020 SPHERIC Harbin International Workshop ; Conference date: 13-01-2020 Through 16-09-2020.

- [40] J. J. Monaghan, *Smoothed Particle Hydrodynamics*, [Annual Review of Astronomy and Astrophysics](#) **30**, 543 (1992).
- [41] P. A. Cundall and O. D. L. Strack, *A discrete numerical model for granular assemblies*, [Geotechnique](#) **29**, 47 (1979).
- [42] R. B. Canelas, J. M. Domínguez, A. J. C. Crespo, M. Gómez-Gesteira, and R. M. L. Ferreira, *Resolved Simulation of a Granular-Fluid Flow with a Coupled SPH-DCDEM Model*, [Journal of Hydraulic Engineering](#) **143**, 06017012 (2017).
- [43] N. V. Brilliantov and T. Poeschel, *Granular Gases with Impact-velocity Dependent Restitution Coefficient*, (2002).
- [44] A. J. Crespo, M. Gómez-Gesteira, and R. A. Dalrymple, *Boundary conditions generated by dynamic particles in SPH methods*, [Computers, Materials and Continua](#) **5**, 173 (2007).
- [45] A. Tafuni, J. Domínguez, R. Vacondio, and A. Crespo, *Accurate and efficient sph open boundary conditions for real 3-d engineering problems*, (2017).
- [46] Sulzer Pumps, *Pipelines, Valves and Flanges*, [Centrifugal Pump Handbook](#), 159 (2010).
- [47] V. C. Pinto, T. Ramos, S. Alves, J. Xavier, P. Tavares, P. M. G. P. Moreira, and R. M. Guedes, *ScienceDirect Comparative failure analysis of PLA, PLA/GNP and PLA/CNT-COOH biodegradable nanocomposites thin films*, [Procedia Engineering](#) **114**, 635 (2015).
- [48] W. Pawlak, *Wear and Coefficient of Friction of PLA-Graphite Composite in 3D Printing Technology*, [Engineering Mechanics](#), 14 (2018).
- [49] R. B. Canelas, J. M. Domínguez, A. J. Crespo, M. Gómez-Gesteira, and R. M. Ferreira, *A Smooth Particle Hydrodynamics discretization for the modelling of free surface flows and rigid body dynamics*, [International Journal for Numerical Methods in Fluids](#) **78**, 581 (2015).
- [50] F. H. Clauser, *Turbulent Boundary Layers in Adverse Pressure Gradients*, [Journal of the Aeronautical Sciences](#) **21**, 91 (2012).
- [51] D. Violeau and R. Issa, *Numerical Modelling of Complex Turbulent Free Surface Flows with the SPH Method: an overview*, [International Journal for Numerical Methods in Fluids](#) **53**, 277 (2007).
- [52] A. D. Mascio, M. Antuono, A. Colagrossi, and S. Marrone, *Smoothed particle hydrodynamics method from a large eddysimulation perspective*, [physics of fluids](#) **29** (2017), <https://doi.org/10.1063/1.497827>.
- [53] D. Violeau, S. Piccon, and J. Chabard, *Two attempts of turbulence modeling in smoothed particle hydrodynamics*, [Proceedings of the 8th Symposium on Flow Modelling and Turbulence Measurements](#), 339 (2002).
- [54] D. Violeau, *One and Two-Equations Turbulent Closures For Smoothed Particle Hydrodynamics*, [Hydroinformatics](#), 87 (2004).
- [55] R. Issa, D. Violeau, and D. Laurence, *A first attempt to adapt 3D large eddy simulation to the Smoothed Particle Hydrodynamics gridless method*, [Proceedings of the Int. Conf. Comput. and Experimental Eng. and Sciences, 1st Symposium on Meshless Methods](#) (2005).
- [56] H. Jasak, *OpenFOAM: open source CFD in research and industry*, [International Journal of Naval Architecture and Ocean Engineering](#) **1**, 89 (2009).
- [57] *ANSYS Fluent Theory Guide*, ANSYS, Inc. (2013).
- [58] D. A. Lysenko, I. S. Ertesvåg, and K. E. Rian, *Modeling of turbulent separated flows using OpenFOAM*, [Computers Fluids](#) **80**, 408 (2013).
- [59] J. M. Dominquez, A. J. Crespo, and M. Gomez-Gesteira, *Optimization strategies for CPU and GPU implementations of a smoothed particle hydrodynamics method*, [Computer Physics Communications](#) **184**, 617 (2013).

- [60] A. Crespoa, J. Domínguez, B. Rogers, M. Gómez-Gesteira, S. Longshaw, R. Canelas, R. Vacondio, A. Barreiroa, and O. García-Feal, *DualSPHysics: Open-source parallel CFD solver based on Smoothed Particle Hydrodynamics (SPH)*, [Computer Physics Communications](#) **187**, 204 (2015).
- [61] M. Cremonesi, A. Franci, S. Idelsohn, and E. Oñate, *A State of the Art Review of the Particle Finite Element Method (PFEM)*, [Archives of Computational Methods in Engineering](#) **27**, 1709 (2020).
- [62] E. Oñate, S. R. Idelsohn, F. Del Pin, and R. Aubry, *The particle finite element method. An overview*, [International Journal of Computational Methods](#) **01**, 267 (2004).
- [63] A. Franci, I. De-Pouplana, G. Casas, M. Celigueta, J. González-Usúa, and E. Oñate, *PFEM-DEM for particle-laden flows with free surface*, [Computational Particle Mechanics](#) **7**, 101 (2020).
- [64] C. B. Fonte, J. A. A. Oliveira, and L. C. D. Almeida, *DEM-CFD COUPLING: MATHEMATICAL MODELLING AND CASE STUDIES USING ROCKY-DEM® AND ANSYS FLUENT®*, Tech. Rep. (2015).
- [65] C. Goniva, C. Kloss, A. Hager, and S. Pirker, *An open source cfd-dem perspective*, 5th OpenFOAM (2010).
- [66] T. Shan and J. Zhao, *A coupled CFD-DEM analysis of granular flow impacting on a water reservoir*, [Acta Mechanica](#) **225**, 2449 (2014).
- [67] T. k. Nian, H. Wu, K. Takara, D. y. Li, and Y. j. Zhang, *Numerical investigation on the evolution of landslide-induced river blocking using coupled DEM-CFD*, [Computers and Geotechnics](#) **134**, 104101 (2021).
- [68] B. Bouscasse, A. Colagrossi, S. Marrone, and M. Antuono, *Nonlinear water wave interaction with floating bodies in SPH*, [Journal of Fluids and Structures](#) **42**, 112 (2013).
- [69] B. Bouscasse, A. Colagrossi, S. Marrone, and M. Antuono, *Nonlinear water wave interaction with floating bodies in SPH*, [Journal of Fluids and Structures](#) **42**, 112 (2013).
- [70] P. Omidvar, P. K. Stansby, and B. D. Rogers, *SPH for 3D floating bodies using variable mass particle distribution*, [International Journal for Numerical Methods in Fluids](#) **72**, 427 (2013).
- [71] D. Violeau, C. Buvat, K. Abed-Meraim, and E. de Nanteuil, *Numerical modelling of boom and oil spill with SPH*, [Coastal Engineering](#) **54**, 895 (2007).
- [72] C. Antoci, M. Gallati, and S. Sibilla, *Numerical simulation of fluid-structure interaction by SPH*, [Computers and Structures](#) **85**, 879 (2007).